

Production of
Charm and Beauty Quarks
at HERA

HABILITATIONSSCHRIFT
zur
Erlangung der Venia legendi
für das Fach Physik
der
Ruprecht-Karls-Universität
Heidelberg

vorgelegt von
Olaf Behnke
aus Hamburg
Oktober 2005

Abstract

The measurements of charm and beauty quark production at the world wide only electron proton collider HERA are reviewed. The results obtained with the H1 and ZEUS detectors are compared to predictions from perturbative Quantum Chromo Dynamics.

Kurzzusammenfassung

Dieses Essay fasst die Ergebnisse über die Produktion schwerer Charm und Beauty Quarks an der weltweit einzigen Elektron-Proton-Kollisionsmaschine HERA zusammen. Die Messungen, die mit den H1 und ZEUS Detektoren erzielt wurden, werden mit Vorhersagen der Störungsrechnung der starken Kraft verglichen.

Contents

1	Introduction	4
2	Theory of heavy flavour production at HERA	12
2.1	HERA kinematic variables and phase space	12
2.2	Perturbative QCD calculations for heavy flavour production	13
2.3	Monte Carlo simulation models	17
2.4	Uncertainties of the pQCD calculations	19
3	Experimental aspects	21
3.1	HERA	21
3.2	H1 and ZEUS Detectors	21
4	Heavy flavour Tagging methods	30
4.1	Charm tagging with full reconstruction of the golden D^{*+} decay channel	31
4.2	Charm tagging with full reconstruction of D-mesons + lifetime tag	34
4.3	Beauty tagging with lepton + p_t^{rel} + lifetime tag + jets	36
4.4	Charm and Beauty with inclusive lifetime tagging	40
4.5	Charm and Beauty with double tagging	43
4.6	Jet reconstruction	47
4.7	Measurement systematic errors	49
5	Results	50
5.1	Charm photoproduction	51
5.1.1	D^{*+} inclusive measurements	51
5.1.2	Studies with a D^{*+} and one other hard parton	56
5.1.3	Parton parton studies in charm tagged events	57
5.2	Charm production in DIS	66
5.3	Beauty introduction	75
5.4	Beauty in photoproduction	75
5.4.1	Analyses using events with a muon and jets	77

5.4.2	Double tag analyses using $D^{*+} \mu$ and $\mu\mu$:	78
5.4.3	Summary of beauty photoproduction as functions of transverse momentum and pseudorapidity of the b quark	79
5.4.4	x_{γ}^{obs} comparisons for beauty, charm and light quark events:	84
5.5	Beauty production in DIS:	85
5.5.1	Analyses using events with a muon and jets	85
5.6	Summary of beauty photoproduction and DIS results as a function of photon virtuality Q^2	87
5.7	Charm and Beauty cross sections at other colliders	89
5.8	Charm and beauty contributions $F_2^{c\bar{c}}$ and $F_2^{b\bar{b}}$ to the proton structure function F_2	93
5.8.1	Experimental aspects and extrapolation	93
5.8.2	$F_2^{c\bar{c}}$ Results	95
5.8.3	$F_2^{b\bar{b}}$ results	103
5.8.4	Direct determination of the proton gluon density with D^{*+} data	106
5.9	Charm fragmentation issues	106
6	HERA II	111
6.1	Detector upgrades for HERA II	111
6.2	Physics goals and reach with HERA II	113
7	Summary	119
9	References	122

1 Introduction

The heavy charm and beauty quarks do not exist as stable particles in nature, since they decay into lighter quarks. They were discovered with modern particle accelerators, which provide enough energy to produce these particles, which thereafter decay within a time of the order of a picosecond. However this time span is long enough for the charm and beauty quarks to interact strongly and to form bound states with other quarks. Since the charm and the beauty quarks were discovered in 1974 [1, 2] and in 1977 [3], respectively, detailed experimental investigations have been performed to understand the interactions of these particles. The large masses of the heavy quarks make them especially interesting for the study of the strong interactions, since the strong force is weaker for harder scales and thus better calculable. However the accurate understanding of how charm and beauty quarks are produced in hadronic environments is still an open issue. Here the HERA electron proton collider offers fascinating research opportunities. Heavy flavour production at HERA is the topic of this essay. In the following the underlying ideas are detailed and the physics key questions will be developed.

HERA is the only electron proton collider in the world. Beam energies of 27.6 GeV for electrons or positrons and 920 GeV for protons provide a centre-of-mass energy of 319 GeV. The main interest in the production of charm and beauty quarks at HERA can be related to the fact that these quarks with their masses of $m_c \approx 1.5$ GeV and $m_b \approx 4.75$ GeV are too heavy to be stable constituents of the proton with its mass of $m_p = 0.935$ GeV – thus special production mechanisms are needed. The dominant process is photon gluon fusion (PGF), shown in the left plot of figure 1. This reaction

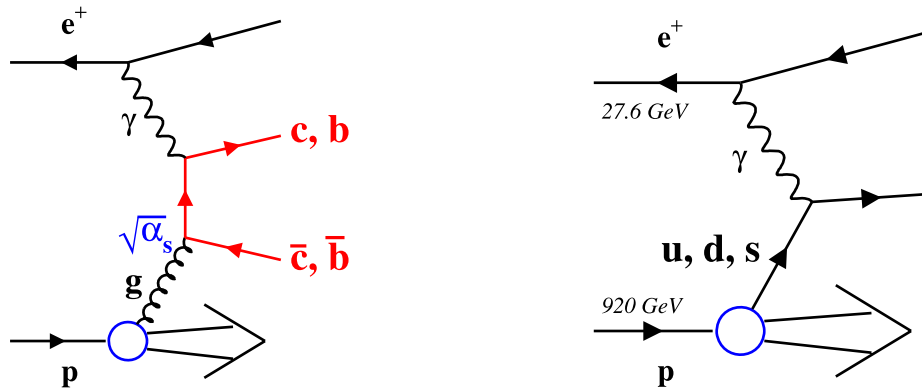


Figure 1: The left plot shows the dominant production process for charm and beauty quarks in ep collisions at HERA, the photon gluon fusion (PGF) reaction. The right plot depicts for comparison the simplest diagram for light quark scattering.

involves the *strong force*, or quantum chromo dynamics (QCD) and is directly sensitive to the gluon density in the proton. On the contrary the light valence or sea quarks in the proton can directly scatter off the electron with only the electromagnetic force (photon exchange) involved, as shown in the right plot of figure 1. The heavy quark masses are

for another reason very important - they set hard scales that facilitate the applicability of perturbative QCD (pQCD), even if there are no other hard scales available. This is illustrated in figure 2, which shows the running coupling constant α_s as a function of the hard scale μ . At the scales of the heavy quark masses, $\alpha_s(m_c)$ and even more

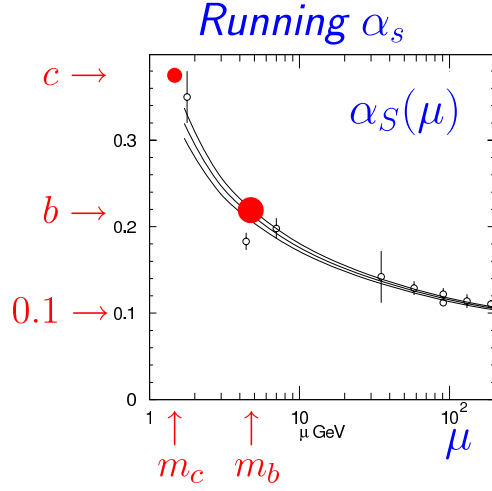


Figure 2: Running coupling constant α_s of the strong force as a function of the hard scale μ .

$\alpha_s(m_b)$ are small enough that higher order processes, i.e. with further gluons involved, are expected to be sufficiently suppressed. Thus the QCD hard scattering factorisation theorem [4] can be applied. This states that the proton gluon density, determined indirectly from the variation of the inclusive structure function F_2 with changing photon virtuality Q^2 (see figure 3), is universal and can be used to predict exclusive hard processes, such as heavy flavour production. The relevant range of the proton mo-

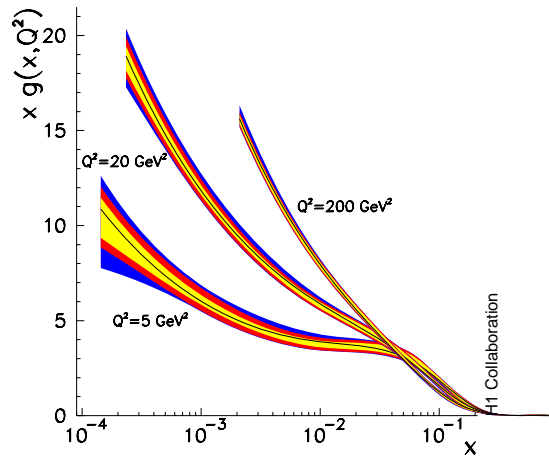


Figure 3: Gluon density in the proton as a function of the proton momentum fraction x carried by the gluon for three different values of the photon virtuality Q^2 , as determined from the scaling violations of the inclusive structure function F_2 , from [5].

mentum fraction x carried by the gluon, which can be probed with the PGF process at

HERA is $\sim 10^{-4} - 10^{-1}$ for charm and $\sim 10^{-3} - 10^{-1}$ for beauty production. Thus the first key question for heavy flavour production at HERA, to be answered in this essay is:

Key question 1: *What do we learn from heavy flavour production at HERA about the proton gluon density? How accurate can we determine it? Is it in agreement with the gluon density determined from the scaling violations of F_2 ? Answers will be provided in section 5.8.*

The strong coupling constant α_s is relatively small at the charm and beauty mass hard scales, on the other hand it is *not that small* – sizable contributions from higher order processes are expected. Some of the next to leading order (NLO) processes are illustrated in figure 4 (right three diagrams). In general calculations for heavy flavour

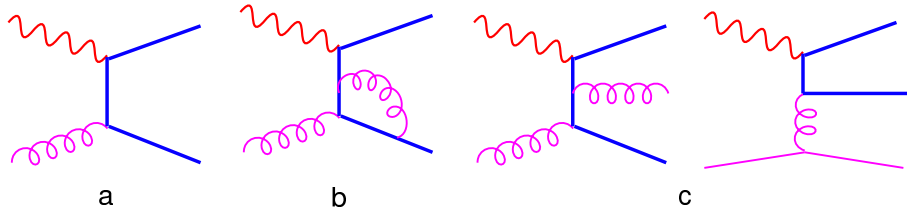


Figure 4: Leading order (left) and selection of next to leading order (right three) processes for heavy flavour production at HERA in the massive scheme.

production at HERA are available to this order, which is $o(\alpha_s^2)$ for cross sections. The NLO contributions lead to a roughly 30 – 50% increase in the expected charm and beauty production cross sections as detailed in [6]. This is partially due to the effect that new types of diagrams contribute for the first time at NLO such as light quark initiated processes (most right diagram in figure 4). This leads to the second key question:

Key question 2: *Are the available calculations for heavy flavour production at HERA in next to leading order perturbative QCD sufficiently precise or are higher order corrections needed? This will be answered in sections 5.1, 5.2, 5.4 and 5.5.*

Besides the heavy quark masses, there can be two other relevant hard scales available in the heavy quark production process, the virtuality Q^2 of the exchanged photon and the transverse momenta p_T of the outgoing heavy quarks, as depicted in figure 5. This leads to the so-called multi-hard-scale problem in QCD, which is related to terms in the perturbation series of the form

$$\sim [\alpha_s \ln(p_t^2/m_h^2)]^n \quad \text{or} \quad \sim [\alpha_s \ln(Q^2/m_h^2)]^n, \quad (1)$$

with $h = c, b$. Such terms appear to all orders n and represent collinear gluon radiations from the heavy quark lines. These terms can be large for $Q^2 \gg m_h$ or $p_T^2 \gg m_h$ and hence can spoil the convergence of the perturbation series. The following competing approximations are available to deal with this problem:

1. In the so called **massive** scheme [7] which was so far assumed, the heavy quarks are treated fully massive. The heavy quarks are only perturbatively produced as

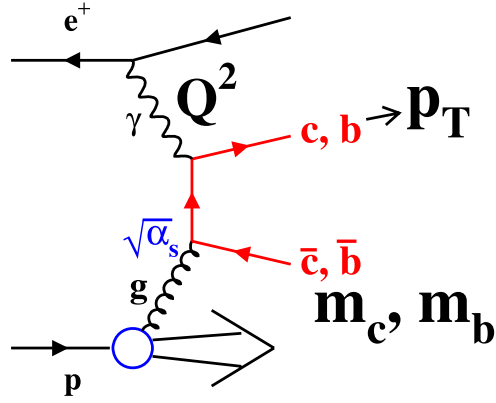


Figure 5: Possible hard scales in the photon gluon fusion process.

in the diagrams in figure 4. The higher order terms in equation 1 beyond NLO are simply ignored. This scheme is expected to work well for the kinematic region $Q^2, p_T^2 \sim m_h^2$.

2. In the so called **massless** scheme [10] the mass of the heavy quarks is neglected in the kinematics of the hard process. In this scheme the heavy quarks can also be absorbed in the proton structure i.e. be treated as massless sea quarks like the light u, d and s quarks; the leading order process is shown in the left plot of figure 6. This treatment allows to resum the terms in equation 1 to all orders, i.e.

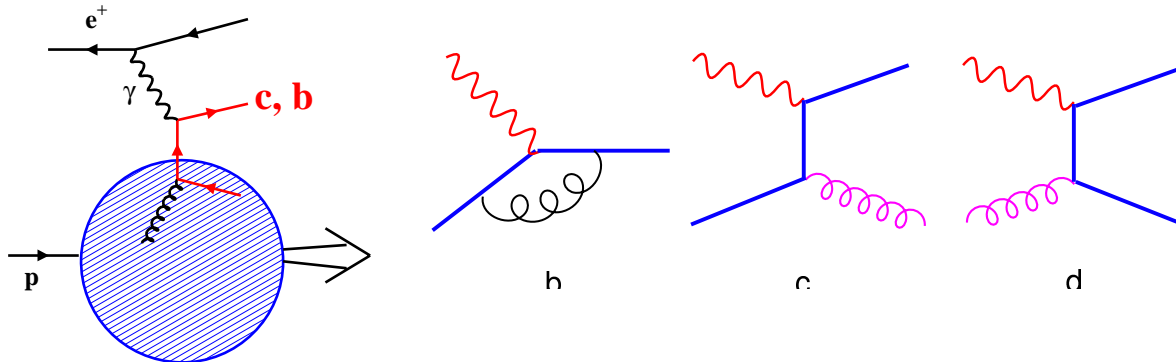


Figure 6: Leading order (left) and selection of next to leading order (right three) processes for heavy flavour production in the massless scheme.

the collinear radiations are absorbed in the 'heavy quark' proton density function, using the DGLAP equations [11], as it is usually also done for the light quarks. This scheme is expected to work well for $Q^2, p_T^2 \gg m_h^2$. A selection of next to leading order diagrams is shown in the right three diagrams in figure 6. Note that here the leading order diagram of the massive scheme (figure 4 left) is recovered.

3. There are **mixed** schemes [12–16], which use for small $Q^2, p_T^2 \leq m_h^2$ the massive scheme, at high $Q^2, p_T^2 \gg m_h^2$ the massless scheme and at intermediate scales a suitable interpolation of the two.

A unique feature of HERA is the wide kinematical range in which the multi-hard-scale problem is probed. For the photon virtuality the range $0 < Q^2 < 1000 \text{ GeV}^2$ is covered and for the heavy quark transverse momenta $0 < p_T < 50 \text{ GeV}$, both for charm and for beauty. The next key question is:

Key question 3: *What do we learn from heavy flavour production at HERA about the inherent multi-hard-scale problem in perturbative QCD? Which of the available approximate pQCD schemes provides a better description of the data, the massive, the massless or the mixed schemes? Answers can be found in the sections 5.1, 5.2, 5.4, 5.5 and 5.8.*

Besides direct photon interactions, as shown in the figures 1, 4 and 6, there exist also resolved photon processes, where the photon fluctuates hadronically before the hard interaction, as illustrated in figure 7. At HERA resolved photon processes play

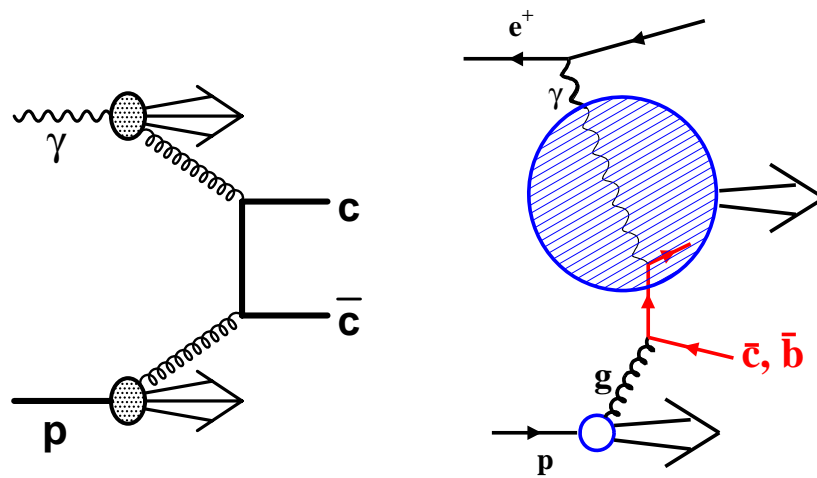


Figure 7: Leading order resolved photon diagrams for charm and beauty production in the massive scheme (left) and in the massless scheme (right).

an important role in photoproduction, where $Q^2 \sim 0 \text{ GeV}^2$, and are suppressed in the deep inelastic scattering (DIS) regime $Q^2 > 1 \text{ GeV}^2$. The heavy quark masses themselves provide hard scales and kinematic thresholds that suppress the probability for a fluctuation of the photon into a heavy quark pair compared to a fluctuation into a light quark pair. The predictions depend crucially on the applied scheme: In the massive scheme the heavy quarks are treated fully massive and can only be perturbatively produced. The leading order diagram is shown in the left plot of figure 7. In the massless scheme the quarks can appear as massless constituents of the resolved photon. The leading order diagram is shown in the right plot of figure 7. The massless scheme predictions exceed the massive scheme calculations usually by far. Thus key question 4 is:

Key question 4: *How much do heavy quarks contribute to the resolved photon structure or, vice versa, how much do resolved photon processes contribute to heavy flavour production at HERA? Answers will be given in section 5.1.*

Charm (beauty) events contribute up to $\sim 30\%$ ($\sim 3\%$) of the flavour inclusive ep

cross sections at HERA. Thus a precise knowledge of these contributions is mandatory for the interpretation of the flavour inclusive proton structure function F_2 . Thus key question 5 is:

Key question 5: *What is the impact of the measurements of the charm and beauty contributions to the inclusive ep scattering on the interpretation of the flavour inclusive structure function F_2 in terms of the proton constituents, i.e. light valence quarks, light and heavy sea quarks and the gluon density? Some answers are given in section 5.8, mainly for the gluon density.*

At HERA one can probe the kinematic regime of very small small proton momentum fractions carried by the quark which is struck by the photon. This is conveniently expressed by the variable *Bjorken* x , which reaches at HERA values down to 10^{-4} at still moderate photon virtualities $Q^2 \sim \text{few GeV}^2$. For such small x there is a large phase space available for multi gluon emissions in the proton before the hard interaction, as illustrated in figure 8.

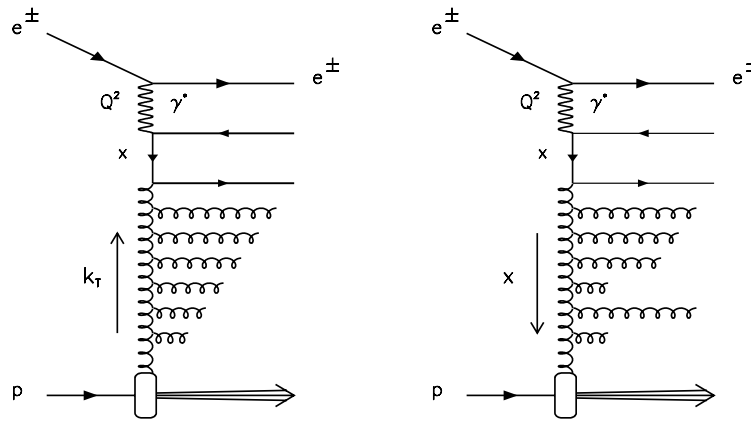


Figure 8: Multi gluon emission for small Bjorken x in the DGLAP (left) and in the BFKL (right) approximation. The heavy charm or beauty quarks are produced in the quark box below the photon line. The lengths of the radiated gluon lines indicates the sizes of the gluon transverse momenta.

There are several perturbative QCD schemes available, which resum a certain part of the emissions to all order and neglect other emissions.

- In the DGLAP [11] parton evolution scheme, the gluon emissions are strongly ordered in their transverse momenta, from very small momenta for the initial emissions in the proton to larger momenta for emissions closer to the hard interaction with the photon.
- In the BFKL [17] scheme, the gluon emissions are strongly ordered in energy, from large energies for initial emissions in the proton to smaller energies closer to the hard interaction, while no strong ordering in the transverse momenta is predicted.

- The CCFM [18] scheme is a mixture of DGLAP and BFKL. Here the emissions are ordered in the angle with respect to the proton direction, from small angles for the initial emissions to larger angles closer to the hard interaction.

Since long one has searched for deviations from DGLAP, e.g. with using jets to measure BFKL like gluon emissions. However with a jet alone one doesn't know if it originates from a quark or a gluon. Here the heavy quarks play a special role, since the experimental tagging from the decay products unambiguously tags a quark and hence reduces the number of possible Feynman diagrams. Thus key question 6 is:

Key question 6: *What do we learn specifically on higher order QCD processes such as multi gluon emissions in the proton from the fact that the heavy flavour tag unambiguously identifies a quark? This topic is addressed in section 5.1 and in the summary.*

In general the HERA ep collider provides a bridge from e^+e^- collisions e.g. at LEP to pp collisions at TEVATRON or LHC. The fragmentation of the heavy quarks which has been measured with good precision in e^+e^- collisions can be tested at HERA for universality in a different colour environment, which resembles the one in pp or other hadron hadron collisions. More specifically in the leading order PGF process (figure 4 left) the heavy quark pair is *not* in a colour singlet state, while it is in the reaction $e^+e^- \rightarrow Z \rightarrow c\bar{c}$ or $b\bar{b}$. Relevant measurements can be made at HERA for the charm fragmentation function and the production ratios of different charmed hadron species including orbital excited (L=1) states. Thus key question 7 is:

Key question 7: *What can we learn at HERA on the universality of charm fragmentation? This is the topic of section 5.9.*

Further heavy flavour topics, which are studied at HERA are:

- Charmonium and Upsilon production: The photon gluon fusion process $\gamma \rightarrow c\bar{c}$ or $b\bar{b}$ can also lead to the production of bound states such as the J/Ψ resonance. The formation of a bound state complicates the theoretical description and leads to further or different model uncertainties. Comprehensive reports can be found in [19,20] and this topic is not further discussed here.
- Diffractive charm and beauty production: A few percent of the HERA ep scattering reactions can be attributed to hard diffractive processes with a colourless exchange between the proton which stays intact or dissociates and a photon dissociative system, which is in the simplest case a quark antiquark pair ($q\bar{q}$). In pQCD this process is mediated in lowest order by two gluon exchange between the proton and the $q\bar{q}$ system. The $q\bar{q}$ pair can be also a charm or a beauty quark pair. This case is especially interesting, similarly to inclusive ep scattering, due to the hard scale provided by the heavy quark mass, which ensures the applicability of pQCD and secondly due to the direct sensitivity on the gluon(s) which enter the hard interaction. In general diffractive hard scattering at HERA is a unique and

exciting field for the understanding of QCD. However, it is with respect to the other topics investigated in this essay a rather separate issue and will not be further discussed here. The diffractive charm results obtained so far with D^{*+} mesons do also suffer from the small data statistics, so that the measurements are not very precise. Beauty results are so far not available.

Finally, there are also important aspects of heavy flavour physics which are not investigated at HERA:

- The physics of the decays of the heavy flavoured hadrons: This covers the hadron lifetimes and the branching ratios for certain decay channels and the search for new decay channels.
- Measurements of CP-violation related to the beauty quark sector.

The simple reason for this non-studying at HERA is the too small available statistics for charm and beauty hadrons that can be reconstructed in the detectors. This physics is investigated successfully at other colliders in the world e.g. with e^+e^- machines. For instance the BABAR and BELLE detectors at the B-factories at SLAC and KEK, respectively, have recorded in the recent years a few hundred million beauty and charm events which allowed to study these topics in great detail.

This essay is organised as follows: In section 2 an introduction is given to the description of heavy flavour production in perturbative QCD. The relevant features of the H1 and ZEUS detectors are described in section 3. The following section 4 elucidates the heavy flavour tagging methods exploited for the physics analyses. The results obtained with the HERA I data period collected in the years 1992-2000 are reported in section 5. An outlook to the currently ongoing HERA II data taking, which ends in summer 2007 and concludes HERA, is given in section 6 with emphasis on the physics goals and reach. Section 7 summarises the results presented in this article.

2 Theory of heavy flavour production at HERA

2.1 HERA kinematic variables and phase space

The measurements of heavy quark production at HERA have so far been restricted, for statistical reasons, to the kinematic region of four-momentum transfer squared $Q^2 < 1000 \text{ GeV}^2$, where photon exchange dominates and Z^0 or W^\pm exchange can be neglected. Figure 9 illustrates the event kinematic variables for ep scattering with heavy quark production via the photon gluon fusion process.

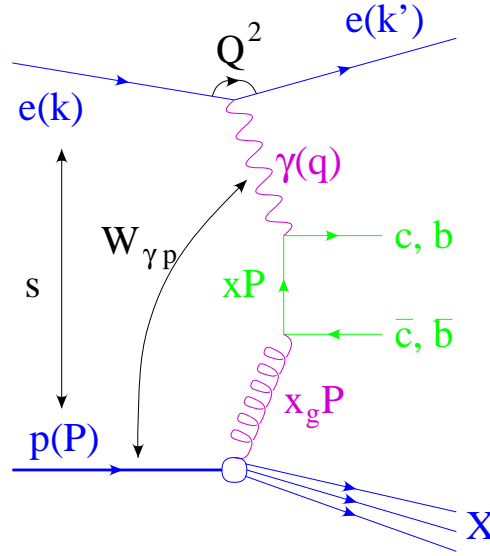


Figure 9: Illustration of event kinematic variables for ep scattering at HERA with heavy quark production via the photon gluon fusion process.

The four-momenta of the incoming electron k , the outgoing electron k' and the proton P can be used to define the following Lorentz invariant variables:

$$s = (k + P)^2 \quad (2)$$

$$Q^2 = -q^2 = -(k - k')^2 \quad (3)$$

$$x = \frac{Q^2}{2P \cdot q} \quad (4)$$

$$y = \frac{P \cdot q}{P \cdot k} \quad (5)$$

$$W_{\gamma p}^2 = (P + q)^2 \quad (6)$$

Here \sqrt{s} is the centre-of-mass energy of the ep system and Q^2 is the photon virtuality. $W_{\gamma p}$ is the centre-of-mass energy of the γp system. In the Quark Parton Model (QPM) Bjorken x describes the proton momentum fraction carried by the scattered parton. y gives the fraction of the electron energy taken by the photon in the proton rest frame.

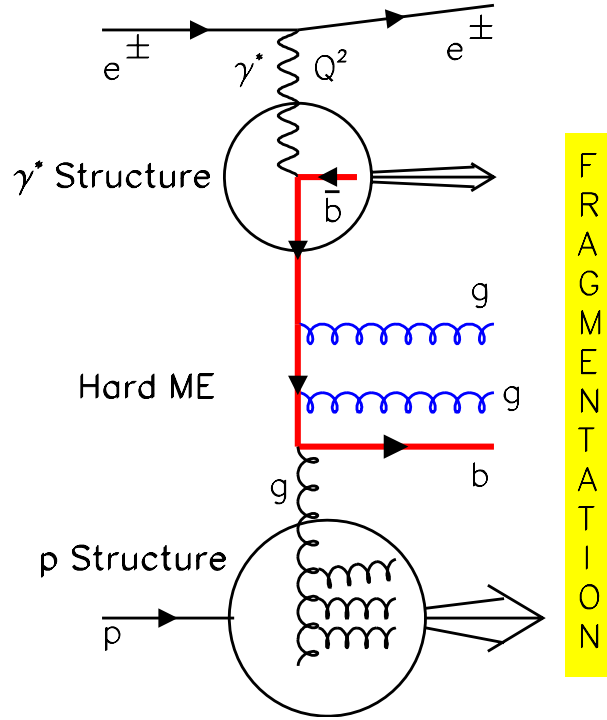


Figure 10: Factorisation of heavy flavour production in QCD in proton structure, photon structure, hard matrix element and fragmentation.

Only three of these five kinematic variables are independent. Neglecting the masses of the electron and the proton the following relations between these quantities hold:

$$Q^2 = s \cdot x \cdot y \quad (7)$$

$$W_{\gamma p}^2 = y \cdot s - Q^2 \quad (8)$$

The ep scattering events are classified by the photon virtuality Q^2 . The regime of small $Q^2 \approx 0 \text{ GeV}^2$ is called *Photoproduction* (γp) and the regime $Q^2 \geq 1 \text{ GeV}^2$ *Deep Inelastic Scattering* (DIS).

2.2 Perturbative QCD calculations for heavy flavour production

QCD calculations of heavy flavour hadron production cross sections factorize the process in four pieces as illustrated in figure 10 and expressed by the following convolution:

$$\sigma = \text{p-Structure} \otimes \gamma^*\text{-structure} \otimes \text{hard-ME} \otimes \text{Fragmentation} \quad (9)$$

Here 'p Structure' denotes the parton densities in the proton, ' γ^* structure' the parton densities in the resolved photon, 'hard ME' the calculable hard scattering cross section and 'Fragmentation' the fragmentation of the quarks into observable hadrons. For the

direct photon gluon fusion process shown in figure 9 the heavy quark cross section (before fragmentation) can be written in the form

$$\sigma_{dir}^{\gamma p}(P_\gamma, P_p) = \int dx f_g^p(x, \mu_F) \hat{\sigma}_{\gamma j}(P_\gamma, xP_p, \alpha_s(\mu_R), \mu_R, \mu_F). \quad (10)$$

Here $f_g^p(x, \mu_F)$ denotes the proton gluon density as a function of the proton momentum fraction x and the factorisation scale μ_F . Gluon radiations with kinematic scales below μ_F are absorbed in the proton gluon density, while those with harder scales are attributed to the hard scattering. The dependence of the gluon density as function of the factorisation scale can be calculated using the DGLAP [11], equations. $\hat{\sigma}_{\gamma j}(P_\gamma, xP_p, \alpha_s(\mu_R), \mu_R, \mu_F)$ is the hard partonic cross section of a photon and a gluon, that depends on their momenta, on the strong coupling constant α_s , on the renormalisation scale μ_r at which α_s is evaluated and on μ_F . The process in figure 9 is a leading order $O(\alpha_s)$ direct photon process, the process in figure 10 a higher order $O(\alpha_s^2)$ resolved photon process. Beyond leading order the separation into direct and resolved photon processes is ambiguous. In the following the available different perturbative QCD schemes that have been already sketched in the introduction are detailed.

Massive scheme: The massive or fixed flavour number scheme (FFNS) [7] follows a rigorous quantum field theory Ansatz. Charm and beauty quarks are treated fully massive and the leading and some of the next to leading order diagrams are shown in figure 4. Calculation programs are available up to next to leading order $O(\alpha_s^2)$, FMNR [21] for photoproduction and HVQDIS [22] for DIS. These calculations are expected to describe heavy flavour production at HERA over most of the accessible kinematic phase space and to encounter only problems for the highest reachable quark transverse momenta and photon virtualities. The two publicly available programs generate events in a similar manner as a Monte Carlo simulation. For each generated event full user access to the outgoing two or three hard partons is provided. This allows to calculate production cross sections on the heavy quark parton level. For hadron level cross sections the situation is highly non trivial, since there exists no rigorous treatment in QCD for the fragmentation of heavy quarks. More specifically a QCD factorisation of the final state fragmentation part from the the hard scattering e.g. like that applied for the initial state proton gluon density and the hard scattering in the PGF process (equation 10) would work only for massless particles. Instead usually a phenomenological factorisation approach is followed which is illustrated in figure 11 for the case of beauty production in DIS with a muon and an associated jet in the final state. The b quark, as generated by the HVQDIS program, is ‘hadronized’ into a b -flavoured hadron by rescaling the three-momentum of the quark using the Peterson fragmentation function [23] with parameters choices, e.g. as those determined in [24]. The program is extended further to include the decay of the b -flavoured hadron into a final state with a muon. The muon momentum spectrum is taken from JETSET [25] and includes direct and indirect decays of b -flavoured hadrons into muons. If in the final state selection also jets are involved the situation is more complicate. Parton level jets are reconstructed by applying the k_t jet algorithm to the outgoing partons. Corrections to the hadron level are

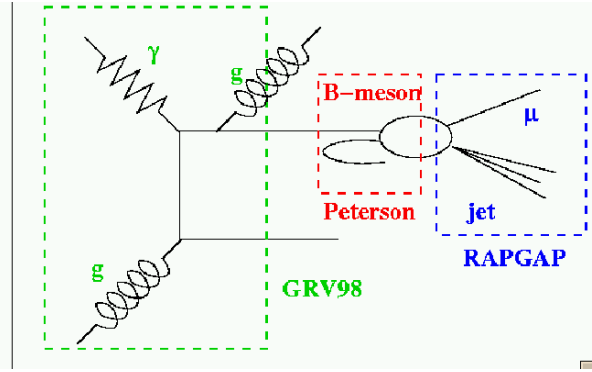


Figure 11: Steps for the massive scheme HVQDIS calculation of beauty production cross sections in DIS with a muon and an associated jet in the final state. The dashed boxes illustrate the reaction at the parton level (left), the b -quark fragmentation process (middle) and the semileptonic decay of the b -flavoured hadron into a muon and further particles (right).

calculated with the help of the Monte Carlo event generators discussed below. These generators embody both the parton and the hadron level.

Massless scheme: In the massless scheme [10] the kinematics of the heavy quarks is treated massless and the leading and some of the next to leading order diagrams are shown in figure 6. Mass effects are considered in the dynamic evolution of the heavy flavour parton densities in the proton and in the resolved photon. Only for scales μ_F larger than the heavy quark masses, the heavy quarks are treated as active partons in the proton and analogously for the resolved photon. Hence these calculations are also labeled sometimes as 'Zero Mass Variable Flavour Number Schemes' (ZMVFNS). The massless treatment allows a rigorous QCD factorisation of the quark fragmentation. A similar factorisation like the one applied for the initial state parton densities and the hard interaction can now be applied for the hard interaction and the fragmentation into the final state hadrons. The fragmentation is described by fragmentation functions, which are scale dependent and evolve according to DGLAP [11]. These fragmentation functions are assumed to be universal and process independent according to the factorisation theorem. The parameters of the fragmentation functions are usually determined from fits to the momentum spectra of hadrons produced in e^+e^- collisions at LEP. Massless calculations are available for HERA in next to leading order $O(\alpha_s^2)$ for the hard scattering cross sections. This includes also higher order processes of the types shown in figure 4 for the massive scheme calculations. The massless calculations are expected to be reliable for transverse momenta or photon virtualities that exceed the heavy quark masses by far. Only a small part of the heavy flavour cross sections at HERA is situated in this phase space. The available calculations, e.g. [26], provide cross sections for photoproduction or DIS with a single charm or beauty hadron in the final state and with or without an additional jet that represents another hard parton. There exist no publicly available programs which would allow to calculate single or

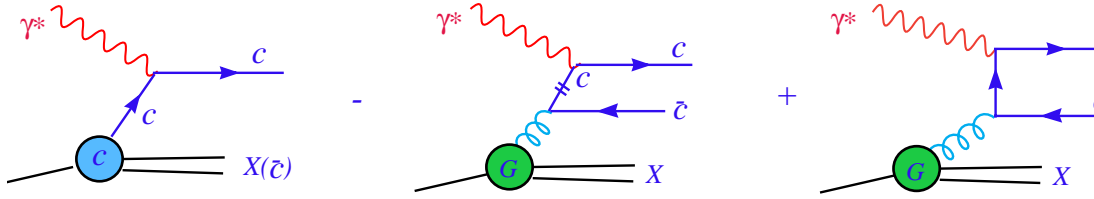


Figure 12: Leading order diagrams for charm production in DIS in the variable flavour number scheme: On the left the QPM diagram is shown, on the right the PGF diagram and in the middle the 'subtraction diagram'.

double parton differential cross sections like for the massive scheme programs FMNR and HVQDIS.

Mixed schemes: The calculations [12–16] in the mixed or variable flavour numbers schemes (VFNS) converge at small (large) photon virtualities Q^2 to the massive (massless) scheme. For intermediate Q^2 an interpolation is performed. The general formula which embodies this idea is the structure

$$[\text{QPM term}] - [\text{asymptotic subtraction term}] + [\text{PGF term}] \quad (11)$$

An illustration is shown in figure 12 for the case of charm production. The subtraction term is the key to the understanding of the interpolation procedure. In this term the charm quark is close to mass-shell and collinear to the gluon and the hadron momenta. For $Q^2 \ll m_c^2$ the subtraction term becomes equally to the QPM term and the remaining contribution is from the PGF diagram. On the contrary for $Q^2 \gg m_c^2$ the subtraction term cancels the PGF term and the QPM term is recovered. There are various approaches [12–16] on how to deal in detail with the subtraction in the intermediate Q^2 region, which are not further discussed here. Recent calculations from the proton parton density fitter groups CTEQ [27] and MRST [28] are available for deep inelastic scattering up to next to leading order $O(\alpha_s^2)$. There is now for the first time ever a calculation on-hand in next to next to leading order (NNLO) from the MRST [29] group. All these calculations provide total c and b production cross sections for given bins in x and Q^2 . There are no programs existing yet for calculating single or double parton differential cross sections, e.g. as a function of the transverse momentum of the leading quark.

FFNLO [30] is a mixed scheme calculation for hadron level cross sections, i.e. it contains a fragmentation part that follows the principles outlined above for the massless scheme calculations. For HERA calculations are available for charm photoproduction with D^{*+} mesons in the final state.

2.3 Monte Carlo simulation models

Monte Carlo simulations are first of all needed for the measurements, to describe signal and background distributions in the data and to determine detector acceptances, efficiencies and smearings. However, for this purpose a reasonable modelling of the underlying physics is needed at the generator level, i.e. before the detector simulation. In the available programs the parton level is generated using leading order pQCD matrix elements. Higher orders are approximated using parton showers radiated from the initial and final state partons. These parton showers are generated in most programs according to the DGLAP [11] parton evolution scheme. The initial state showers represent the multi gluon emissions shown in figure 8. One should note that these showers do - in the QCD factorisation picture - not belong to the hard interaction but are associated with the proton structure, as indicated in figure 10 in the 'proton blob'. For the next to leading order calculations discussed above, the effect of these showers is taken only *implicitly* into account in the proton parton density of the gluon that finally enters the hard interaction in figure 10. However these gluon emissions are in principle observable, e.g. they lead to measurable jets in the detectors close to the proton beam direction. In this respect the Monte Carlo simulations are superior to the next to leading order calculations since they *explicitly* generate this partonic component.

In the following the simulation programs are briefly introduced that are commonly used for heavy flavour production at HERA. However, in this essay the comparisons of data to calculations will be restricted mainly to the next to leading order calculations discussed in the previous subsection, since leading order calculations are regarded as being insufficiently predictive.

PYTHIA: PYTHIA [25] is the most frequently used program for the simulation of photoproduction processes at HERA for all quark flavours. For charm and beauty PYTHIA can be run in the massive or in the massless mode. In both cases the leading order direct photon and resolved photon processes as shown in figure 13a and b are implemented. In the massless case also flavour excitation processes are included, where the charm and beauty quarks are massless constituents of the resolved photon (sketched in figures 13c and d) or of the proton. The parton showers are generated in PYTHIA according to the DGLAP approximation. For the fragmentation PYTHIA embodies the Lund string model [31] which provides a sophisticated treatment. In the fragmentation process the hadrons can also obtain a transverse momentum component with respect to the direction of the mother quark, due to colour strings span between the quark and the other partons. For the heavy quark longitudinal fragmentation component different functions can be chosen, the Lund-Bowler function [32], the Peterson function [23] or others. The fragmentation part of PYTHIA is used for all other generator programs discussed in the following besides HERWIG [33]. PYTHIA is not applicable for DIS, since a proper implementation of the leading order hard matrix element is missing.

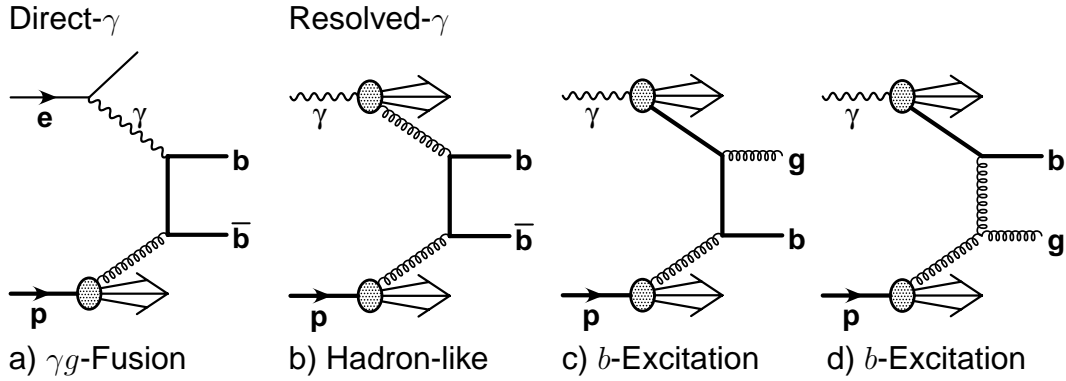


Figure 13: Beauty production processes in leading order pQCD as implemented in PYTHIA

HERWIG: HERWIG [33] is similar to PYTHIA but has implemented a modified DGLAP parton showering approach and a different fragmentation, the cluster hadronisation model. In this model the parton showering process ends with the creation of a set of quarks and antiquarks that are combined to color-singlet clusters and then fragmented into hadrons. HERWIG is typically used for photoproduction analyses as an alternative model to PYTHIA.

CASCADE: CASCADE [34] is the only generator presented here, which does not use DGLAP as default for the evolution of the parton density functions and the parton showering but instead contains an implementation of the CCFM [18] evolution equation. In CASCADE the direct process $\gamma g \rightarrow c\bar{c}$ or $b\bar{b}$ is implemented in the massive scheme using off-shell matrix elements convoluted with k_t -unintegrated parton distributions in the proton. CASCADE is one of the few generators that are used both for photoproduction and DIS. It is used as an alternative simulation model to PYTHIA (RAPGAP) for photoproduction (DIS) measurements.

RAPGAP: RAPGAP [35] is a standard event generator for DIS. Heavy flavour production is modelled in the massive scheme. RAPGAP is interfaced with the program HERACLES [36] which simulates QED initial and final state radiation.

DJANGO: DJANGO [37] is used to model heavy flavour production in DIS in the massless scheme and is based on the programs LEPTO [38] and HERACLES [36].

MC@NLO: The program MC@NLO [39] provides the first next to leading order Monte Carlo simulation of heavy quark production in pp collisions. The NLO hard scattering calculation is matched to parton showers as provided by HERWIG [33], which is also used for the fragmentation. It would be nice to have an extension of this program for heavy flavour production in ep collisions at HERA.

2.4 Uncertainties of the pQCD calculations

There are several sources of uncertainties associated with the perturbative QCD calculations discussed above. A conceptual problem is the uncertainty of the missing higher order perturbative terms, since there is no rigorous treatment at hand. Instead this is usually estimated for the NLO calculations by varying the renormalisation and factorisation scales from their default values, which are typically set in photoproduction to $\mu_r = \mu_f = m_t = \sqrt{m_h^2 + p_T^2}$ and in DIS to $\mu_r = \mu_f = \sqrt{4m_h^2 + Q^2}$, by factors of two up and down. Here h denotes c or b . In the following the effect of this and other relevant error sources are detailed for the case of the massive NLO calculations. For charm the numbers are taken from the papers on inclusive D^{*+} measurements for beauty from the analyses using events with muons and jets. The measurements themselves are presented in sections 4 and 5.

1. Charm in photoproduction ($Q^2 \approx 0 \text{ GeV}^2$):

- For low transverse momenta $p_T(D^{*+}) < 3 \text{ GeV}$ the by far largest theory uncertainty of $\geq 50\%$ results from the variations of the renormalisation scale, reflecting that the not so large charm mass is the only available hard scale.
- Varying the charm mass from the default value 1.5 GeV by $\pm 0.3 \text{ GeV}$ leads to average cross section variations of about $\mp 20\%$. The effect is decreasing slowly towards larger p_T .
- The uncertainty from the proton gluon density is estimated by taking different densities from the various pdf fitter groups. The variations are in the order of $\sim 10\%$ and increase towards smaller p_T .
- A variation of the Peterson fragmentation parameter ϵ_c from e.g. 0.06 to 0.02 leads to a cross section increase of $\sim 40\%$ for high transverse momenta $p_T(D^{*+}) > 7 \text{ GeV}$ and $\sim 20\%$ for smaller momenta $p_T(D^{*+}) < 3 \text{ GeV}$.

2. Charm in DIS ($Q^2 \geq 1 \text{ GeV}^2$):

- The effect of the renormalisation scale variation on the cross sections is drastically reduced to $\leq 10\%$, which is due to the presence of the additional hard scale provided by Q^2 .
- The other uncertainties are similar as for photoproduction.

3. Beauty in photoproduction ($Q^2 \approx 0 \text{ GeV}^2$):

- The variation of the renormalisation scale leads to typical cross section changes of $\leq 10\%$, much smaller compared to the charm case, due to the larger hard scale provided by the beauty mass.
- Varying the beauty mass from the default value 4.75 GeV by $\pm 0.3 \text{ GeV}$ leads to average cross section variations of about $\mp 20\%$.

- The uncertainty from the proton gluon density is small. This is due to the fact that for beauty production the relevant proton momentum fraction x_g carried by the gluon is $x_g \geq 0.01$ and the gluon density is well known in this region for relevant factorisation scales $\mu_F^2 = p_T^2 + m_b^2 \geq 25 \text{ GeV}^2$, as can be seen in figure 3. The resulting beauty production cross section errors are in the order of a few percent.
 - The uncertainty when varying the Peterson fragmentation parameter ϵ_b e.g. from 0.0033 to 0.0025 is $\sim 3\%$.
4. Beauty in DIS ($Q^2 \geq 1 \text{ GeV}^2$): The errors are rather similar as for photoproduction.

For the massless calculations the errors are approximately similar for the above discussed sources. An additional uncertainty is observed for the choice of the resolved photon structure function, giving variations of the order of 20% for charm photoproduction cross section results. The variations increase towards smaller angles of the produced heavy quarks with respect to the proton beam axis.

3 Experimental aspects

3.1 HERA

HERA is the only electron proton collider in the world. It is situated at the DESY laboratory in Hamburg. The HERA ring (see figure 14) is about 25 m below ground and has a circumference of 6.4 km. Electrons or positrons¹ and protons are accelerated in two separate rings to final energies of 27.6 GeV and 920 GeV (820 GeV before 1998), respectively, providing a centre-of-mass energy of $\sqrt{s} = 319$ GeV (300 GeV before 1998). Both beams are stored in 180 bunches. The bunch-crossing rate is 10 MHz. Electrons and protons collide in two interaction regions, where the H1 and ZEUS detectors are located. The data taking with the two detectors started in 1992 and continues until today.

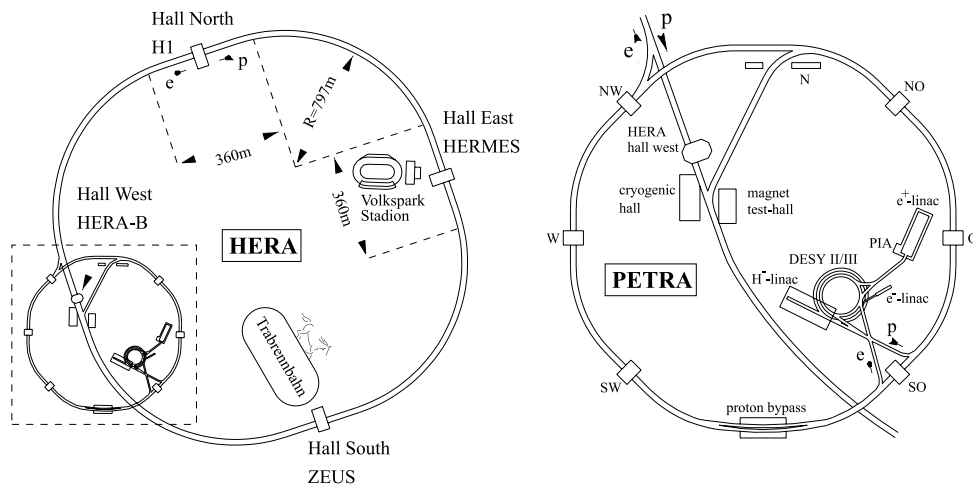


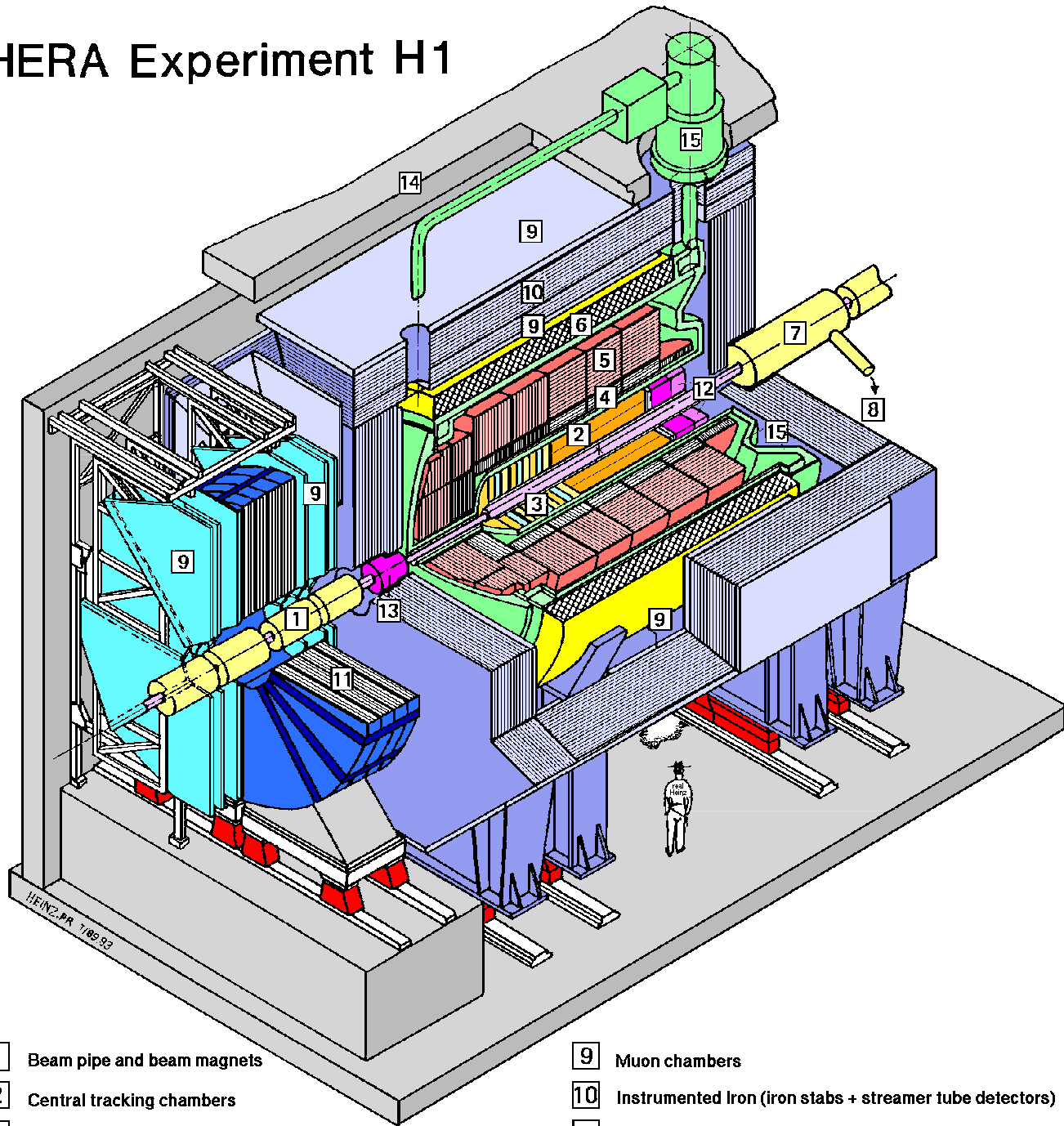
Figure 14: The HERA ep collider with the H1 and ZEUS experiments on the left and the HERA pre-accelerators on the right.

3.2 H1 and ZEUS Detectors

H1 and ZEUS are typical modern multi-purpose collider detectors and are described in detail in [40, 41]. In the following the aspects are discussed which are most relevant for the heavy flavour measurements presented in this essay. A sketch of the 2800 ton heavy H1 detector is shown in figure 15. The electrons enter along the central axis from the left and the protons from the right and interact in the center of the detector (marked in figure 15 with the cross right beneath the [2]).

¹Hereafter, both electrons and positrons are referred to as electrons, unless explicitly stated otherwise.

HERA Experiment H1



- | | |
|--|--|
| 1 Beam pipe and beam magnets | 9 Muon chambers |
| 2 Central tracking chambers | 10 Instrumented Iron (iron slabs + streamer tube detectors) |
| 3 Forward tracking and Transition radiators | 11 Muon toroid magnet |
| 4 Electromagnetic Calorimeter (lead) | 12 Warm electromagnetic calorimeter |
| 5 Hadronic Calorimeter (stainless steel) | 13 Plug calorimeter (Cu, Si) |
| 6 Superconducting coil (1.2T) | 14 Concrete shielding |
| 7 Compensating magnet | 15 Liquid Argon cryostat |
| 8 Helium cryogenics | |

Figure 15: Layout of the H1 detector, for a detailed discussion see [40].

The right-handed coordinate system used at H1 and ZEUS has its origin at this nominal interaction point. The z -axis points in the proton beam direction. The region with positive z is called the “forward” region. The polar angle θ is the angle with respect to the z -axis. Instead of θ the pseudo-rapidity $\eta = -\ln \tan(\theta/2)$ is often used. The x -axis points towards the centre of the HERA ring and the y -axis points perpendicular upwards. The x - y - or r - ϕ -plane is also denoted as the transverse plane.

In figure 16 a rz -section of the H1 tracking chambers and calorimeters is displayed, where a few important detector polar acceptance borders are indicated as lines. Some

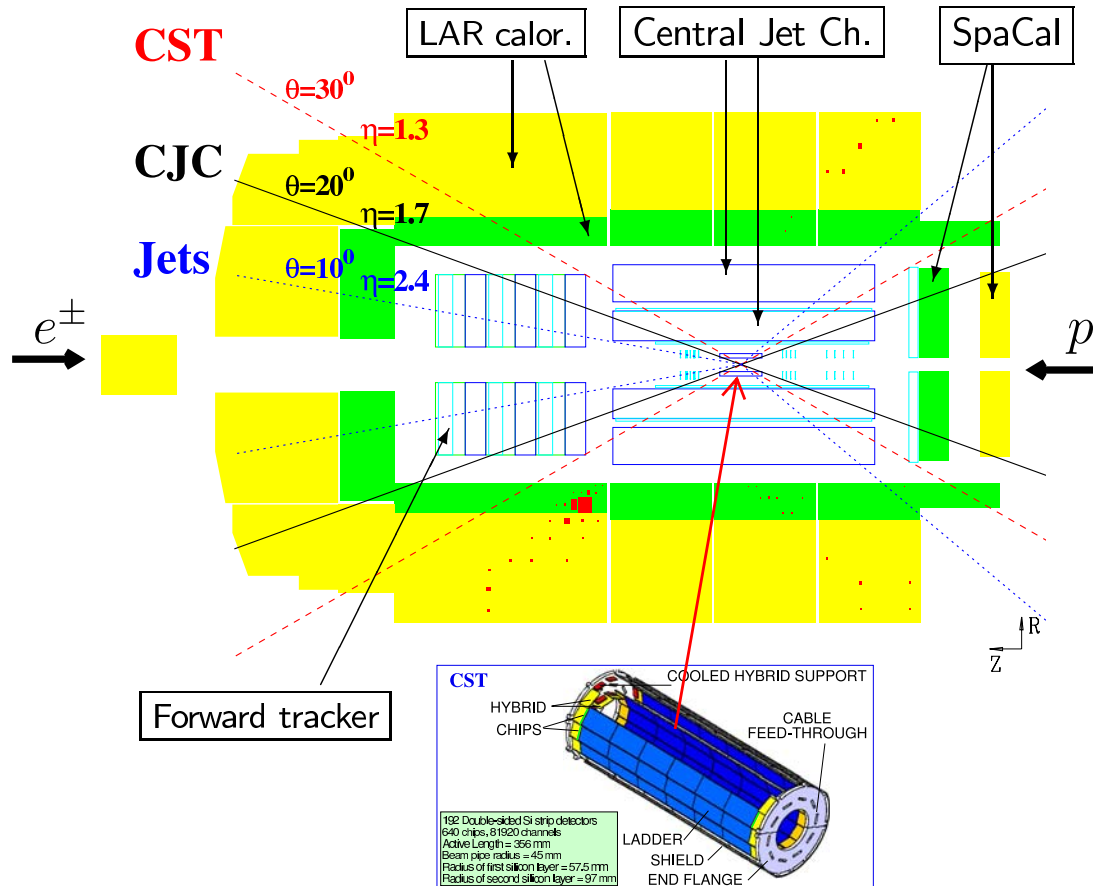


Figure 16: rz -view of the tracking system and calorimeters of the H1 detector. The layout of the central silicon tracker (CST) is shown separately below in a larger scale. The dashed and full lines indicate the polar angle acceptance borders for tracks measured with high quality in the CST and the central drift chambers (CJC), respectively. The dotted lines indicate the typical minimal and maximal polar angles for selected jets which are reconstructed in the Lar calorimeter.

of the most important benchmarks of the H1 and ZEUS detectors, such as polar angle coverage and momentum and energy resolutions are listed in table 1. In the following the main components of the H1 and ZEUS detectors are discussed with emphasis on the advantages of the respective designs:

	H1	ZEUS
Central Si-detector:		
θ -coverage	[30°, 150°]	
η -coverage	[-1.3, 1.3]	
Drift-chambers:		
θ -coverage	[20°, 160°]	[15°, 165°]
η -coverage	[-1.74, 1.74]	[-2.03, 2.03]
$\sigma(p_T)/p_T$	$0.006p_T \oplus 0.015$	$0.0058p_T \oplus 0.0065 \oplus 0.0014/p_T$
Calorimeters:		
θ -coverage	[4°, 154°]	[2.6°, 176.2°]
η -coverage	[-1.46, 3.35]	[-3.4, 3.79]
El.-magn. $\sigma(E)/E$	$0.12/\sqrt{E}$	$0.18/\sqrt{E}$
Hadronic $\sigma(E)/E$	$0.5/\sqrt{E}$	$0.35/\sqrt{E}$
θ -coverage	[153°, 177.8°]	
η -coverage	[-3.95, -1.43]	
El.-magn. $\sigma(E)/E$	$0.07/\sqrt{E}$	

Table 1: Selected benchmarks of the H1 and ZEUS detectors which are relevant for the heavy flavour physics analyses presented in this review. All transverse momenta p_T and energies E are to be given in units of GeV.

Tracking Chambers: For both experiments H1 (ZEUS) the main tracking chambers are large **Central Drift Chambers** providing up to 56 (78) measurement points for charged tracks. The main differences between H1 and ZEUS are:

- At H1 there are two chambers, inner and outer, while in ZEUS the chamber is divided in nine superlayers. For the HERA I data taking the ZEUS drift chambers have been very reliable, while the H1 jet chambers suffered from a few broken wires, which set for certain periods regions of the inner or the outer chamber out of order. This is one of the reasons, why the ZEUS heavy flavour measurements have usually a higher statistics than comparable H1 analyses.
- For ZEUS a superconducting coil surrounds the tracking detectors and provides a magnetic field of 1.43 Tesla. This is considerably higher than the 1.15 Tesla delivered by the H1 superconducting coil, situated outside the calorimeter. Thus the transverse momentum resolution for charged tracks is somewhat better at ZEUS.
- Four of the nine superlayers of the ZEUS chambers are equipped with stereo wires which are tilted $\sim 5^\circ$ with respect to the beam axis. This provides z -measurement points for tracks with a resolution of ~ 1.5 mm. At H1 the sense

wires are strung parallel to the beam axis and the track z -position measurement is obtained by the division of the charges recorded at both wire ends, yielding a moderate resolution of a few centimeters. Two additional z -drift-chambers are installed to provide for each track a few accurate z -measurement points.

In general ZEUS has achieved with their drift chambers a $\sim 20\%$ better signal mass peak resolution compared to H1, e.g. for the golden decay channel $D^{*+} \rightarrow K^- \pi^+ \pi_s$. Figure 19 shows the signal peak obtained in this channel by ZEUS using a high statistics data sample. The obtained momentum and mass peak resolutions of H1 and ZEUS are comparable to that achieved with other high energy physics detectors at different colliders in the world, e.g. with CDF [42] at TEVATRON and with OPAL [43] at LEP.

Both H1 and ZEUS have installed **Forward Tracking Detectors**, using a set-up of drift-chambers. Their main purpose is to extend the polar angular coverage to angles smaller than 20° , outside the acceptance of the central drift chambers (compare with figure 16), However for both experiments these detectors have not been used for physics analyses. One reason is that due to large amounts of dead material in front of the chambers (≈ 2 radiation lengths in the H1 case) the detectors are swamped with secondary tracks from photon conversions and the efficiency for identifying and measuring good tracks is very low. This means that for both experiments the tagging of heavy quarks in the more forward polar angle region $\leq 20^\circ$ is not possible with the standard method of reconstructing heavy flavoured hadrons from their decays into charged tracks. So one has to restrict in this region to other methods, e.g. by identifying electrons and muons, originating from semileptonic decays of heavy quarks, in the calorimeters or in the muon chambers.

Vertex-detector: The innermost tracking detector of H1 is the **Central Silicon Tracker** (CST) [44]. Its main purpose is to determine the positions of charged tracks at the primary event vertex with sufficient precision to resolve secondary decays of heavy flavoured hadrons. The CST consists of two 36 cm long concentric cylindrical layers of silicon strip detectors, surrounding the beam pipe at radii of 57.5 mm and 97 mm from the beam axis (figure 16). The CST covers a pseudo-rapidity range of $-1.3 < \eta < 1.3$ for tracks passing through both layers. Double-sided silicon detectors provide resolutions of $12 \mu\text{m}$ in $r-\phi$ and $25 \mu\text{m}$ in z . Average hit efficiencies are 97% (92%) in $r-\phi$ (z). For a driftchamber measured track with associated CST $r-\phi$ hits in both layers, the transverse distance of closest approach dca of the track to the nominal vertex in $x-y$ is measured with a resolution of $\sigma_{dca} \approx 33 \mu\text{m} \oplus 90 \mu\text{m}/p_t[\text{GeV}]$, where the first term represents the intrinsic resolution (including alignment uncertainties) and the second term is the contribution from multiple scattering in the beam pipe and the CST; p_t is the transverse momentum of the track. It is interesting to compare the achieved resolutions with that at other experiments in the world. This information is provided in table 2. The track impact parameter resolutions obtained at H1 are comparable to that achieved with the ALEPH [45] detector at LEP, which had installed a Silicon detector of similar

Detector	H1	ALEPH	SLD	CDF
Vertex Detector	Silicon strip $r\phi$ and rz	Silicon strip $r\phi$ and rz	CCD (Pixel) $r\phi$ and rz	Silicon strip $r\phi$ only
# layers	2	2	4	4
vertex det. inner radius	5.7 cm	6 cm	2.8 cm	3 cm
$r\phi$ track impact par. resolution	$33 \oplus 90 \mu\text{m}/p_t$	$25 \oplus 95 \mu\text{m}/p_t$	$11 \oplus 40 \mu\text{m}/p_t$	$13 \oplus 40 \mu\text{m}/p_t$
Collider	HERA ep	LEP e^+e^-	SLC e^+e^-	TEVATRON $p\bar{p}$
Beamspace size				
σ_x	140 μm	100 μm	2 μm	40 μm
σ_y	25 μm	10 μm	1 μm	40 μm
σ_z	12 cm	7 mm	0.7 mm	30 cm

Table 2: Comparison of the Silicon vertex detectors at different experiments in the world, using information from [47].

design. The resolutions obtained with the SVD2 [46] Silicon pixel detector of the SLD experiment at SLAC and with the CDF Silicon vertex detector are roughly a factor of two better, mainly due to the smaller distance of the innermost silicon layers to the primary vertex. Table 2 lists also the beam spot sizes, i.e. the spread of the collision points of the beam particles at the different colliders. This spread is of high importance for the secondary vertexing analyses since it affects the knowledge of the primary event vertex. The x and y beam spot sizes of HERA are roughly comparable with the ones at LEP. The x size is that large at HERA, that the knowledge of the ep -collision point can be considerably improved eventwise in a primary vertex fit, combining the information of the average beam spot position with that of selected tracks, as detailed in [48]. The z -hit information of the CST is usually not used for secondary vertex analyses, due to the modest hit efficiency and difficulties to associate the correct CST z -hits to the track. For ZEUS a silicon tracker is only available for the HERA II data period, which is discussed in section 6.

Calorimeters: The tracking detectors are surrounded by calorimeter systems, which cover almost the full solid angle. Their main tasks are to identify and measure the scattered electron, to reconstruct the hadronic final state (e.g. jets) and to separate leptons from hadrons. At H1 a fine-grain liquid argon (LAr) sandwich calorimeter is installed in the central and forward region and supplemented in the backward region with the lead-scintillating fibre calorimeter SpaCal [49]. Both calorimeters have inner electromagnetic and outer hadronic sections. In the ZEUS detector the solenoid is surrounded by a compensating uranium-scintillator calorimeter. The energy scales of

the H1 and ZEUS calorimeters are known accurately at the level of a few percent or better and are calibrated from the data using kinematic constraints. In practice, both calorimeter systems have performed very well.

The ZEUS beam-pipe calorimeter (BPC) is a small tungsten-scintillator sampling calorimeter located about 5 cm from the beam line just upstream of the main calorimeter. This calorimeter enables ZEUS to tag events at very low photon virtuality Q^2 in the region $0.05 < Q^2 < 0.7 \text{ GeV}^2$ and thereby to map the transition region from photoproduction to DIS.

Muon systems: To identify muons both experiments have installed inside and outside the magnetic return yoke large arrays of limited streamer tubes, which cover polar angles from the backward to the forward region and measure muons efficiently for transverse momenta $\geq 2 \text{ GeV}$. For the H1 detector these muon systems are shown in figure 15 (marked as 9).

Luminosity measurement: The luminosity determination is based on the measurement of the bremsstrahlung process $ep \rightarrow ep\gamma$. The photon and the electron are measured in dedicated detectors 30 and 100 metres away from the main detectors, respectively.

Particle identification: Particle identification is provided by several of the aforementioned subdetectors:

- The central drift chambers provide dE/dX information for charged tracks with a resolution of about 8%.
- The muon chambers provide good muon identification for transverse momenta $\geq 2 \text{ GeV}$. In this momentum region the fraction of hadrons which are misidentified as muons is less than 1 %. This background is dominated by kaons and pions which decay in flight into muons somewhere in the detector. For momenta 1-2 GeV the muons can be still effectively identified in the calorimeters, using their 'minimum ionising particle' signatures and obtaining a muon fake probability for hadrons of at most a few percent.
- Charged pions and electrons can be very well separated in the calorimeters using their different shower behaviour.

Trigger and readout system: Both H1 and ZEUS have installed multilevel trigger and readout systems using special information from the detectors. These systems have the following general capabilities:

- They monitor each bunch crossing (10.4 MHz rate) and are able to select the interesting ep collision events.
- They efficiently reject interactions of the proton beam with residual gas inside the beam pipe. This is the dominant background source yielding a trigger input rate of about 100 kHz.
- The final output rate of the trigger is limited to ~ 10 Hz. This makes it possible to trigger on each ep scattering with sufficiently high $Q^2 \geq 10 \text{ GeV}^2$, since the rates are small enough. However, for lower Q^2 , only a fraction of all events can be retained. Nevertheless there are still means to trigger at low Q^2 on specific event classes, such as heavy flavour production, due to the characteristic signatures, e.g. the presence of a number of charged tracks. This is one of the big advantages of H1 and ZEUS compared to e.g. the CDF experiment at the TEVATRON proton antiproton collider, where the triggering of heavy flavour events relied for Run I mainly on high transverse momentum leptons, thus restricting the kinematic acceptances to c and b quarks with high transverse momenta of typically above 10 GeV.

There are several **special trigger detectors and systems** installed for providing fast information at the first trigger level, where for each bunch crossing a decision has to be taken:

- The calorimeters provide energy and timing information. Here a main advantage of the ZEUS trigger compared to H1 is the fast readout of the Uranium scintillating calorimeter, which allows to trigger at the first level on energy deposits from single particles or jets with total energy of a few GeV. This enables ZEUS to measure charm production in 'untagged' photoproduction i.e. without detecting the scattered electron, but instead relying on the jets initiated by the produced charm quarks. For H1, to measure charm photoproduction, mostly the small angle electron detector ($z = -33$ m) is exploited, which can tag the scattered electron in the kinematic range $0.3 < y < 0.6$ and $Q^2 < 0.01 \text{ GeV}^2$, albeit with limited acceptance ($\leq 30\%$). This is the reason why the ZEUS photoproduction charm analyses have often a factor ~ 10 more available statistics than comparable H1 measurements.
- H1 has installed several multiwire proportional chambers which are sensitive to signals from charged tracks originating from ep collisions. The central drift chambers provide also trigger information based on track segments in the r - ϕ plane. Similarly for ZEUS, a drift chamber trigger is installed, which determines the number of tracks and whether they originate from the ep interaction. For H1 the charged track trigger signals are essential for the measurements of heavy flavour production in the kinematic region $2 < Q^2 < 100 \text{ GeV}^2$.

- Muons from semileptonic heavy flavour decays can be triggered with efficiencies of above 50% for transverse momenta $p_T > 2$ GeV, using the signals from dedicated systems in the muon chambers. This is mainly exploited for beauty analyses.

At the final trigger level a complete event reconstruction is performed and additional selections can be applied to reduce the rate, for instance one can require the presence of a candidate for the golden decay channel $D^{*+} \rightarrow K^- \pi^+ \pi_s$.

4 Heavy flavour Tagging methods

In this section the charm and beauty tagging methods are discussed which are used for the measurements presented in this article. There are five basic tagging methods (figure 17):

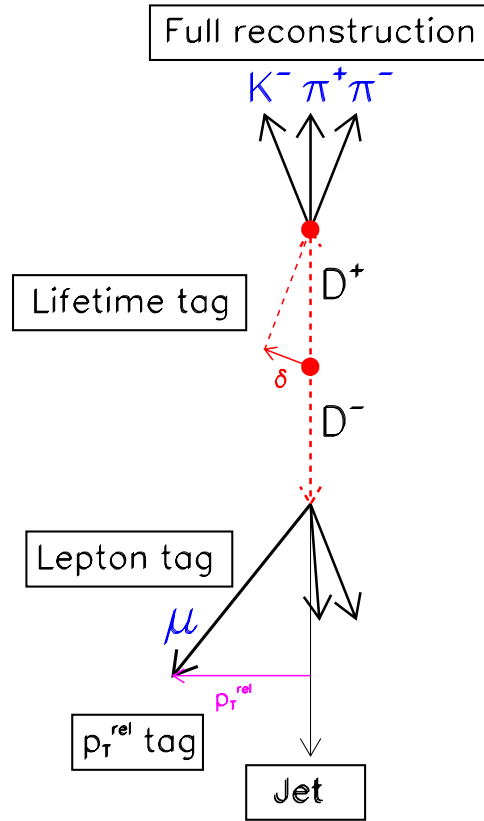


Figure 17: Basic tagging methods for heavy flavour events.

1. **Full reconstruction** of decays of heavy flavoured hadrons in charged tracks, e.g. $D^+ \rightarrow K^- \pi^+ \pi^+$. This is used at HERA only for charm tagging. For beauty the obtainable statistics for fully reconstructed b -hadrons is too small due to the comparably low beauty production rates and the little branching ratios for suitable decay channels.
2. **Lepton tagging**, using muons or electrons from semileptonic b and c decays. This is mainly used for beauty tagging, since b decays produce leptons of relatively high momenta that can be well identified.
3. **Lifetime tagging**, exploiting the long lifetimes of c and b quarks, which lead to displaced secondary decay vertices. These tags are based either on the full reconstruction of the secondary vertex from the charged decay tracks, or on the displaced signed impact parameters δ of charged tracks, i.e. their distances to the primary vertex (see figure 17).

4. p_T^{rel} **tagging**, using the relative transverse momentum p_t^{rel} of leptons (muon or electron) to the axis of the associated jet. This is used for beauty tagging and exploits the large beauty mass which transfers to large p_t^{rel} values.
5. **Jets** are not a heavy flavour tag, but are needed to estimate the heavy quark direction for the lifetime method based on the signed track impact parameters and the p_t^{rel} method. The jets are used in general as a tool to tag and measure the kinematics of outgoing hard partons which are produced or scattered in the interaction. If combined with one of the above tagging methods then a heavy quark jet is tagged. For some measurements presented in this article, a heavy quark tag is combined with requiring in the event a jet, which is not associated to the tagged heavy quark, but represents another hard parton which may be the partner heavy quark or a light quark or a gluon. This additional parton allows to study the production dynamics in heavy flavour events in more detail.

The above methods are all based on measuring the decay particles of *one* heavy quark (single tag). One can also tag *both* heavy quarks (double tag) in an event, by applying one method to tag one heavy quark and another (or the same) for the other heavy quark. This allows to study the correlated production of the heavy quarks in-depth, but the double tagging efficiencies are low.

In the following the different tagging methods are discussed in more detail with emphasis on the advantages and disadvantages of each method.

4.1 Charm tagging with full reconstruction of the golden D^{*+} decay channel

Most of the HERA charm results so far have been made with using the *golden decay channel* $D^{*+} \rightarrow D^0 \pi_s^+ \rightarrow (K^- \pi^+) \pi_s^+$, where all the three decay particles K^- , π^+ and π_s^+ are measured in the H1 or ZEUS central drift-chambers. Due to the small energy release in the decay $D^{*+} \rightarrow D^0 \pi_s^+$ the phase space for combinatorial background is suppressed, providing an excellent signal to background ratio. An event with a D^{*+} candidate recorded by H1 is shown in figure 18 together with the boson gluon fusion diagram (top left), the assumed production mechanism. The scattered electron is clearly visible in the backward calorimeter; this is a DIS event with a photon virtuality $Q^2 \approx 30 \text{ GeV}^2$. The display shows also the charged tracks as measured in the drift chambers. The three D^{*+} decay tracks are marked separately. Furthermore the energy deposits in the Lar calorimeter cells are depicted. In this event there are no very high energy deposits or collimated jets visible. This is typical since at HERA most of the charm quarks are produced with low transverse momenta of a few GeV. The following or similar cuts are applied in the physics analyses:

- The direction of the reconstructed $D^{*\pm}$ candidate is restricted to $|\eta(D^{*\pm})| < 1.5$ to ensure a good acceptance of the decay tracks in the drift chambers.

- For an efficient tracking a cut $p_T(\pi_s) > 120$ MeV is applied, which effectively restricts the transverse momentum of the D^{*+} to be above 1.5 GeV.
- The invariant mass of the $K\pi$ combination has to be consistent with the nominal D^0 mass within two to three sigma of the detector resolution. The resolution is about 25 MeV.

Figure 19 shows the D^{*+} mass peak obtained by ZEUS for such a selection in the analysis [50], using the total HERA-I data sample and all available triggers. For the mass peak the observable

$$\Delta m = m(K^\mp \pi^\pm \pi_s^\pm) - m(K^\mp \pi^\pm)$$

is chosen, which provides a good mass resolution due to the partial cancellation of the K and π track errors. The number of signal events is determined by counting the number of events in the signal region (shaded area in figure 19) after subtracting the combinatorial background, which is estimated from the Δm distribution of 'wrong charge' $K^\pm \pi^\pm \pi_s^\mp$ combinations, which fulfill all other cuts. Alternatively fits are used with a gaussian shape for the signal and a phenomenological function for the background. The signal found by ZEUS for the inclusive HERA I data data sample shown in figure 19 is 42730 ± 350 D^{*+} candidates. This is the statistically most significant heavy flavour sample which is available at HERA. It is also in comparison with other experiments at different colliders in the world one of the biggest samples collected in this decay mode.

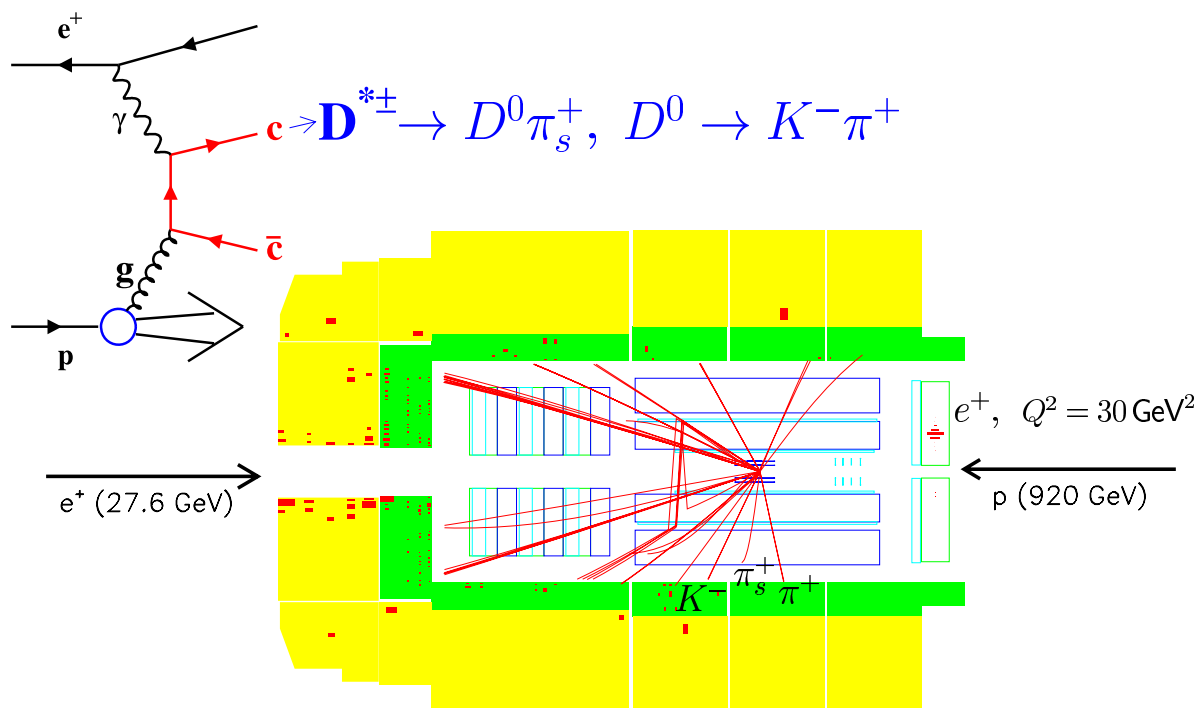


Figure 18: D^{*+} event candidate in the H1 detector display (r - z view) together with the boson gluon fusion diagram (top left), the assumed production mechanism. The cluster from the scattered electron in the backward calorimeter indicates that this is a deep inelastic scattering event; the photon virtuality is measured to be $Q^2 = 30 \text{ GeV}^2$. The display shows also the charged tracks as measured in the drift chambers. The three D^{*+} decay tracks are marked separately. Furthermore the energy deposits in the Lar calorimeter cells are depicted.

In summary the advantages of this tagging method are:

1. The full reconstruction allows to accurately determine the momentum of the D^{*+} , which in turn can be used to estimate the kinematics of the mother charm quark after a correction for the fragmentation.
2. An excellent signal to background ratio of $\sim 1 : 1$ can be achieved, as for the sample in figure 19. This is calculated from the counted number of signal and background events in a two sigma window around the peak.
3. The mass peak signal can be used as an efficient tool in the online filtering of events to reduce the trigger rates.

The disadvantages are:

1. The total branching ratio for the golden decay channel is only $\sim 2.5\%$ [51]. This has to be multiplied with the fragmentation fraction $f(c \rightarrow D^{*+}) = 0.235$ [51] to obtain a total fraction of 0.6% of charm quarks that end up in this decay channel. Furthermore the kinematic and geometric acceptances of the three decay tracks

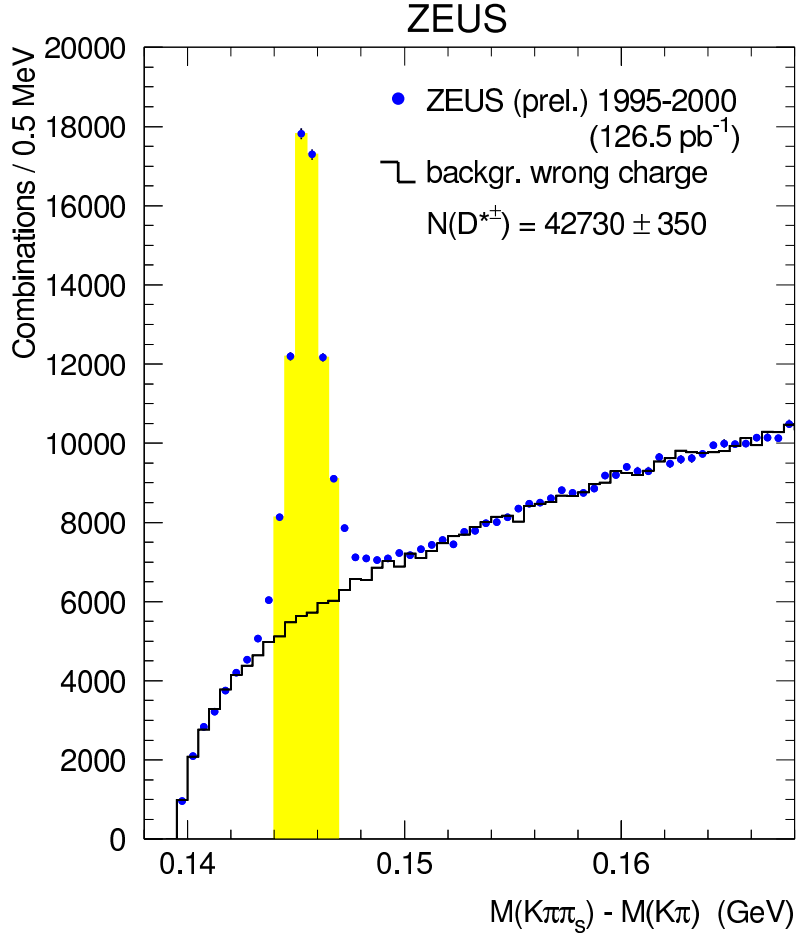


Figure 19: Total inclusive D^{*+} sample obtained by ZEUS for the HERA I data period in the golden decay channel $D^{*+} \rightarrow D^0 \pi_s^+ \rightarrow (K^- \pi^+) \pi_s^+$, from the analysis [50].

reduce the visible fraction to $\leq 0.2\%$. Thus only a very small fraction of charm quarks can be tagged with this method.

4.2 Charm tagging with full reconstruction of D-mesons + lifetime tag

For all other charm hadron decay channels the background situation is much worse compared to the D^{*+} golden decay channel, when the selection is only based on the momenta of the charged decay tracks. As an example for this the D^+ signal in the decay channel $D^+ \rightarrow K^- \pi^+ \pi^+$ is shown in the left plot of figure 20 as obtained by H1 in [48] after the standard track selection cuts. The D^+ signal is sitting on top of a huge combinatorial background, making a significant and reliable signal determination impossible. A way to improve the situation is to combine the full decay channel reconstruction technique with a method that exploits the sizable lifetime of the D^+ -meson, which makes it distinguishable from the combinatorial background that is dominated

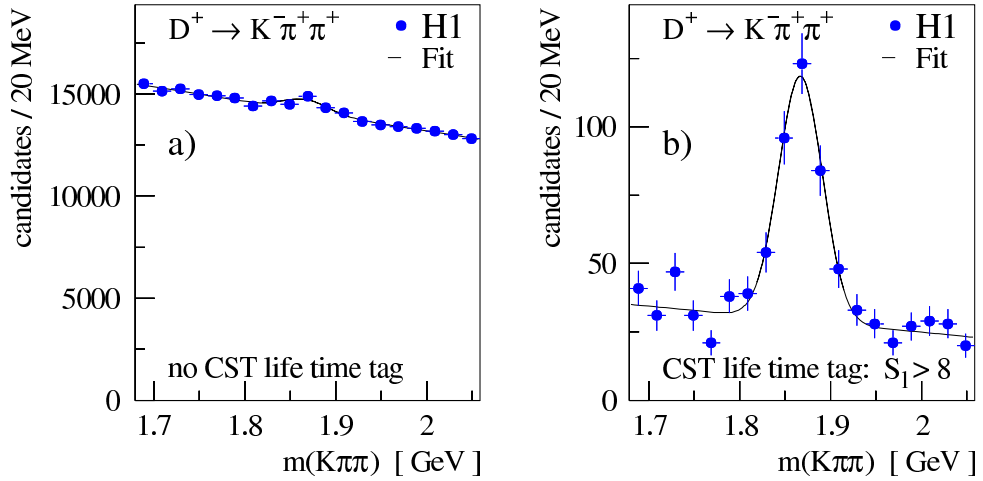


Figure 20: Invariant mass distributions $m(K\pi\pi)$ for $D^+ \rightarrow K^-\pi^+\pi^+$ decay candidates as obtained by H1 in [48]. On the left the distribution is shown before and on the right after a cut on the decay length significance $l/\sigma(l) > 8$.

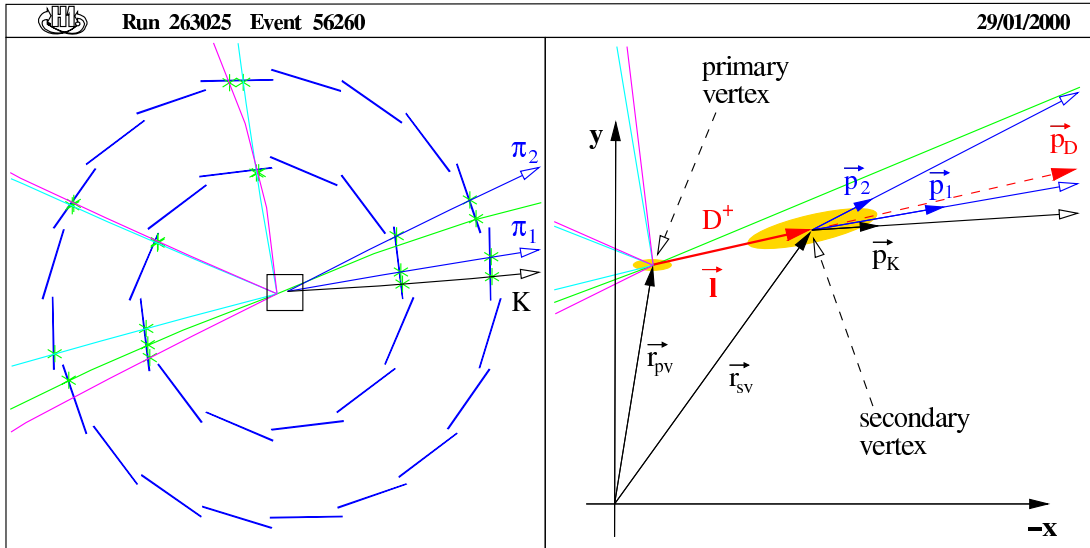


Figure 21: An event with a $D^+ \rightarrow K^-\pi^+\pi^+$ decay candidate is shown, from [48]. To the left a schematic $r\phi$ -view of the H1 central silicon tracker (CST) including hits (stars) and tracks (lines) is displayed. The area magnified to the right is indicated by the box in the center. The right plot illustrates the primary and the D^+ secondary decay vertex reconstruction. The errors of the primary and secondary vertex positions (shaded ellipses) have been blown up by a factor of 10 for illustrative reasons. The reconstructed transverse momentum of the D^+ candidate is $p_T(D^+) = 3.34 \pm 0.02$ GeV and its radial decay length is measured to be $l = |\vec{l}| = 4.8 \pm 0.3$ mm.

by light quark events and where most of the tracks originate from the primary vertex. In [48] the displaced secondary vertex of the D^+ meson is reconstructed from the three daughter particle tracks, which are measured with high precision in the H1

central silicon tracker (CST). The precise silicon tracking is illustrated in the left plot of figure 21 for a D^+ candidate event while in the right plot the primary and secondary vertex reconstruction is sketched. The signal in the right plot of figure 20 is obtained after cutting on the significance $S = l/\sigma(l) > 8$, where l is the reconstructed D^+ decay length and $\sigma(l)$ the calculated error of l . The signal-to-background improves by this cut by a factor 50, while 20% of the signal is retained. For the cross-section measurements in [48] less stringent cuts are applied to increase the efficiency, albeit with a reduced purity. This background suppression technique is applied in [48] also for the measurement of D^0 , D_s and D^{*+} production in the respective decay channels $D^0 \rightarrow K^-\pi^+$, $D_s \rightarrow \phi\pi^+ \rightarrow K^+K^-\pi^+$ and the golden decay channel $D^{*+} \rightarrow D^0\pi_s^+ \rightarrow (K^-\pi^+)\pi_s^+$.

In summary the advantages of this tagging method are:

- A similar good signal to background ratio $\sim 1 : 1$ can be obtained for the other D-mesons as for the D^{*+} golden decay channel.

The disadvantages are:

- The branching ratios of the selected decay channels are in the order of a few percent and thus only a small fraction of events with charm quarks is tagged.
- The total efficiency for all the lifetime tagging selection cuts is only of the order of 10%. An alternative to the lifetime based selection is to apply harder kinematic cuts on the momenta of the D -mesons and daughter tracks and hereby to improve the signal to background ratio in the mass distributions. This approach is pursued by ZEUS in [96]. However the achieved signal to background ratio is still not better than $1 : 20$. Thus with or without using the additional lifetime tag, the statistical significances of the fully reconstructed charmed hadron decays of all other decay channels are rather marginal in comparison to the golden D^{*+} decay channel. This is the reason, why the measurements using these decay channels focus mainly on the question of the relative production rates of the different charm hadrons D^{*+} , D^0 , D^+ , D_s and λ_c , i.e. on the fragmentation, but not on the perturbative QCD aspects, that are studied alone with using the D^{*+} golden decay channel.

4.3 Beauty tagging with lepton + p_t^{rel} + lifetime tag + jets

A well established method to identify beauty quarks is to select a muon with high transverse momentum of typically above 2 GeV from semileptonic b -quark decay which is associated with a jet that represents the beauty quark and consists of the muon and further final state particles. For the measurements in photoproduction, such as in [52], usually two jets are required, of which one contains the muon. In the leading order pQCD picture one selects with this directly the two outgoing b -quarks produced in the

PGF process (figure 1 left). Figure 22 shows in the left plot the standard H1 detector display of such a beauty event candidate from the analysis [52]. This event is classified as photoproduction, i.e. $Q^2 \approx 0 \text{ GeV}^2$; the electron is scattered under a small angle and remains undetected. The muon with a transverse momentum of $\sim 5 \text{ GeV}$ is well identified in the muon chambers. The two jets are visible in the lego plot of the Lar calorimeter energy deposits in the ϕ - η plane. The plot in the middle-right of figure 22 shows the charged tracks as measured with the central silicon tracker in the transverse plane. A small region is shown of a few millimeter extension around the ep beam spot center, which represents the average ep collision point. The tracks are plotted as thick lines, which start at their closed distance to the beam spot center. The widths of the lines indicate the spatial resolutions of the tracks. A couple of tracks are clearly not in agreement with originating from the primary vertex but indicate the presence of two secondary b -quark decay vertices.

After the muon and jet selection there is still significant background from charm events with a genuine muon from semileptonic c -decay and from light quark events with a fake muon, i.e. a hadron (mainly π^+ or K^+) misidentified as a muon. To determine the beauty contribution in the sample, two observables are used which exploit the large mass and the long lifetime of the beauty quark, respectively, and which are illustrated in the sketch on the right of figure 22:

1. The transverse momentum p_t^{rel} of the muon with respect to the axis of the associated jet. For muons from b -decays the p_t^{rel} spectrum extends to much larger values than for the other sources.
2. The signed impact parameter δ of the muon track in the transverse plane with respect to the primary vertex. The sign is defined as positive (negative) if the muon track is crossing the axis of the associated jet 'downstream' ('upstream') from the primary vertex, i.e. in the direction (opposite direction) of the jet. For muons from b -decays δ takes larger positive values as compared to the other sources.

The latter variable is only used by H1, where the central silicon vertex detector provides the necessary track resolution. Finally, the relative contributions of beauty and background in the data are determined from likelihood fits to the above observables. H1 uses in [52] a fit to the two-dimensional distribution of p_t^{rel} and δ , which leads to an improved beauty separation. The results of this fit are illustrated in figure 23, for the photoproduction sample. The contributions from beauty, charm and light quark events, with respective fractions of about 30%, 50% and 20%, are indicated. At large positive values of δ and at large values of p_t^{rel} , the beauty component (dashed line) becomes dominant.

In summary the advantages of this method are:

- The relative large branching ratio $BR(b \rightarrow \mu X) \sim 22\%$ [51], which includes $b \rightarrow cX \rightarrow \mu X$ and other cascade decays, provide a reasonable tagging efficiency for b quarks.

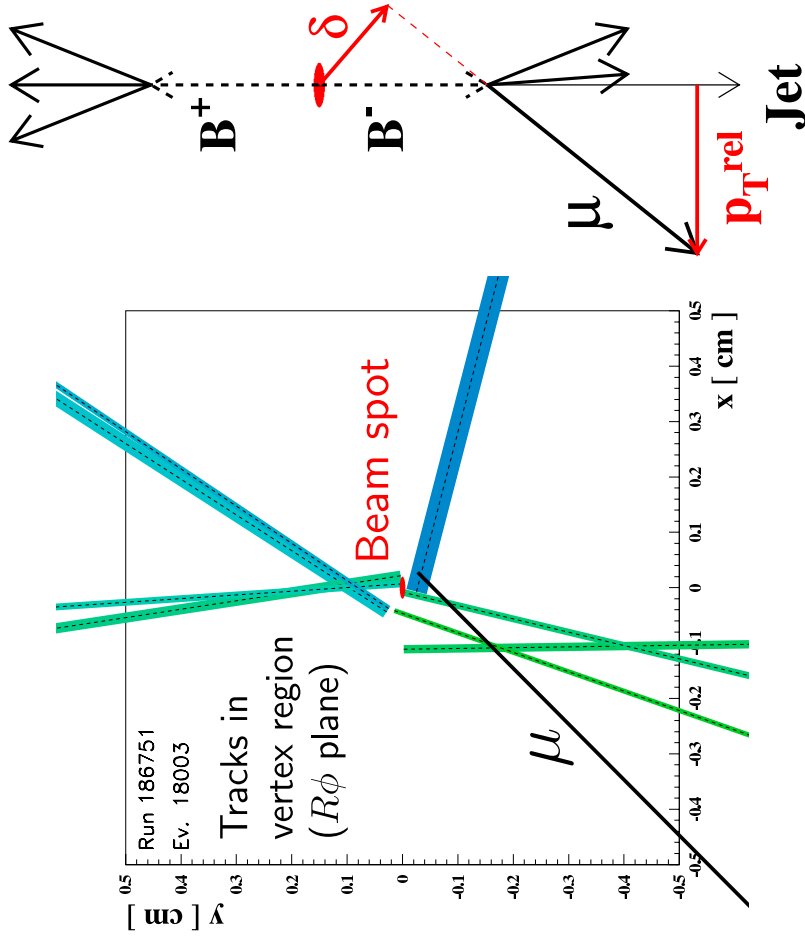
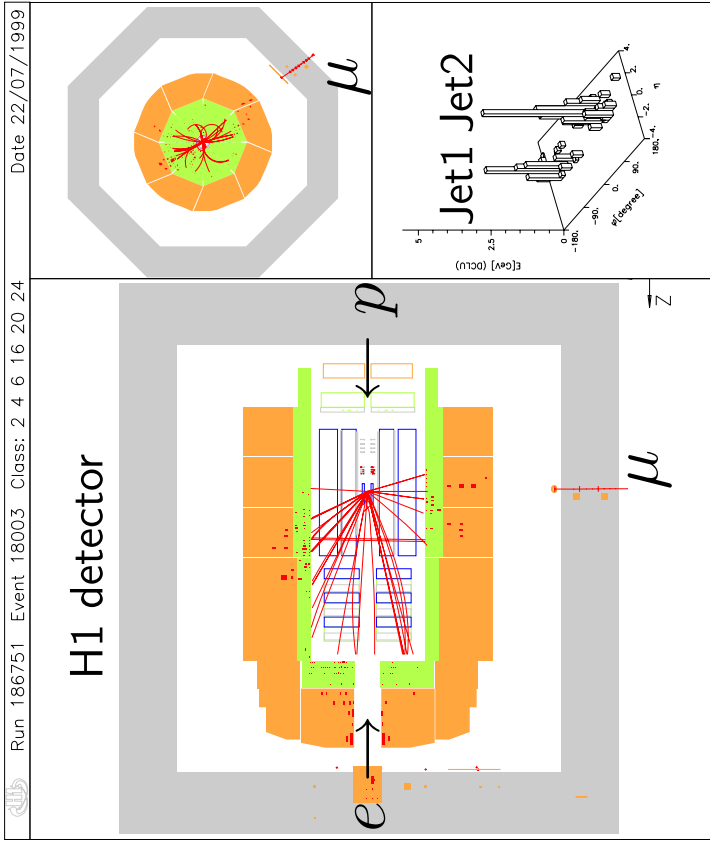


Figure 22: Beauty candidate event with a muon and two jets in the final state, from the H1 analysis [52]. On the left the event is shown in the standard H1 event display. The plot in the middle-right shows the charged tracks as measured with the central silicon tracker in the transverse plane. A small region of a few millimeter scale is shown around the e_p beam spot center, which represents the average ep collision point. The tracks are plotted as thick lines, which start at their closed distance to the beam spot center. The widths of the lines indicate the spatial resolution of the tracks. The sketch on the very right of the figure illustrates the two beauty tagging observables δ and p_t^{rel} .

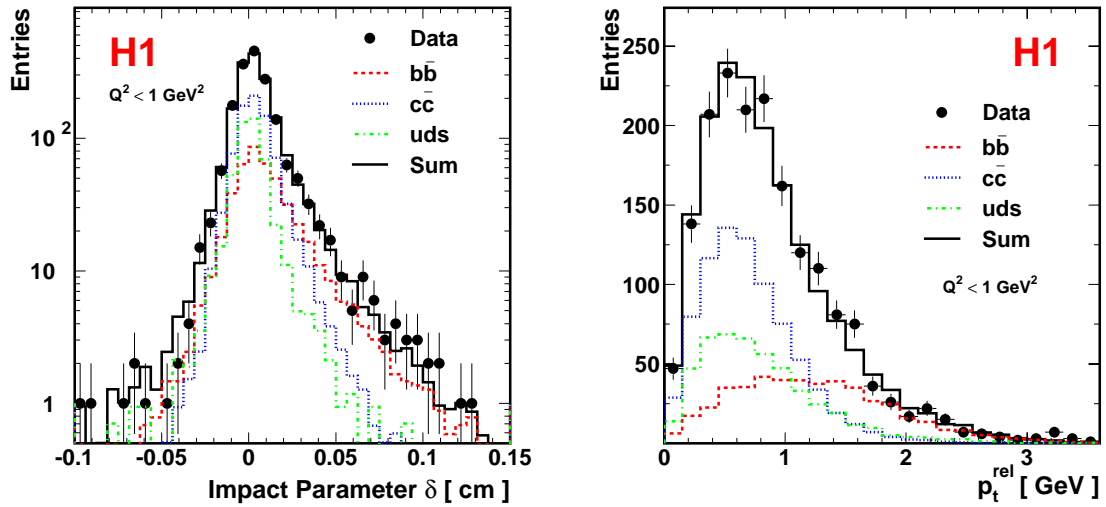


Figure 23: Distributions of the impact parameter δ of the muon track (left) and the transverse muon momentum p_t^{rel} relative to the axis of the associated jet (right) for the photoproduction event sample of the H1 beauty analysis [52]. Included in the figure are the estimated contributions of events arising from b quarks (dashed line), c quarks (dotted line) and the light quarks (dash-dotted line). The shapes of the distributions of the different sources are taken from a PYTHIA [25] Monte Carlo simulation and their relative fractions are determined from a fit to the two-dimensional data distribution of p_t^{rel} and δ .

- The clean experimental signature of high p_T muons in the detectors, which distinguishes very well from hadrons and thus allows to suppress light quark events. Charm events with genuine muons from semileptonic charm decays are very effectively suppressed by the high p_T cuts. With the muon and jet selection alone a beauty purity of $\sim 25\%$ is achieved. The remaining charm and light quark background is well distinguishable from the beauty signal by using the p_t^{rel} and δ observables.
- Muons can be also tagged outside the polar acceptance of the central trackers, i.e. for $|\eta| > 1.5$, which are covered by the muon systems, thus providing access to more forward and backward beauty quark production.

The disadvantages are:

- An efficient identification of muons and electrons in the detectors is typically only possible above a minimal momentum of 1 – 2 GeV. This restricts the kinematic acceptance, favouring events with larger b -quark momenta.
- For the p_t^{rel} and δ observables the direction of the jet, with which the muon is associated, must be reconstructed with sufficient precision. This is only achieved

for jets with p_T of roughly larger than 5 GeV, which sets a lower border for the b -quark transverse momenta probed in these analyses.

Instead of using muons, electrons from semileptonic b -decays can also be used. This has been done by ZEUS in [53], where the electron is identified using the drift chamber dE/dX measurement and the calorimeter shower information. In this analysis the p_t^{rel} observable is used for determining the beauty contribution to the final event sample.

4.4 Charm and Beauty with inclusive lifetime tagging

The methods presented above all suffer from the fact that only a fraction of the charm or beauty quark decays leads to the selected final state. This can be avoided by using an *inclusive tagging method*, based on the long lifetime of charm and beauty quarks. The H1 collaboration has pioneered a new practical method for this in the measurement [54] of the charm and beauty contributions to the proton structure function F_2 at high photon virtualities $Q^2 > 150 \text{ GeV}^2$. In this method, charged tracks are used with transverse momenta $p_T > 500 \text{ MeV}$. For each track two silicon r - ϕ -hits have to be associated and it is required that the combined drift chamber silicon r - ϕ -track fit probability exceeds 10%, ensuring a high quality reconstruction. In figure 24 the transverse momentum spectrum of the selected tracks is displayed, which shows a steep drop-off towards higher momenta, reflecting the underlying physics of the quark production processes. The applied lower momentum cut is a compromise between retaining a

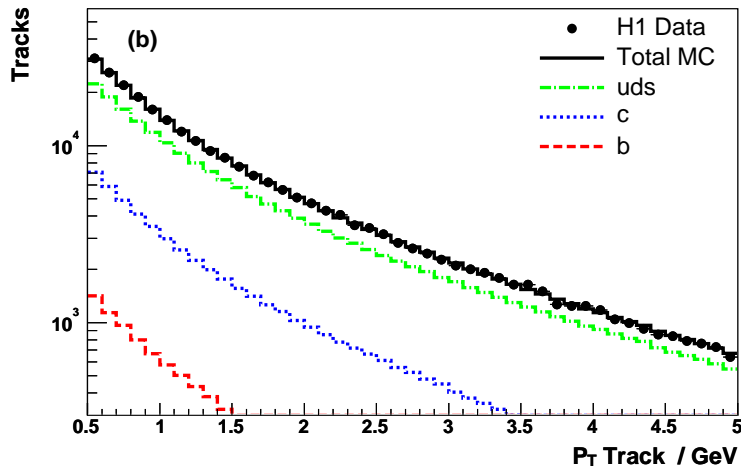


Figure 24: Transverse momentum distribution of the selected tracks in the H1 analysis [54] of charm and beauty production at high photon virtualities $Q^2 > 150 \text{ GeV}^2$. The estimated contributions from beauty, charm and light quark events are also shown as estimated from a Monte Carlo simulation.

good impact parameter resolution and keeping at the same time a high acceptance for charm and beauty quarks with low transverse momenta. The estimated contributions from light quark, charm and beauty events are also indicated in figure 24. In this flavour inclusive event sample the light quark contribution is dominating while charm contributes $\sim 20\%$ and beauty only $\leq 3\%$. The further steps for the charm and beauty tagging in [54] are:

1. For each event a 'jet axis' is defined, which approximates the direction of a charm or a beauty quark. The jet axis is defined as the direction of the detector jet with the highest transverse momentum above 5 GeV or, if there is no such jet reconstructed in the event, then the direction is estimated from the momentum vector of the sum of all the hadronic final state particles in the detector.
2. Tracks are associated to the jet axis if they lie within a cone of size 1 in η - ϕ space. Only associated tracks are used for the further analysis.
3. To suppress background from strangeness events (K_s^0 and λ decays) a cut is applied on the track impact parameters $|\delta| < 0.1$ cm.
4. For the further analysis the impact parameter significance $S = \delta/\sigma(\delta)$ is used. For optimal statistical precision different significance distributions are used for events with different multiplicities. The first significance distribution S_1 is defined for events where only one track is linked to the jet, and is simply the significance of the track. The second significance distribution S_2 is defined for events with two or more tracks associated with the jet and is the significance of the track with the second highest absolute significance. Only events in which the tracks with the first and second highest absolute significances have the same sign are selected for the S_2 distribution. The S_1 and S_2 distributions are shown in figure 25 on the left. The S_2 distribution provides a better separation of light to heavy quarks. This is due to the effect, that for light quark events often one track with large significance S is observed, but rarely two. On the contrary charm and beauty decays often produce two or more tracks with significant positive impact parameters. The events with one track are retained in the analysis to improve the statistical precision.
5. To eliminate a large fraction of the light quark background and to substantially reduce the uncertainty due to the impact parameter resolution, the negative bins in the S_1 and S_2 distributions are subtracted from the positive. The subtracted distributions are shown in figure 25 on the right. The resulting distributions are dominated by c quark events, with an increasing b fraction towards larger significances. The light quarks contribute only a small component $\leq 10\%$ for all values of significance. Finally the fractions of c , b and light quark events are extracted from a simultaneous χ^2 -fit to the subtracted S_1 and S_2 distributions and to the total number of inclusive events before track selection (this sample is just selected by the scattered electron). The latter information is mainly needed for constraining the light quark contribution.

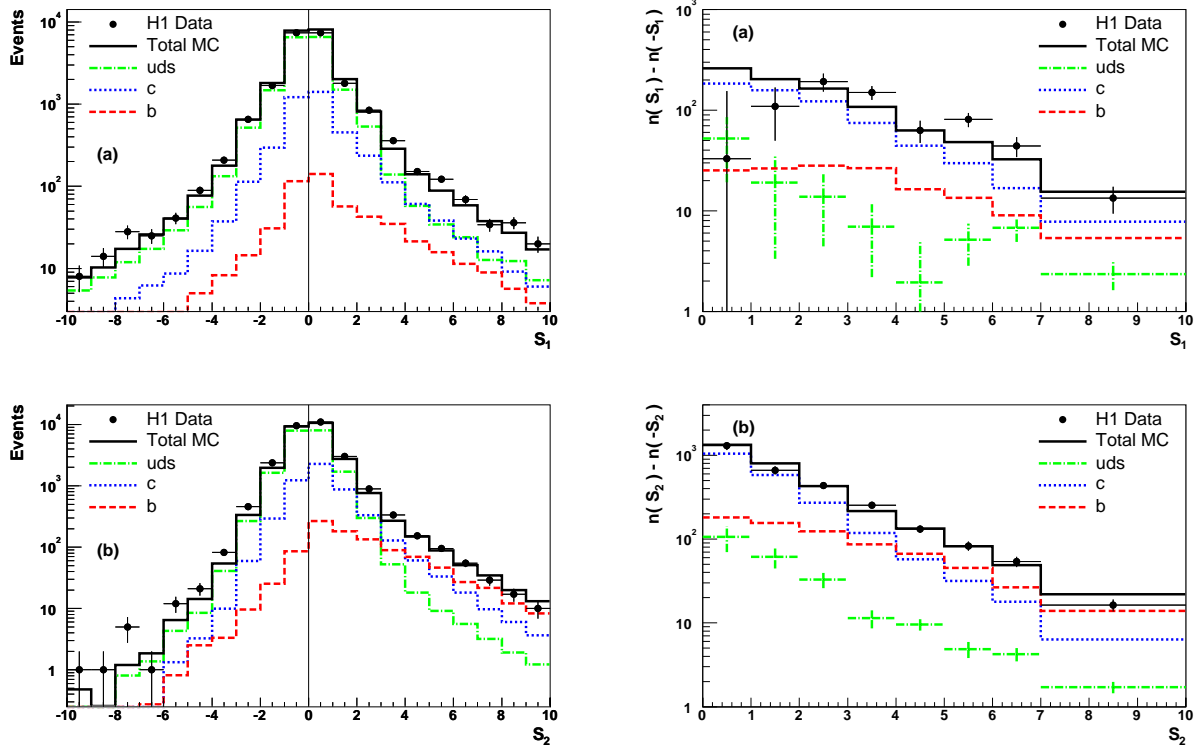


Figure 25: Final distributions used for the charm and beauty tagging in the H1 inclusive lifetime analysis [54] of charm and beauty production at high photon virtualities $Q^2 > 150 \text{ GeV}^2$. The upper left plot shows the significance $S_1 = \delta/\sigma(\delta)$ distribution per event for events that contain one selected track associated to the jet axis. The lower left plot shows the significance $S_2 = \delta/\sigma(\delta)$ distribution per event of the track with the second highest absolute significance for events with ≥ 2 selected tracks associated to the jet. On the right side the S_1 and S_2 distributions are shown after subtracting the negative bins in the S_1 and S_2 distributions from the positive.

Alternative methods have been used as a cross check for this new technique: In the analysis [54] the explicit reconstruction of secondary decay vertices in the transverse plane is applied, using a special technique that avoids a definite assignment of tracks to vertices. In the analysis [55] a multi-impactparameter method [56] as developed by the ALEPH experiment is used. The results obtained with these methods are in agreement with using the subtracted S_1 and S_2 , however are found to be more sensitive to systematical uncertainties from track resolutions and efficiencies.

In summary the advantages of this inclusive lifetime tagging method are:

- With only requiring at least one charged track a large fraction of all charm and beauty events is retained in the selected event sample.
- With the applied track minimal transverse momentum cut of 500 MeV one obtains a good acceptance for low heavy quark momenta, which is of high importance for measuring the charm and beauty contributions to the inclusive ep scattering.

The disadvantages are:

- The total achieved effective signal to background ratio is not better than 1:15 for both charm and beauty. This can be estimated from the numbers of charm and beauty events in the negative subtracted S_1 and S_2 spectra, which effectively represent the numbers of tagged events, and from the errors achieved for the charm and beauty components in the fit.
- The method necessitates a precise understanding of the track resolutions and efficiencies.
- A clear isolation of the beauty component is difficult, which is mainly due to the inclusive nature of the selection and the relatively small beauty production cross sections at HERA. For the analysis [54] shown in figure 25 the beauty component is dominant only in the S_2 distribution in the region $4 < S_2 < 10$, where about 150 beauty events are found, a relatively small fraction of all beauty events.

4.5 Charm and Beauty with double tagging

In the double tagging analyses [57–59] in a large fraction of events *both* heavy quarks are tagged using as signatures either a muon and a D^{*+} reconstructed in the golden decay channel [57, 58] or two muons [59].

$D^{*+} \mu$ analyses: In the photon gluon fusion process $\gamma g \rightarrow c\bar{c}$ or $b\bar{b}$ the two heavy quarks are produced back-to-back in the γg frame as illustrated in figure 26 for the beauty case. Charm and beauty events can be separated by their different charge

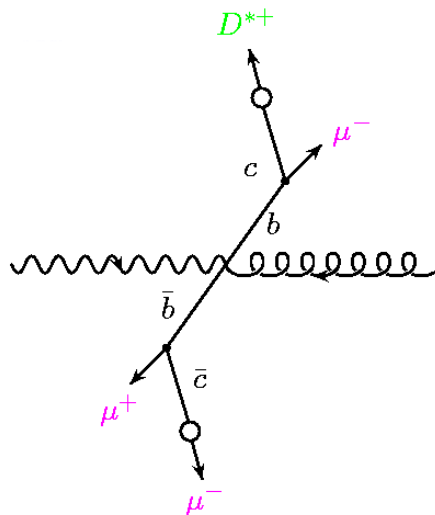


Figure 26: Possible ways to produce a D^{*+} muon pair from the decays of the b - and the \bar{b} -quark produced in the photon gluon fusion process at HERA.

and angular correlations of the selected decay particles, the muon and the D^{*+} . For charm, the muon can only originate from the decay of the opposite charm quark from which the D^{*+} is released. Thus the muon and the D^{*+} have unlike charge signs and are approximately back to back. On the contrary for beauty events, the muon and the D^{*+} can originate from opposite beauty quarks or from the same beauty quark; the muon can stem from a direct $b \rightarrow \mu X$ decay or from a cascade decay $b \rightarrow cX \rightarrow \mu X$; and $\bar{B}^0 - B^0$ mixing can turn the \bar{b} quark into a b . Thus for beauty, the muon and the D^{*+} can have unlike- or like-sign charge and can be opposite or more close in their direction in the γp frame.

In the H1 analysis [57] the data are divided into four correlation regions, where the D^{*+} and the muon either have like- or unlike-sign charge and are either in the opposite or in the same azimuthal hemisphere. The obtained D^{*+} mass peak signals in the four regions are shown in figure 27 on the left. The charm and beauty contributions are

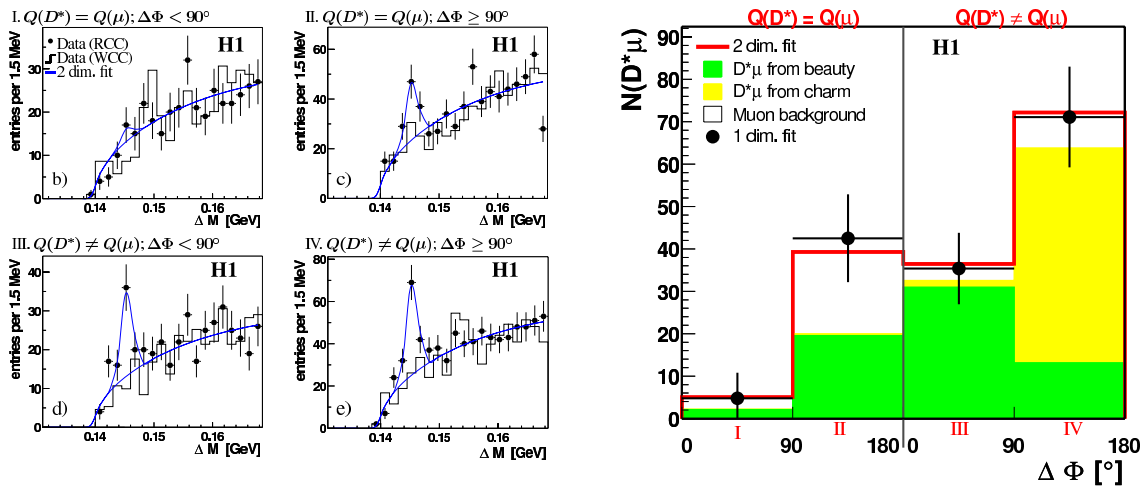


Figure 27: Illustration of the charm and beauty tagging in the H1 analysis [57] using events with a D^{*+} reconstructed in the golden decay channel and a muon. The left four small plots show the D^{*+} mass peak signal distributions, labeled as DATA (RCC), in the four correlation regions, given by the relative charges of the D^{*+} and the muon and the azimuthal angle $\Delta\Phi$ between them. The solid lines are the results of a two-dimensional fit, where for the normalizations of the gaussian functions for the mass peak signals the relative fractions of charm and beauty to the regions are used as predicted by the Monte Carlo simulations of c and b events. The right plot shows the population of the four correlation regions I-IV obtained from the simultaneous likelihood fit in all correlation regions (two-dimensional fit histogram). The resulting decomposition into charm and beauty contributions and the muon background is also shown. The points with error bars are the results of one-dimensional fits of the ΔM distributions in each correlation region.

determined from a simultaneous fit to the D^{*+} mass peak signals observed in the four regions using the division of charm and beauty events over the regions as predicted

by the PYTHIA Monte Carlo simulation. The result of the fit is shown in the right plot of figure 27. A correction needs to be applied for fake muon background contributions. For this the relative fractions of fake muons in charm and beauty events are used as predicted by the Monte Carlo simulation. The simultaneous fit gives a good description of the D^{*+} yields in each bin, that were also separately determined by a fit to the mass peak distribution in that bin only and which are shown in figure 27 as the points labeled as '1 dim fit'. In summary the advantages of this method are:

- The double tagging gives for a large fraction of the events access to the kinematics of *both* heavy quarks. This information can be used to investigate the $c\bar{c}$ and $b\bar{b}$ production processes in more detail.
- Since the D^{*+} alone already provides a clean heavy flavour tag, the muons can be selected in transverse momentum down to ~ 1 GeV with a reasonable purity. For beauty this gives access to much lower quark momenta than for the method of using events with a muon and jets that was discussed in section 4.3.

The disadvantages are:

- The total tagging efficiency is very low. For the H1 analysis [57] only about 150 events are selected for the total HERA I data sample.
- The muon tagging is well suited for the measurement of beauty production but has relatively small acceptance for charm, where the muons have usually small transverse momenta < 1 GeV.
- The correlation between the D^{*+} and the muon momenta with the mother quarks is not as good as for jets.
- Since the fake muon background is subtracted using Monte Carlo simulations, this necessitates a good understanding of this background in the simulation, which is a difficult task.

Beauty tagging with two muons: In the recent analysis [59] ZEUS has pioneered a new method for the double tagging of beauty events with two decay muons. An event candidate from this analysis is shown in figure 28, displaying the clear detector signatures of the two muons. For the beauty measurement it is exploited that the fake muon background is expected to yield the same amount of two muon candidates with like- and unlike-sign charges, while for the beauty signal there are significantly more muon pairs with unlike-sign charges (compare with figure 26). This is observable in figure 29, which shows the distributions of the muon pair invariant masses for unlike- and like-sign events with the estimated beauty signal and background contributions. The total beauty signal is determined using the following procedure:

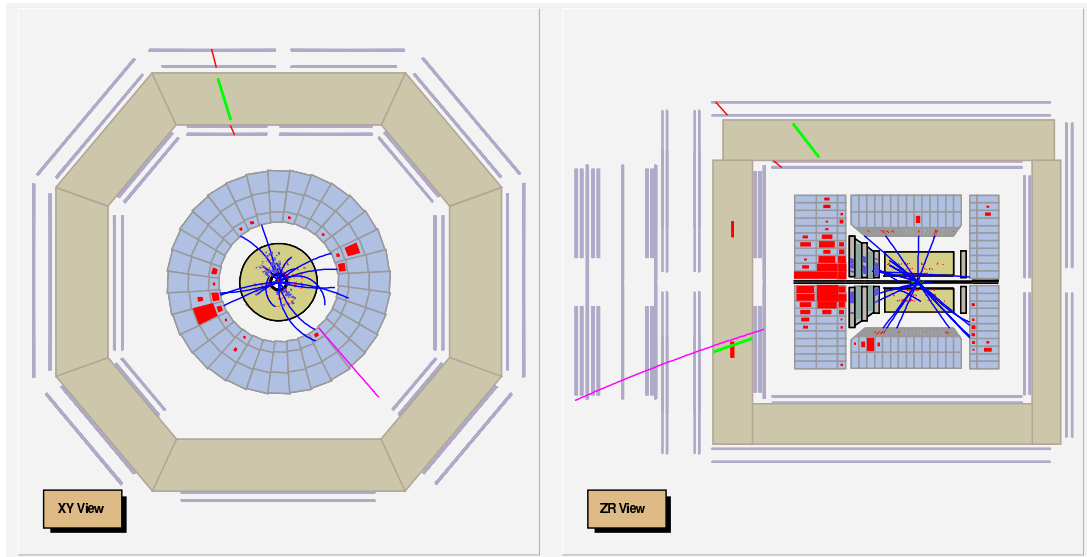


Figure 28: Beauty event candidate with two muons in the final state, from the ZEUS analysis [59].

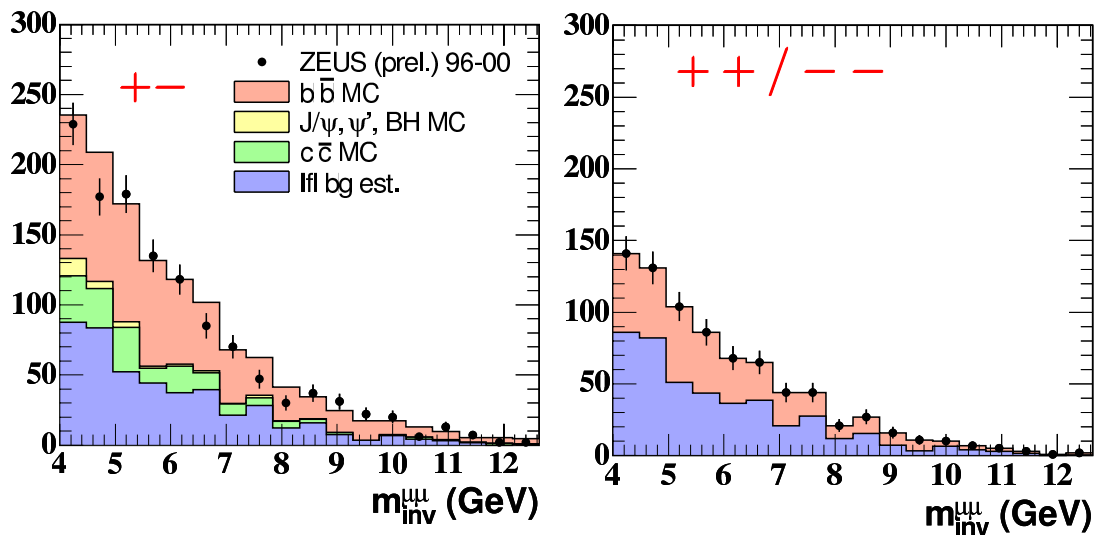


Figure 29: Dimuon invariant mass distribution for unlike sign muon pairs (left) and like sign pairs (right), from the ZEUS analysis [59]. The estimated contributions for the beauty signal and background sources are also shown, as discussed in detail in [59].

1. The number of events with two like-sign muon candidates is subtracted from the number of unlike-sign events.
2. The number of remaining charm and other residual backgrounds is subtracted using Monte Carlo simulations. The simulation of the charm events was verified to provide the correct normalisation with an independent analysis using events with a muon and a D^{*+} , applying a similar tagging method as described above.

3. The pure beauty contribution which is obtained after the subtraction is corrected for its relative acceptance to the total beauty sample.

In summary the advantages of this method are:

- The relatively large branching fractions for semimuonic b -decays retain reasonably high statistics for the signal. In total $\sim 1800 \pm 200$ beauty events are tagged in the analysis [59].
- The double tagging suppresses very effectively background processes. This enables to use muons which are only identified in the calorimeters and thus to extend the muon selection to lower momenta and to the more forward and backward directions. In the ZEUS analysis one muon is required to have a transverse momentum above 0.75 GeV and the second above 1.5 GeV. Both muons are measured in a wide pseudorapidity range from -2.2 to 2.5. In summary the acceptance is good for b -quarks over a large momentum and rapidity range allowing to measure the total beauty cross section as done in [59].

4.6 Jet reconstruction

The today commonly used jet finder by H1 and ZEUS is the inclusive kt algorithm [60, 61]. The basic principle is to merge two particles, represented by their four momentum vectors, to a single object if they are close enough in their direction. The usual way to do this is to require the distance $\sqrt{\Delta\phi^2 + \Delta\eta^2}$ of the two particles in the η - ϕ plane to be smaller than a separation parameter, which is normally set to one. This procedure is repeated until no further merging is possible and the remaining objects are classified as jets. There are different schemes available for adding the four momenta of the particles in the merging step, as described in [62]. In the E -scheme, the four vectors are just added leading to jets with non zero mass. In the p_T -scheme the transverse momenta p_T of the momentum vectors are added and p_T weighted averages are calculated for ϕ and η . In this scheme, the energy of the merged object is set to its three momentum, so that the jets are massless. In practice the differences are not very large and both schemes are used for heavy flavour analyses. The inclusive kt algorithm is known to provide a particular good correlation of the quark momenta with the jets at the hadron level after the fragmentation.

For finding jets in the experimental analyses the jet algorithm is applied to the so-called hadronic final state particles which are measured in the detectors. To define these particles dedicated algorithms [63] are used for combining in an optimal way charged tracks that have typically superior resolution for transverse momenta up to a few GeV with calorimetric information that is more precise at very high particle energies. For more forward or backward pseudorapidities $|\eta| > 1.5$ only calorimetric information is available.

Comparison of achieved tagging efficiencies: Table 3 compares for some selected charm tagging methods the finally achieved tagging efficiencies. The numbers for the

	$D^{*+} \rightarrow K^- \pi^+ \pi_s^+$ golden decay	$D^+ \rightarrow K^- \pi^+ \pi^+$ $D^0 \rightarrow K^- \pi^+$ $D_s^+ \rightarrow K^+ K^- \pi^+$	$D^+ \rightarrow K^- \pi^+ \pi^+, \dots$ + Lifetime tag	Incl. lifetime tag S_1, S_2
Br's	1 %	~ few %	~ few %	10%
Kinematic & geometric acceptance	~ 40%	~ 40 %	~ 40 %	~ 100%
Tagging sel. & efficiency	~ 50%	~ 50%	~ 5%	~ 10%
Total tag. efficiency	$2 \cdot 10^{-3}$	few 10^{-3}	few 10^{-4}	10%
s:b	1:1	1:20	1:1	1:15
equiv. bgfree events efficiency	10^{-3}	few 10^{-4}	few 10^{-4}	$5 \cdot 10^{-3}$

Table 3: Comparison of the achieved charm quark tagging efficiencies for selected methods.

total tagging efficiency and the signal to background ratios are obtained from the final tagged samples, which for the fully reconstructed D -mesons are defined by the number of events in the signal peaks (e.g. figure 19) and for the inclusive lifetime tagging from the negative subtracted S_2 spectra (figure 25). After all, the inclusive lifetime tagging provides the best overall performance in terms of equivalent background free events. This number is calculated from the squared significance, where the significance means the measured number of tagged events divided by its error. The results are based on comparisons of HERA I measurements performed with the different methods in similar event kinematic regions. The inclusive lifetime tagging provides approximately four times larger equivalent background free events than the golden D^{*+} method. For beauty the tagging power of the inclusive lifetime method and the method using events with a muon and jets $+ p_t^{rel} + \delta$ are similar and these two methods provide the most competitive tagging so far.

4.7 Measurement systematic errors

Certain systematic errors are associated with the tagging methods discussed above which propagate into the charm and beauty production cross section measurements which results are presented in the following section. Many of these errors are observed to decrease in parallel with the statistical errors, as usual. The following error sources are the most important ones:

- Normalisation uncertainties:
 - The integrated luminosities are known to $\sim 2\%$.
 - The trigger efficiencies have typical uncertainties of $2-5\%$. The lower values are reached for DIS, where the triggering is based on the scattered electron, while for photoproduction it is mostly based on final state signatures such as muons.
 - H1 assumes a single track efficiency uncertainty of 3% which for analyses with several tracks leads to correspondingly larger errors. This affects mainly the D^{*+} golden decay channel analyses and the beauty analyses with inclusive lifetime tagging. For the latter case total systematic errors of $\geq 10\%$ are found. ZEUS assumes a negligible track efficiency uncertainty.
 - For analyses with high transverse momentum muons the reconstruction efficiencies are known with $5-10\%$ precision.
- Signal determination uncertainties:
 - For the D^{*+} analyses a systematic error of a *few percent* is attributed to the mass peak signal determination. This uncertainty is approximately scaling with the statistical errors.
 - For the lifetime tag based analyses, the knowledge of the track impact parameter resolution is of highest importance. For the inclusive lifetime tagging this leads to average errors for charm of *few percent* which can reach up to 10% and for beauty the errors are $10-20\%$.
- Other uncertainties:
 - QCD model uncertainties in the Monte Carlo simulations that are used to unfold the data (efficiency corrections etc.) lead to systematic errors which are usually of the order of a *few percent* and can reach up to 10% for certain measurement bins.
 - For analyses with jets the hadronic energy scale uncertainty in the calorimeters of a few percent lead to cross section errors for charm and beauty in the order of $3-5\%$.

All the errors are as usually added in quadrature. The total systematic errors are typically $\sim 10\%$ for charm and $20-30\%$ for beauty analyses.

5 Results

In the following the heavy flavour results are discussed, based on the HERA I data samples from the years 1992-2000. The ordering of the results follows the logic to begin with the measurements that probe the perturbative aspects of QCD and then to move to the more non perturbative aspects. The perturbative aspects will be dealt with in a ordering according to a walk through the hard scales of photon virtuality Q^2 and heavy quark mass m_Q as illustrated in table 30. Starting from the softest scales, charm in photoproduction is discussed first. Then the Q^2 scale is raised and charm is studied in DIS. Afterwards beauty production is discussed, first in photoproduction and then, ending with the hardest two scales, in DIS.

$Q^2 \rightarrow$



m_Q \downarrow		Photoproduction $Q^2 \approx 0$ 	DIS $Q^2 \geq 1 \text{ GeV}^2$ 
	c ● 1.5 GeV	5.1	5.2
	b ● 4.75 GeV	5.4	5.5

Figure 30: Ordering of the first parts of the results section devoted to comparisons of data to perturbative QCD calculations.

After this follows in 5.7 a discussion of charm and beauty production results at other colliders in the world, in $\gamma\gamma$ processes at LEP and in $p\bar{p}$ collisions at the TEVATRON. In 5.8 the contributions of charm and beauty production to the ep inclusive scattering at HERA, as expressed by the structure functions $F_2^{c\bar{c}}$ and $F_2^{b\bar{b}}$, are detailed. Finally the non perturbative fragmentation aspects are dealt with in 5.9.

5.1 Charm photoproduction

For the H1 and ZEUS photoproduction analyses presented in this essay the important event kinematic observable y , which in photoproduction represents the fraction of the electron energy entering the hard interaction, is reconstructed from the hadronic final state in the main detector. In this section, first the inclusive D^{*+} measurements are discussed, obtained with the golden decay channel $D^{*+} \rightarrow K\pi\pi_s$. Then the more exclusive analyses are reviewed, where in addition to the D^{*+} one or two jets are selected, which allows more detailed investigations of the production processes. An overview of the presented measurements is given in table 4. In the lower half the perturbative NLO calculations are detailed, which the data are compared to.

5.1.1 D^{*+} inclusive measurements

First measurements at HERA: In the the first H1 and ZEUS measurements [65, 66] on open charm production the inclusive D^{*+} results were extrapolated to obtain total charm photoproduction cross-sections. The results are shown in figure 31 as a function of the photon proton centre-of-mass-energy $W_{\gamma p}$. Measurements from fixed target experiments from the pre-HERA era are also shown. An example is the analysis from EMC [67], which used a beam of muons with energies of 92-280 GeV on a proton target. At HERA, $W_{\gamma p}$ and the observed cross-sections are roughly one order of magnitude larger. The steep cross section rise reflects that with increasing $W_{\gamma p}$ gluons with smaller and smaller proton momentum fractions are accessible for the visible charm production via the photon gluon fusion process. The data in figure 31 are compared with a massive scheme NLO prediction [21], which, as a remarkable fact, is able to describe both the fixed target data at lower $W_{\gamma p}$ and the HERA data at higher $W_{\gamma p}$. This shows that the basic charm production mechanism in photoproduction is at least reasonably well understood and also demonstrates a good understanding of the proton gluon density.

D^{*+} Single differential cross sections: Figure 32 shows the results for the ZEUS D^{*+} analysis [68] as a function of the D^{*+} transverse momentum and pseudorapidity. One should note that the data sample from this analysis is the one with the highest statistical significance of all heavy flavour measurements at HERA, as can be seen in the third row of table 4. The data span a huge kinematic range from $p_t(D^{*+}) = 2 \text{ GeV} \sim m_c$ to $p_t = 20 \text{ GeV} \gg m_c$. Over this range the data fall off by about four orders of magnitude. The measurements are compared to three NLO predictions, the massive scheme (NLO) calculations from Frixione *et al.* [21], the massless scheme (NLL) predictions from Kniehl *et al.* [26], and the mixed scheme (FONLL) calculations from Cacciari *et al.* [30]. In a very rough picture, all three predictions are able to describe the drop off over the complete $p_T(D^{*+})$ range within a factor of two. However, looking more in detail, one observes:

No.	Analysis	c-Tag	Ref.	Exp.	Data	\mathcal{L} [pb^{-1}]	Q^2 [GeV^2]	y	Particle	p_T [GeV]	η	Events	effect. s:b	bgfree events
1	D^{*+} incl.	$K\pi\pi_s$	[65]	H1	94	2.8	< 0.01	[0.28, 0.65]	D^{*+}	> 2.5	[-1.5, 1.0]	119 ± 16	1 : 1.2	50
1		$K\pi\pi_s$	[65]	H1	94	1.3	< 4	[0.10, 0.80]	D^{*+}	> 2.5	[-1.5, 1.0]	97 ± 15	1 : 1.3	40
2		$K\pi\pi_s$	[68]	ZEUS	98/00	78	< 1	[0.17, 0.77]	D^{*+}	[1.9, 20]	[-1.6, 1.6]	10350 ± 190	1 : 2.6	2900
3		$K\pi\pi_s$	[69]	H1	99/00	49	< 0.01	[0.29, 0.64]	D^{*+}	> 2.5	[-1.5, 1.5]	1117 ± 76	1 : 4	220
4	dijets	incl. lt	[55]	H1	99/00	58	< 1	[0.15, 0.80]	Track Jet1(2)	> 0.5 > 11(8)	[-1.3, 1.3] [-0.9, 1.3]	4600 ± 460	1 : 46	100
5	D^{*+} + jet	$K\pi\pi_s$	[71]	H1	99/00	51	< 0.01	[0.29, 0.64]	D^{*+} Jet	> 2.0 > 3	[-1.5, 1.5] [-1.5, 1.5]	588 ± 46	1 : 2	150
6	D^{*+} + dijets	$K\pi\pi_s$	[70]	ZEUS	96/97	37	< 1	[0.19, 0.87]	D^{*+} Jet1(2)	> 3.0 > 7(6)	[-1.5, 1.5] [-2.4, 2.4]	587 ± 41	1 : 1.6	200
7	D^{*+} + dijets	$K\pi\pi_s$	[73]	ZEUS	96-00	120	< 1	[0.17, 0.77]	D^{*+} Jet1(2)	> 3.0 > 7(6)	[-1.5, 1.5] [-1.9, 1.9]	1092 ± 43	1 : 0.7	650
8	D^{*+} + jet	$K\pi\pi_s$	[72]	ZEUS	98-00	79	< 1	[0.17, 0.77]	D^{*+} Jet	> 3.0 > 6	[-1.5, 1.5] [-1.5, 2.4]	4891 ± 113	1 : 1.4	1900

Default settings														Variations			
No.	Program	Ref.	p PDF	γ PDF	μ_r	μ_f	m_c	ϵ_c	p PDF	γ PDF	μ_r	μ_f	m_c	ϵ_c	Treatment		
1	FMNR	[21]	MRSG	GRV-G-HO	m_c	m_c	1.5	0.06	MRSA	LAC1	[0.5, 2]		[1.2, 1.8]		separate var.		
2,7,8	FMNR	[21]	CTEQ5M1	AFG	m_T	m_T	1.5	0.035			[0.5, 2]		[1.3, 1.7]		simult. var.		
2	FONLL	[30]	CTEQ5M1	AFG	m_T	m_T	1.5	0.02			[0.5, 2]		[1.2, 1.8]		linear add.		
3	FMNR	[21]	CTEQ5D	GRV-G-HO	m_T	$2m_T$	1.5	0.035			[0.5, 2]				simult. var.		
4	FMNR	[21]	CTEQ5D	GRV-G-HO	m_T	$2m_T$	1.5	-	MRSG		[0.5, 2]	[0.5, 2]	[1.3, 1.7]		simult. var.		
5	FMNR	[21]	CTEQ5M1	GRV-G-HO	m_T	$2m_T$	1.5	0.035			[0.5, 2]	[0.5, 2]	[1.3, 1.7]	[0.028, 0.042]	simult. var.		
6	FMNR	[21]	MRSG	GRV-G-HO	m_T	$2m_T$	1.5	0.02			[0.5, 1]		[1.2, 1.5]	[0.02, 0.06]	simult. var.		

Table 4: Charm photoproduction measurements discussed in this review. Information is given for each analysis on the charm tagging method, the experiment, the data period, integrated luminosity, Q^2 and y ranges and the cuts on transverse momenta and pseudorapidities of selected final state particles. The last three columns provide information on the number of tagged charm events, the effective signal to background ratio and the equivalent number of background free events. **In the lower half the perturbative NLO calculations** are detailed, with which the data are compared in the respective analysis and which are also shown in the figures. Information is given on: the used program, proton and photon parton density functions, renormalisation and factorisation scales μ_r and μ_f , c -quark mass (in units of GeV) and the ϵ parameter in the Peterson fragmentation function. Information and references for the PDFs can be found in [64]. m_T is defined as $m_T = \sqrt{m_c^2 + p_t^2}$, where p_t is the transverse momentum of the c -quark. On the right the variations of the settings are listed, which are used to estimate the uncertainties of the calculations, shown as error bands in the plots.

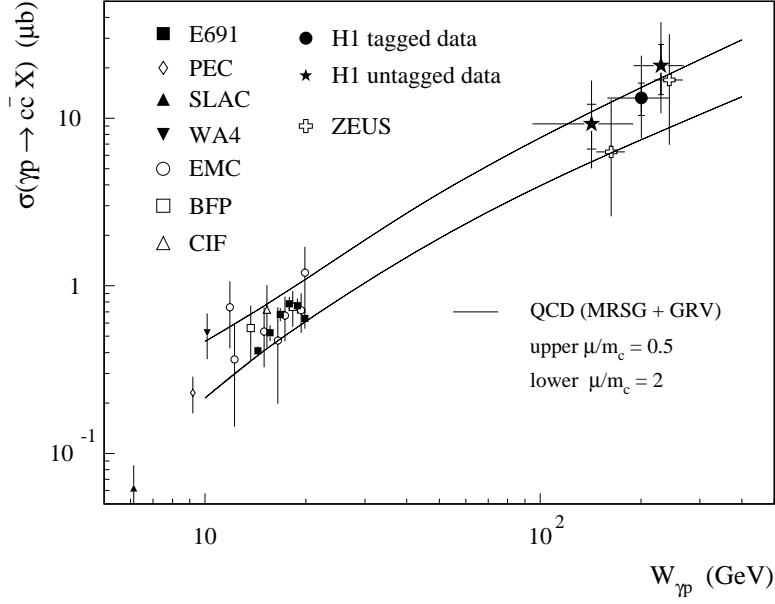


Figure 31: Total charm photoproduction cross section as a function of centre-of-mass energy $W_{\gamma p}$. The data shown are from the first H1 and ZEUS publications on open charm production and from previous fixed target experiments.

1. The NLO prediction is too low for $p_T \sim m_c$, exactly where it is expected to work, while it fits the data better at $p_T \gg m_c$.
2. On the contrary the NLL prediction fits the data better for low p_T , while it is too low for high p_T , where it is expected to work. Only about 30% of the NLL prediction is made up by direct photon interactions, which contributions are shown separately in figure 32, the majority is from resolved photon interactions.
3. The FONLL prediction follows at low p_T the NLO and at high p_T the NLL prediction, as expected for a mixed scheme calculation, and does not provide a better description of the data.

Note that for most of the covered momentum range the errors of the data are much smaller than the prediction uncertainties, which by far largest contribution arises from the variation of the renormalisation scale. Especially for low transverse momenta $p_T(D^{*+}) < 3$ GeV these uncertainties reach a factor of two. This indicates that in this kinematic region the hard scales provided by the charm mass and the transverse momentum of the charm quarks are simply not large enough to ensure a sufficient convergence of the QCD perturbation series at next to leading order.

The plots on the right in figure 32 present the cross sections as function of the pseudorapidity of the D^{*+} . An enhancement is observed in the region $\eta(D^{*+}) > 0$, where the D^{*+} is closer to the proton than to the photon direction. This is due to

ZEUS

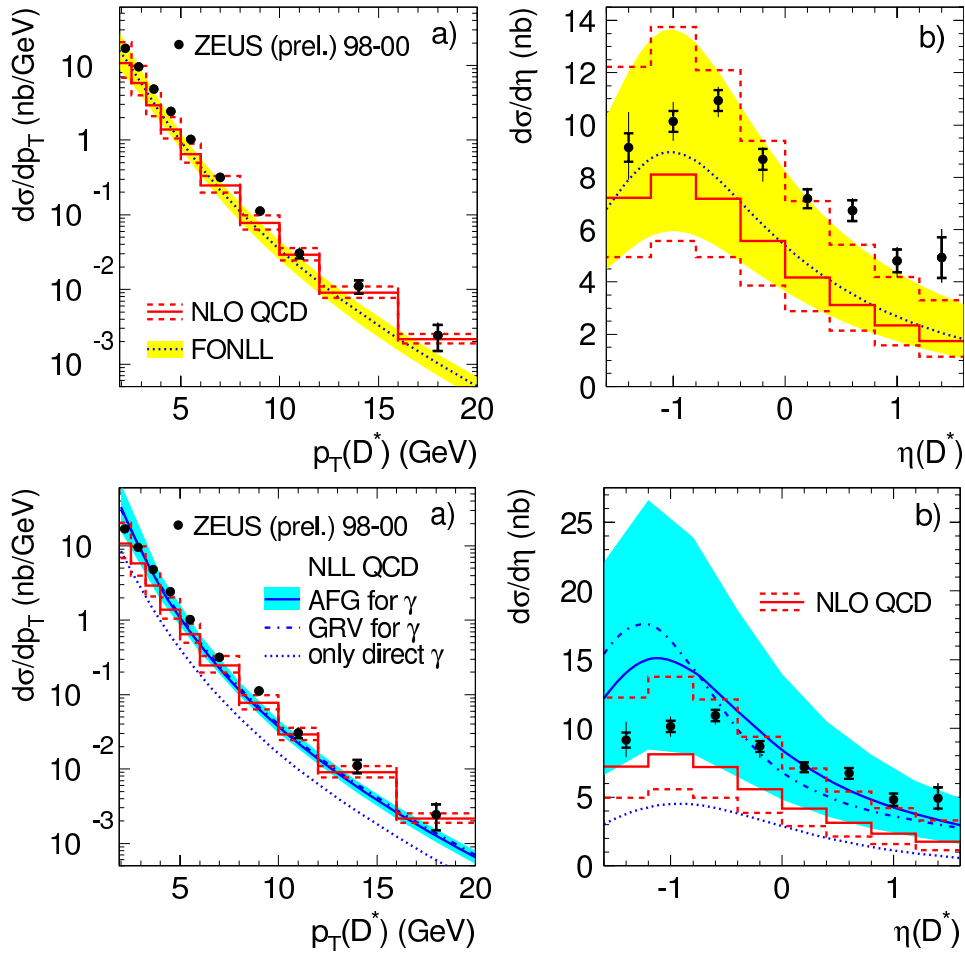


Figure 32: D^{*+} single differential cross sections in photoproduction as function of the D^{*+} transverse momentum and pseudorapidity, from the ZEUS analysis [68]. The measurements are compared to three NLO predictions, the massive scheme (NLO) calculations from Frixione et al. [21], the massless scheme (NLL) predictions from Kniehl et al. [26] and the mixed scheme (FONLL) calculations from Cacciari et al. [30].

the fact that in the probed kinematic region, the photon carries on average larger energy into the photon gluon fusion process than the gluon. The NLO, NLL and FONLL calculations predict all rather similar pseudorapidity shapes. In comparison to the calculations the data are shifted somewhat to the more forward pseudorapidity region. A more or less significant excess is seen for $\eta(D^{*+}) > 0.5$. This resembles the excesses seen in the more forward direction for many other HERA measurements with hard final states such as jets. As discussed in the later sections, such an effect is seen basically for all heavy flavour measurements in photoproduction and in DIS, for charm as well as for beauty. The sensitivity of the predictions to the photon PDF is tested by using in the NLL calculation instead of AFG the GRV photon structure function². As shown

²References for the proton and photon structure functions can be found in [64].

in figure 32 the D^{*+} pseudorapidity distribution is shifted more backwards with GRV. This sensitivity is quite interesting, because it indicates that these data might help to constrain the photon pdf. However, given the overall large uncertainties, it is not clear if the calculations are predictive enough for that purpose. It is an interesting question, which is yet to be answered, if one could improve the situation by using only shape normalised comparisons of data and predictions, i.e. removing the large *global* normalisation uncertainties especially of the calculations. An alternative possibility would be to restrict the measurements and comparisons to larger momentum regions, where the calculations are more predictive, but the data statistics are much smaller. In general the D^{*+} pseudorapidity cross sections alone do not allow to disentangle the effects of the uncertainty of the gluon density and of the photon parton density, since both affect the D^{*+} pseudorapidity distributions.

A similar inclusive D^{*+} photoproduction measurement as the above one by ZEUS is available from H1 [69], performed in a more restricted $W_{\gamma p}$ region (see table 4) with a roughly ten times smaller data sample. The conclusions are very similar. ZEUS has performed in [68] and also in the previous charm milestone paper [70] double differential cross section measurements as function of the D^{*+} transverse momentum and pseudorapidity. The excesses in the more forward pseudorapidity region $\eta > 0.5$ are observed for all regions of transverse momenta.

H1 has recently performed a measurement [55], which extends to the highest charm transverse momenta $p_T^c = 35$ GeV reached so far. Here events are used with two jets in the central rapidity region (detailed cuts are listed in row four of table 4). Due to the high jet transverse momenta the events are efficiently triggered using the deposits of the jet particles in the calorimeter. An inclusive lifetime tagging is applied, based on the displaced impact parameters of jet associated charged tracks from charm and beauty decays. The details of the tagging method are discussed in section 4. Figure 33 shows the measured charm production cross sections as function of the transverse momentum of the leading jet. The data are compared to massive scheme NLO prediction [21], which describe the data well up to the highest jet transverse momenta. For comparing this result with the above D^{*+} measurement (Figure 32) one has to take into account that the jet gives a good approximation of the charm quark kinematics, but the D^{*+} obtains in the fragmentation on average only $\sim 70\%$ of the charm quark momentum. Thus the kinematic range tested with the leading jet from 11 to 35 GeV corresponds roughly to a D^{*+} transverse momentum region from 8 to 25 GeV. It is interesting to note that the experimental errors of both measurements are for comparable momentum regions of similar size. For D^{*+} transverse momenta from 8 GeV up to the highest covered value of 20 GeV the D^{*+} data are similarly well described by the NLO calculation as the dijet data at their correspondingly higher momenta. So the two independent measurements using different tagging techniques give consistent results.

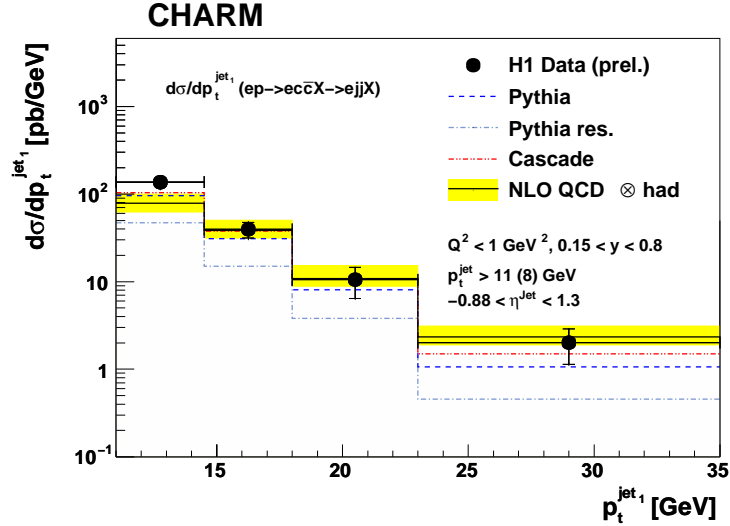


Figure 33: Differential cross sections for the process $ep \rightarrow ec\bar{c}X \rightarrow ejjX$ as function of the transverse momentum p_t^{jet1} of the leading jet, from the H1 analysis [55]. The data are compared to an NLO calculation [21] in the massive scheme.

5.1.2 Studies with a D^{*+} and one other hard parton

To obtain more information on the charm photoproduction process, H1 requires in the analysis [71] in addition to the D^{*+} the presence of a jet in the final state, which is not associated to the D^{*+} . This means that the jet and the D^{*+} are well separated in their directions and that the jet tags another hard parton in the process. This parton can be the other charm quark or a gluon or a light quark. In this analysis very soft jet momentum cuts $p_T > 3$ GeV are applied. The jets are restricted to the central pseudorapidity region $|\eta| < 1.5$, ensuring a good reconstruction with mainly the information of charged tracks. In figure 34 the differential cross sections are shown as function of the pseudorapidities of the D^{*+} and the jet. For the leading order direct photon process it is expected that the D^{*+} tags one charm quark and the jet the other. Since similar momentum cuts are applied for the D^{*+} and the jet, one would expect very similar pseudorapidity distributions for the D^{*+} and the jet. This assumption was verified (not shown) with a Monte Carlo simulation. However, the observed pseudorapidity spectrum for the jet (figure 34) is significantly shifted in the more forward direction compared to that of the D^{*+} . This indicates that the jet often tags another parton, i.e. a gluon or a light quark and that the process is different from the leading order direct photon reaction. This effect is also predicted by the massive and massless scheme NLO calculations the data are compared to in figure 34. The calculations describe the data reasonably well.

ZEUS has performed a similar measurement [72] using events with a D^{*+} and a jet. The main differences are:

- Events are also selected where the D^{*+} is associated to the jet. In this case one

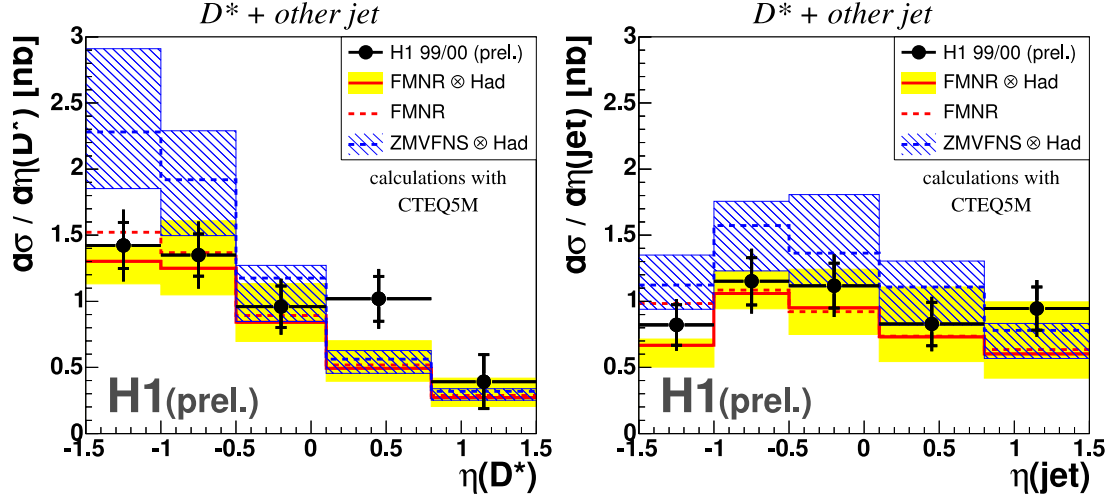


Figure 34: $D^{*+} + \text{jet}$ cross sections as function of the pseudorapidities of the D^{*+} (left) and the jet (right), from the H1 analysis [71]. The measurements are compared to two NLO predictions, the massive scheme (NLO) calculations from Frixione et al. [21] and the massless scheme (ZMVFNS) predictions from Kniehl et al. [26].

does obtain information only about one hard parton in the event, which is a charm quark.

- The jet transverse momentum cut $p_T^{\text{jet}} > 6 \text{ GeV}$ is much harder.
- For the jet a much wider pseudorapidity range $-1.5 < \eta^{\text{jet}} < 2.4$ is covered.

An important observation for this measurement is that the excess observed in the inclusive D^{*+} measurement in the more forward D^{*+} pseudorapidity region (figure 32), is not seen here as a function of the jet pseudorapidity (not shown). A simple explanation for this could be that the jet requirement ensures the presence of a further hard kinematic scale in the event, thus facilitating the convergence of the perturbative QCD expansion. In other words the excesses seen in the inclusive D^{*+} measurement are probably related to charm production processes, where such hard partons are not being produced.

5.1.3 Parton parton studies in charm tagged events

The analyses using tagged charm events with *two identified hard partons* in the final states [55, 70–73], and studying the correlations of the two partons, provide the most detailed information on the production mechanism so far. There are two different experimental approaches followed:

- For the charm tagging the D^{*+} tag is used in the analyses [70–73]. For the two hard partons either the reconstructed D^{*+} plus an additional non associated jet are used, as in [71, 72], or alternatively two jets, as in [70, 72, 73].

- The inclusive lifetime tagging method is used in [55], where dijet events are selected and one jet is tagged as charm using the displaced impact parameters of jet associated charged tracks.

With the two identified parton three observables are constructed, which will be discussed in the following:

1. The observable x_γ^{obs} , which allows to separate, in the leading order picture, direct and resolved photon interactions.
2. The hard scattering angle $\cos\theta^*$ of the two partons, which allows to separate contributions with quark or gluon propagators in the hard scattering.
3. The azimuthal correlation $\Delta\Phi$ of the two partons, which is sensitive to higher order effects.

x_γ^{obs} studies: For the following the case of two jets is assumed for the two hard partons. The observable x_γ^{obs} is defined, which is in the leading order pQCD picture an estimator of the fraction of the photon energy entering the hard interaction:

$$x_\gamma^{obs} = \frac{\sum_{Jet_1}(E - p_z) + \sum_{Jet_2}(E - p_z)}{\sum_h(E - p_z)} \quad (12)$$

The sums in the numerator runs over the particles associated with the two jets and those in the denominator over all detected hadronic final state particles. E and p_z denote the particles energies and momenta parallel to the proton beam, respectively. For the direct process (figure 13a) x_γ^{obs} approaches unity, as the hadronic final state consists of only the two hard jets and the proton remnant in the forward region, which contributes little to $\sum_h(E - p_z)$. In resolved processes x_γ^{obs} can be small. It is also smaller than unity for next to leading order processes with another hard outgoing parton (figure 4) that produces a third jet. Thus in general the observable x_γ^{obs} is sensitive to the resolved photon structure and higher order processes.

One of the milestone papers on charm photoproduction at HERA is the ZEUS analysis [70], where x_γ^{obs} studies are performed using events with a D^{*+} and two jets. The jets are required to have transverse momenta $p_T^{Jet1(2)} > 7(6)$ GeV and are selected in a wide rapidity range $|\eta^{jet}| < 2.4$. In most events the D^{*+} is associated to one of the two jets. Figure 35 shows the measured single differential cross sections as function of x_γ^{obs} . One sees in the data distribution a peak at large $x_\gamma^{obs} > 0.75$, which reflects the direct photon component. Roughly 50% of the data are observed at $x_\gamma^{obs} < 0.75$, indicating large contributions from resolved photon or other higher order contributions. In the lower plot in figure 35 the data are compared to predictions from a massive scheme NLO calculation [21]. The calculation severely underestimates the data cross sections at $x_\gamma^{obs} < 0.75$. This failure clearly indicates the need for higher order corrections beyond NLO. A much better shape description is obtained with the leading order

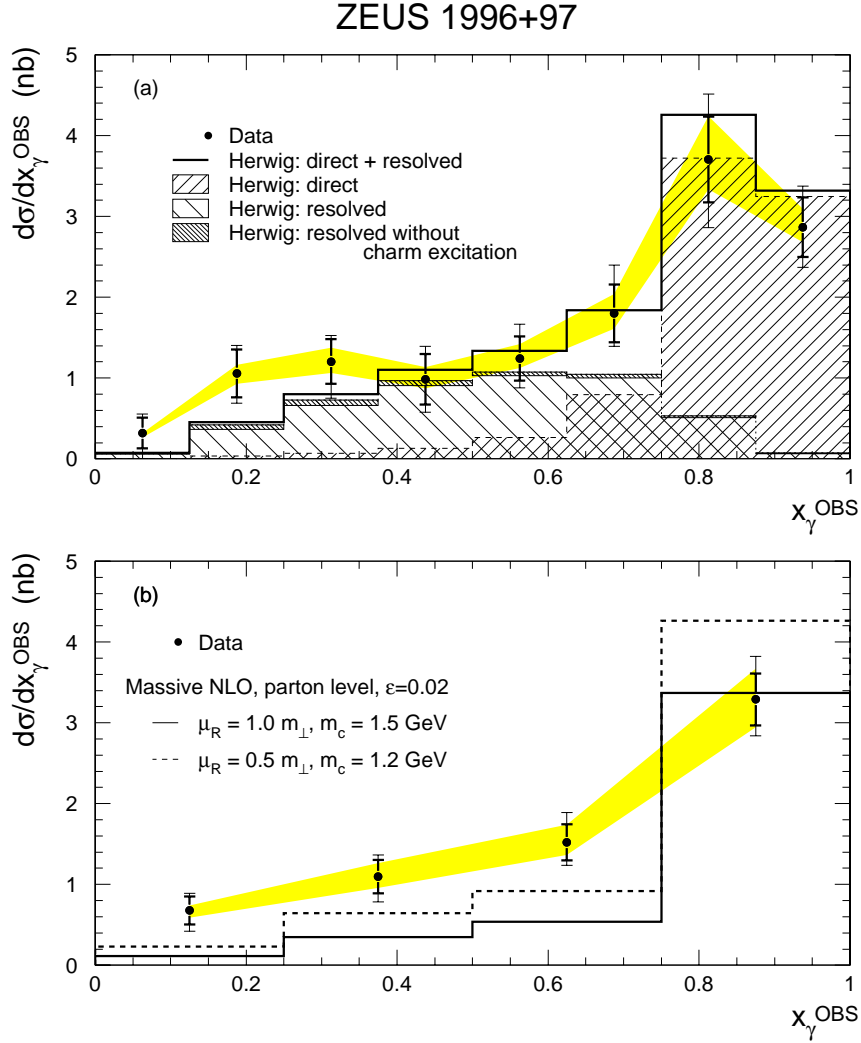


Figure 35: Differential cross section as function of x_{γ}^{obs} for dijets events with an associated D^{*+} meson, from the ZEUS analysis [70]. The data are compared in the lower plot to an NLO calculation [21] in the massive scheme. In the upper plot the data are compared to predictions from the leading order program HERWIG [33] with direct and resolved photon contributions, including a charm excitation component.

HERWIG [33] Monte Carlo program as shown in the upper plot of figure 35. In this calculation a charm excitation component is included, where the charm quark is treated as a massless constituent of the resolved photon, as shown in figure 13c and 13d. This gives for $x_{\gamma}^{obs} < 0.75$ the dominant contributions and provides a reasonable data description. This approach provides at least an effective way of describing the small x_{γ}^{obs} region, although the charm quark is treated as massless in a kinematic region where this is probably not a good approximation. Note that the total cross section with D^{*+} + dijets is only $\sim 18\%$ of the D^{*+} cross section without the dijets, also measured in [70], for the same D^{*+} cuts applied ($p_T(D^{*+}) > 3 \text{ GeV}$ and $|\eta(D^{*+})| < 1.5$). Thus the excesses observed in the D^{*+} + dijet sample in the region $x_{\gamma}^{obs} < 0.75$ contribute only a relatively small part to the inclusive D^{*+} cross section.

In the recent ZEUS analysis [72] using events with a D^{*+} and at least one jet, the first comparison ever is provided of measured x_γ^{obs} cross sections with a massless scheme NLO calculation [26]. Here the D^{*+} and a jet, to which the D^{*+} is not associated, are taken as estimators for the two leading partons and used for the x_γ^{obs} reconstruction in Eq. (12). Note that the available massless scheme calculations provide only cross sections for a $D^{*+} + \text{jet}$ final state but not for two jets. The jet is required in the analysis to have transverse momentum $p_T > 6$ GeV in a pseudorapidity range $-1.5 < \eta < 2.4$. Figure 36 shows the differential cross sections as function of x_γ^{obs} . In the left (right) plot the data are compared to the massive (massless) scheme NLO predictions. Both calculations are too low for the more resolved like region $x_\gamma^{obs} < 0.75$. However, the central massless scheme prediction, using the nominal parameters, is closer to the data than to the central massive scheme calculation. It is unclear, why the uncertainties of the two calculations appear to be so different.

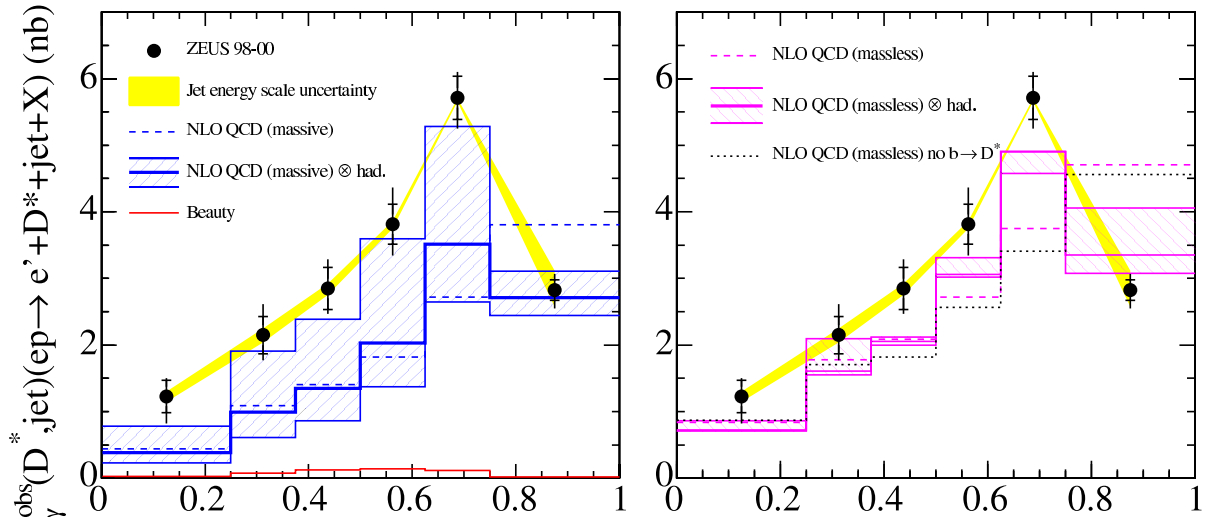


Figure 36: Differential cross sections as function of x_γ^{obs} for events with a jet and a D^{*+} meson, which is not associated to the jet, from the ZEUS analysis [72]. In the left (right) plot the data are compared to a NLO calculation in the massive (massless) scheme, from [21] (from [26]).

Study of hard scattering angle $\cos \theta^*$: ZEUS has investigated in the analysis [73], using events with a D^{*+} and two jets, the scattering angle θ^* of the charm quark with respect to the proton direction in the dijet rest space. The charm quark is identified by the jet, which the reconstructed D^{*+} is associated to. The $\cos \theta^*$ distribution mainly reflects the type of the propagator particle exchanged in the $2 \rightarrow 2$ hard interaction:

- For a charm quark propagator $\cos \theta^*$ should follow a $(1 - |\cos(\theta^*)|)^{-1}$ distribution. The direct photon (figure 13a) and the resolved process with a gluon from the photon structure (figure 13b) belong to this class of processes and also one of the charm excitation diagrams (figure 13c).

- For a gluon propagator $\cos \theta^*$ should follow a $(1 - |\cos(\theta^*)|)^{-2}$ distribution, i.e. a much steeper rise for $|\cos \theta^*| \rightarrow 1$. For leading order processes only the charm excitation mechanism provides such a contribution. (figure13d). The main idea in the ZEUS analysis [73] is to look for such an effect directly in the data.

Special cuts are applied in order to ensure a flat acceptance for the $\cos \theta^*$ distribution over a wide range, extending to as large values of $|\cos \theta^*|$ as possible. The invariant mass of the two jets is required to be above 18 GeV. The average pseudorapidity of the two jets, defined as $\frac{\eta^{jet1} + \eta^{jet2}}{2}$ is required to be smaller than 0.7. Figure 37 shows the obtained differential cross sections as function of x_γ^{obs} . Note that this distribution

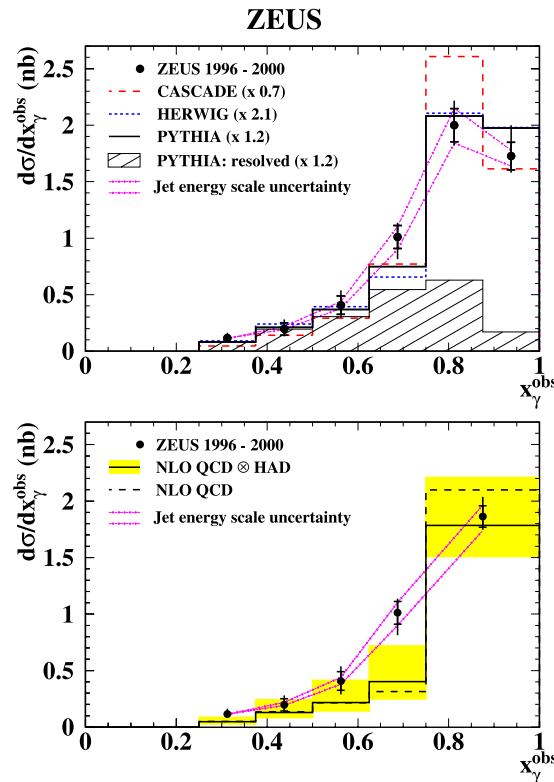


Figure 37: Differential cross section as function of x_γ^{obs} for dijets events with an associated D^{*+} meson, from the ZEUS analysis [73]. The smaller contributions for $x_\gamma^{obs} < 0.75$ compared to the data in figure 35 are due to the additional cuts on the dijet invariant mass $m_{jj} > 18$ GeV and the average pseudorapidity of the two jets $|\bar{\eta}| < 0.7$, which suppress small x_γ^{obs} . The data are compared in the lower plot to an NLO calculation [21] in the massive scheme using the parameters settings and variations listed in table 4. In the upper plot the data are compared to predictions from the LO programs HERWIG [33] and PYTHIA [25] with direct and resolved photon contributions, including a charm excitation component. The prediction by the LO CASCADE [34] program is also shown.

has much smaller contributions for $x_\gamma^{obs} < 0.75$ than the one for the similar analysis [70] shown in figure 35. This is due to the aforementioned special cuts, which basically

restrict the two jets to the pseudorapidity region $\eta^{jet} < 1.9$, while for the analysis [70] the jets extend to $\eta^{jet} < 2.4$. Thus only a small part of the phase space of the “excess events” in figure 35 for $x_\gamma^{obs} < 0.75$ is probed here. The data are compared in figure 37 in the bottom plot to an NLO calculation [21] in the massive scheme, which is again somewhat low for $x_\gamma^{obs} < 0.75$. In the upper plot of figure 37 the data are compared to predictions by the leading order programs PYTHIA [25], HERWIG [33] and CASCADE [34]. Both PYTHIA and HERWIG include charm excitation processes in resolved photon events, which give the dominant contributions for $x_\gamma^{obs} < 0.75$ and provide a reasonable description of the observed x_γ^{obs} shape. In figure 38 the differential cross sections are shown as function of $\cos\theta^*$ separately for $x_\gamma^{obs} < 0.75$ and $x_\gamma^{obs} > 0.75$. In the lower half of figure 38 the data are compared to massive scheme NLO predictions [21]. For the $x_\gamma^{obs} > 0.75$ sample the NLO calculation provides a reasonable description of the data over the whole range of $\cos\theta^*$. One can interpret this as evidence for a dominance of the leading order direct photon process, where the propagator particle is a charm quark and this component is adequately modelled by the NLO calculation. Compared to the $x_\gamma^{obs} > 0.75$ data, there is a much stronger rise visible in the $x_\gamma^{obs} < 0.75$ sample towards more negative $\cos\theta^*$ values. The NLO calculation is not able to follow this. This can be interpreted as a direct proof for sizable contributions from gluon propagator exchanges such as for the charm excitation process (figure 13d), which are not included in the NLO calculation. Indeed the plots in the upper half of figure 38 show that the PYTHIA and HERWIG programs with their large excitation contributions are able to describe the observed rise. For the NLO calculation this means that higher order contributions beyond NLO would be needed to improve the description. In [73] it is claimed as the final conclusion that the above observations ‘demonstrate that charm originating from the photon is the dominant component in the resolved photoproduction of dijet events with charm’. However, as already stated above, the special experimental cuts applied for this analysis have suppressed a large fraction of the ‘excess events’ in the resolved photon region $x_\gamma^{obs} < 0.75$, that are visible in the similar analysis in figure 35. Thus it remains the question, if this much larger excess can be explained alone by the charm excitation mechanism or if there are also other higher order processes involved. In this context a very recent H1 analysis [74] is interesting, which studies charm photoproduction using a muon tagged charm jet and investigating the jet shape of a second untagged jet. In this analysis there are indications that the untagged jet is more charm quark like, also for $x_\gamma^{obs} < 0.75$, compared to the expectation from the excitation models, where it is dominantly a gluon.

Azimuthal correlations: In the ZEUS analysis [72] using events with a D^{*+} and two jets and in the H1 measurement [71] with a D^{*+} and a non associated jet the azimuthal correlation of the two hard partons is investigated. In the leading order picture the two charm quarks are produced in direct photon interactions (figure 13a) back to back in their azimuthal angles in the lab frame, i.e. with $\Delta\phi = 180^\circ$. Smaller $\Delta\phi$ can be due to higher order processes such as gluon radiation or due to a non zero transverse momentum of the partons that enter the hard interaction, as illustrated in fig-

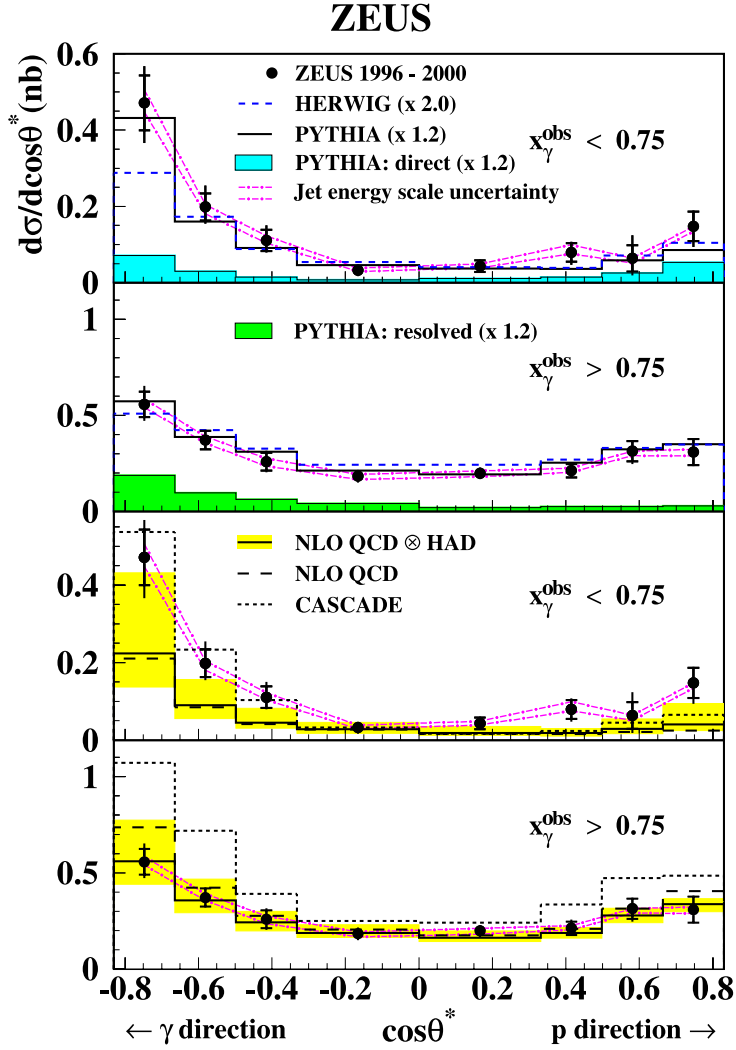


Figure 38: Differential cross sections as function of $\cos \theta^*$ for dijet events with an associated D^{*+} meson, from the ZEUS analysis [73]. Results are given separately for samples enriched in direct ($x_\gamma^{\text{obs}} > 0.75$) and resolved photon events ($x_\gamma^{\text{obs}} < 0.75$). The data are compared in the lower two plots to NLO predictions [21] in the massive scheme using the parameter settings and variations listed in table 4. The predictions of the CASCADE [34] program are also shown. In the upper two plots the data are compared to predictions using the HERWIG [33] and PYTHIA [25] programs, which both include charm excitation processes in the resolved photon component, where in the hard scattering a gluon can be exchanged as propagator particle.

Figure 39. In the ZEUS analysis the transverse momentum requirements for the jets $p_T^{jet1(2)} > 7(6)$ GeV are much harder than the $p_T^{jet} > 3$ GeV for the jet in the H1 analysis. On the contrary in the ZEUS case the two jets are selected in a wider pseudorapidity range $-1.5 < \eta^{jet1,2} < 2.4$ than for H1, where the jet is restricted to $|\eta^{jet}| < 1.5$. Figure 40 shows the differential cross sections as function of the azimuthal difference $\Delta\phi$ between the D^{*+} and the jet for the H1 analysis and between the two jets for the ZEUS measurement. The H1 result is shown in the upper and lower left plots. The

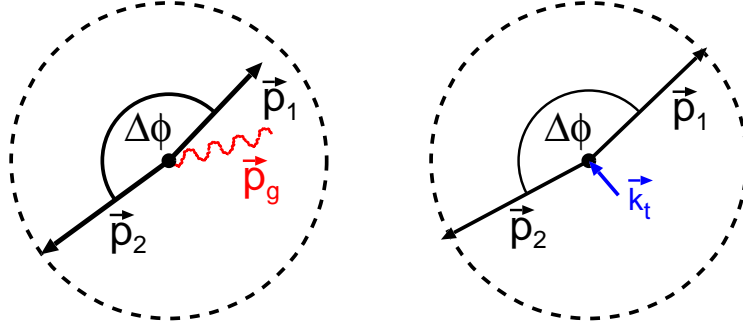


Figure 39: View of the charm quark pair production in the $r\phi$ transverse plane, illustrating how gluon radiation (left) or a transverse momenta of the incoming partons in the hard scattering (right) can lead to a non back-to-back ($\Delta\phi < 180^\circ$) topology of the outgoing hard partons.

data are highest for $\Delta\phi = 180^\circ$, i.e. for the back to back configuration and drop off towards smaller angles. The data are compared in the upper plot in figure 40 with NLO calculations in the massive scheme, from [21] and in the massless scheme, from [26]. Both calculations drop off more steeply compared to the data towards smaller opening angles than 180° . Especially for $\Delta\phi \approx 100^\circ$ there is a problem, since the two calculations predict almost zero contributions, while there are still sizeable ones in the data. A better description is obtained with the LO programs PYTHIA [25] and CASCADE [34], which are shown in the lower plot. PYTHIA includes charm excitation processes in resolved photon events, which give the dominant contributions for $\Delta\phi < 140^\circ$ and provide a reasonable data description in this region. The results of the ZEUS analysis [72] are shown in the middle and right plots of figure 40. Here the azimuthal correlation is measured separately in the more direct photon region $x_\gamma^{obs} > 0.75$ and in the more resolved photon region $x_\gamma^{obs} < 0.75$. The data are compared in the upper plots to an NLO calculation [21] in the massive scheme. For the more direct photon sample the description is satisfactory. On contrary for the more resolved photon sample, the NLO calculation is clearly falling below the data for $\Delta\phi < 120^\circ$. Again a better shape description is obtained by PYTHIA and HERWIG, which are compared in the lower plots to the data. Thus the conclusion is again very similar to the above studies with the x_γ^{obs} observable: The NLO calculation is missing a component in the data, which can be effectively described by a LO charm excitation component in resolved photon processes. It is interesting to note that the NLO problems in the $\Delta\phi$ distribution are seen both for the lower charm quark transverse momenta probed with the soft jet cuts in the H1 analysis and for the higher momenta probed in the ZEUS analysis, which on the other hand covers a larger rapidity range.

Thus we have seen in this section a partial failure of the massive scheme NLO predictions for the three independent parton parton kinematic observables x_γ^{obs} , $\cos\theta^*$ and $\Delta\phi$, which were studied in charm events with a D^{*+} and one or two jets. The NLO calculations in the massless scheme, where available, do mostly not provide a significant better description for the observables. However, it must be also stated that the

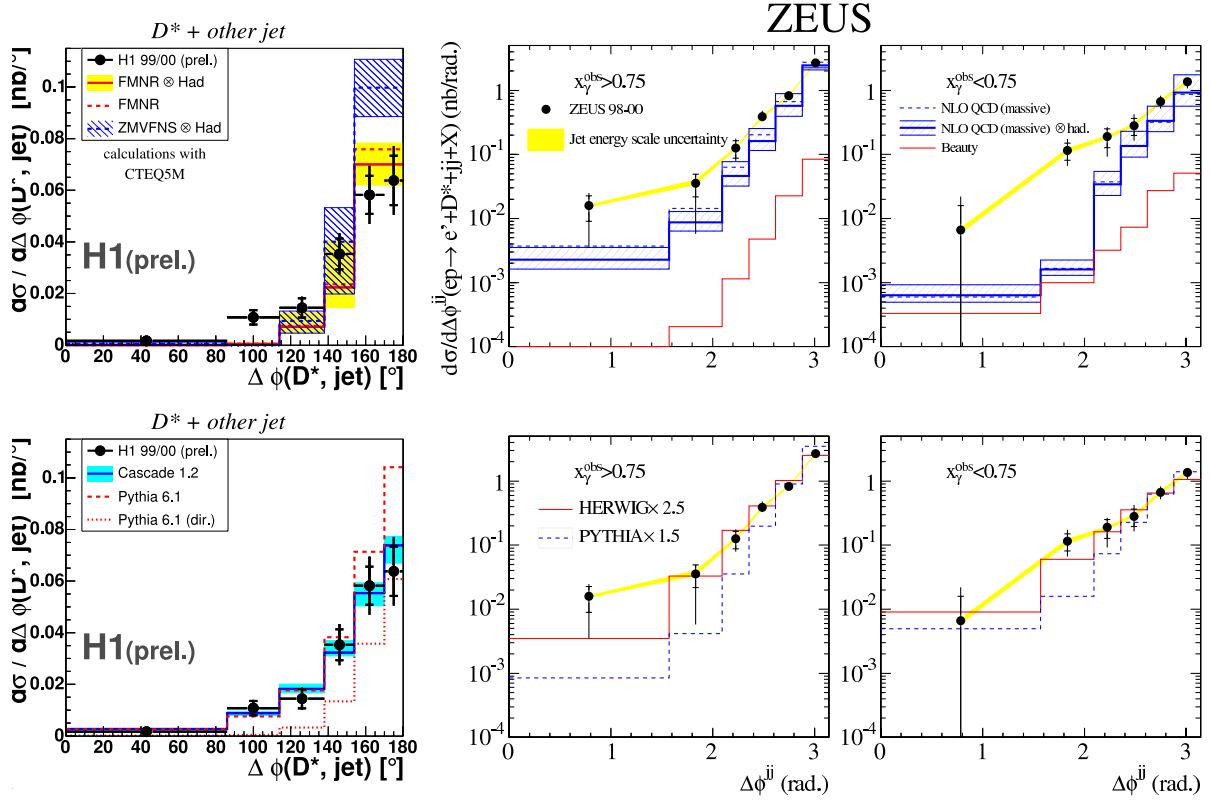


Figure 40: Azimuthal differences of two outgoing hard partons in D^{*+} tagged charm events. The upper and lower left plots show the results from the H1 analysis [71], the upper and lower middle and right plots the one from the ZEUS analysis [72]. In the H1 analysis the azimuthal difference of the selected D^{*+} and a jet is shown. The D^{*+} is required to be not associated to the jet. In the ZEUS analysis the azimuthal difference of the two selected jets is shown. In the upper plots the data are compared to NLO predictions [21] in the massive scheme. The H1 data are also compared to an NLO calculation [26] in the massless scheme (labeled as ZMVFNS). The detailed parameter settings and variations of the calculations are listed in table 4. In the lower plots the data are compared to predictions from the LO programs PYTHIA [25], CASCADE [34] and HERWIG [33].

deviations of data and the NLO calculations are mostly concentrated in some corners of the kinematic phase space, which often do not contribute much to the total charm production cross sections. This is also true for the $\Delta\phi$ observable, as can be seen in the upper left plot of figure 40. The excess in the bin $\Delta\phi \approx 100^\circ$ contributes only about 5% to the cross section integrated over $\Delta\phi$.

5.2 Charm production in DIS

The previous section discussed charm production in ep collisions with the exchange of *real photons*. Now the photon virtuality is raised to values $Q^2 > 1 \text{ GeV}^2$ and the regime of deep inelastic scattering (DIS) is entered. For most DIS analyses presented in this essay the event kinematic variables Q^2 and y are reconstructed from the scattered electron as measured in one of the calorimeters. An overview of the presented measurements and theory calculations is given in the table 5. The results are all based on the full reconstruction of D-mesons, in most cases using the D^{*+} golden decay channel. Results based on inclusive lifetime tagging [54,75] will be presented in section 5.8, where the charm contribution to inclusive deep inelastic ep scattering is discussed.

Production mechanism: In the first measurement [76] of charm production at HERA the production mechanism in DIS is investigated for the kinematic range $10 < Q^2 < 100 \text{ GeV}^2$, where Q^2 is already larger than m_c^2 . The main question is if in this kinematic regime the photon gluon fusion process $\gamma^* g \rightarrow c\bar{c}$ or the quark parton model process $\gamma^* c \rightarrow c$ dominates. Events are used with fully reconstructed D^{*+} and D^0 mesons applying the selection cuts listed in table 5. A sensitive observable to test the production mechanism is

$$z_D = \frac{p_D \cdot p}{q \cdot p},$$

which is in the proton rest frame the fraction of the photon energy transferred to the D -meson. For the QPM process the struck charm quark absorbs the full photon energy, i.e. $z_c = 1$ with

$$z_c = \frac{p_c \cdot p}{q \cdot p}.$$

z_D is expected to be somewhat smaller due to the charm quark fragmentation process, where the D -mesons obtains in average $\sim 70\%$ of the charm quark momentum. On contrary for the PGF process the charm and the anticharm quark share the photon energy, i.e. z_c is expected to be on average 1/2 and z_D is correspondingly smaller. In the analysis [76] the variable

$$x_D = \frac{2|\vec{p}_D|}{W_{\gamma p}}$$

is used instead of z_D , however, both quantities are very closely connected. Figure 41 shows the differential cross sections as a function of x_D for the D^{*+} (closed points) and the D^0 (open points) measurements. The shaded and dashed histograms shows the expectation of the PGF and the QPM processes, respectively, according to Monte Carlo simulations. The PGF model agrees very well with the data, while the QPM model clearly fails. By fitting the normalisations of the two models to the data in figure 41, an upper limit for the fraction of QPM processes $f(QPM)$ is derived:

$$f(QPM) < 0.05 \quad \text{at 95\% c.l.}$$

The paper [76] thus concludes *'that photon gluon fusion is the dominant charm production process in DIS at HERA'*.

No.	Analysis	c-Tag	Ref.	Exp.	Data	\mathcal{L} [pb^{-1}]	Q^2 [GeV^2]	y	Particle	p_T [GeV]	η	Events	effect. s:b	bgfree events
1	D^{*+} incl.	$K\pi\pi_s$	[76]	H1	94	3	[10, 100]	< 0.53	D^{*+}	> 1.5	$[-1.5, 1.5]$	103 ± 13	1 : 0.7	64
1	D^0 incl.	$K\pi$	[76]	H1	94	3	[10, 100]	< 0.53	D^{*+}	> 2.0	$[-1.5, 1.5]$	144 ± 19	1 : 1.5	57
2	D^{*+} incl.	$K\pi\pi_s$	[77]	ZEUS	98-00	82	[1.5, 1000]	[0.02, 0.7]	D^{*+}	[1.5, 15]	$[-1.5, 1.5]$	5545 ± 129	1 : 0.5	3070
3	D^{*+} incl.	$K\pi\pi_s$	[81]	H1	95-96	10	[2, 100]	[0.05, 0.7]	D^{*+}	[1.5, 15]	$[-1.5, 1.5]$	583 ± 35	1 : 1	270
4	D^{*+} incl.	$K\pi\pi_s$	[80]	H1	97	18	[1, 100]	[0.05, 0.7]	D^{*+}	> 1.5	$[-1.5, 1.5]$	973 ± 40	1 : 1.5	600
5	D^{*+} incl.	$K\pi\pi_s$	[82]	ZEUS	98-00	82	[0.05, 0.7]	[0.02, 0.85]	D^{*+}	[1.5, 9]	$[-1.5, 1.5]$	253 ± 25	1 : 1.5	100
6	D^{*+} + dijets	$K\pi\pi_s$	[83]	ZEUS	96-00	104	$< 5 \cdot 10^3$	[0.25, 0.65]	D^{*+} Jets1(2)	> 3 $> 7.5(6.5)$	$[-1.5, 1.5]$ $[-2.4, 2.4]$	2600 ± 70	1 : 0.9	1380
7	charm	incl. lt	[54]	H	99/00	57	[6, 120]	[0.07, 0.7]	Track	> 0.5	$[-1.3, 1.3]$	18000 ± 562	1 : 18	1024
8	charm	incl. lt	[52]	H	99/00	57	> 150	[0.1, 0.7]	Track	> 0.5	$[-1.3, 1.3]$	2000 ± 164	1 : 20	100

No.	Program	Ref.	Default settings						Variations					
			μ_r	μ_f	m_c	ϵ_c	p PDF	μ_r	μ_f	m_c	ϵ_c	Treatment		
2.5	HVQDIS	[22]	ZEUS-NLO [78]	$\sqrt{Q^2 + 4m_c^2}$	μ_r	1.35	0.035	p PDF	[0.5, 2]	[1.2, 1.5]	[0.02, 0.05]	quadr. add.		
3	HVQDIS	[22]	CTEQ4F3	$\sqrt{Q^2 + 4m_c^2}$	μ_r	1.5	0.036	MRS(A)	[2 m_c , 2 Def]	[1.3, 1.7]	[0.026, 0.046]	quadr. add.		
7.8	HVQDIS	[22]	CTEQ5F3	m_T	m_T	1.3								
7.8	MRST	[28]	MRSTQED04	$\sqrt{Q^2}$	μ_f	1.43								
7.8	MRST-NNLO	[29]	unspecified	$\sqrt{Q^2}$	μ_f	1.43								
7.8	CTEQ	[27]	CTEQ6HQ	$\sqrt{m_c^2 + Q^2}$	μ_f	1.3								

Table 5: **Charm DIS measurements** discussed in this review. Information is given for each analysis on the charm tag method, the experiment, the used data period, integrated luminosity, Q^2 and y ranges and the cuts on transverse momenta and pseudorapidities of selected final state particles. The last three columns provide information on the number of tagged charm events, the effective signal to background ratio, as calculated from $s : b = \text{events} : (\sigma(\text{events})^2 - \text{events})$ and the equivalent number of background free events, as calculated from $[\text{events}/\sigma(\text{events})]^2$. In the lower table for each measurement the perturbative NLO calculations are detailed to which the data are compared. Information is given on the used program, the proton parton density function and the default parameters for the renormalisation and factorisation scales μ_r and μ_f , the c -quark mass (in units of GeV) and the ϵ parameter in the Peterson fragmentation function. Information and references for the PDFs can be found in [64]. m_T is defined as $m_T = \sqrt{m_c^2 + p_t^2}$, where p_t is the transverse momentum of the c -quark. On the right the variations of the parameter settings are listed, which are used to estimate the uncertainties of the calculation, shown as error bands in the plots.

D^{*+} Single differential cross sections: Figure 42 shows the D^{*+} single differential cross sections, from the ZEUS analysis [77]. The data sample from this analysis is the one with the highest available statistical significance of HERA charm measurements in DIS, as can be seen in the third row of the last column in table 5. Hence the measurements are quite accurate, i.e. at the $\sim 10\%$ level for the differential cross sections. In the two upper plots in figure 42 the cross sections are shown as a function of the photon virtuality Q^2 and Bjorken x . Both distributions fall by about four orders of magnitude in the covered region, which reflects mainly the $1/Q^4$ cross-section dependence of the photon propagator. In the two lower plots the cross sections are shown as function of the D^{*+} transverse momentum and pseudorapidity. The cross section $d\sigma/dp_T(D^{*+})$ falls by two orders of magnitude with increasing $p_T(D^*)$. The cross section $d\sigma/d\eta(D^{*+})$ rises with increasing $\eta(D^*)$.

The data are compared in figure 42 with the massive scheme NLO calculation, from Harris and Smith [22], using the parameter settings and variations listed in table 5. Unfortunately for the time being there are no NLO calculations in the massless scheme available that could be compared to D^{*+} production in DIS. The NLO prediction provides a reasonable description of all measured cross sections. Note, that a charm quark mass $m_c = 1.35$ GeV is used here for the central value of the NLO calculation.

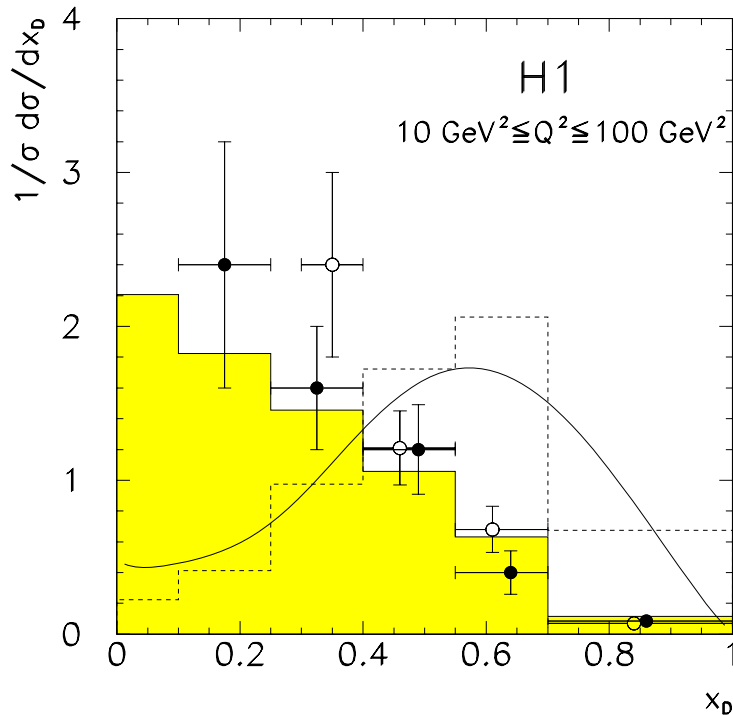


Figure 41: Normalised distribution of the observable $x_D = \frac{2|\vec{p}_D|}{W_{\gamma p}}$, from the first HERA analysis [76] of charm production in deep inelastic scattering, using fully reconstructed D^{*+} and D^0 mesons. x_D is a measure of the photon energy absorbed by the D -meson, in the proton rest frame. The open (closed) points show the D^0 (D^{*+}) data. The shaded and dashed histograms shows the expectation for PGF and the QPM processes, respectively, according to Monte Carlo simulations.

ZEUS

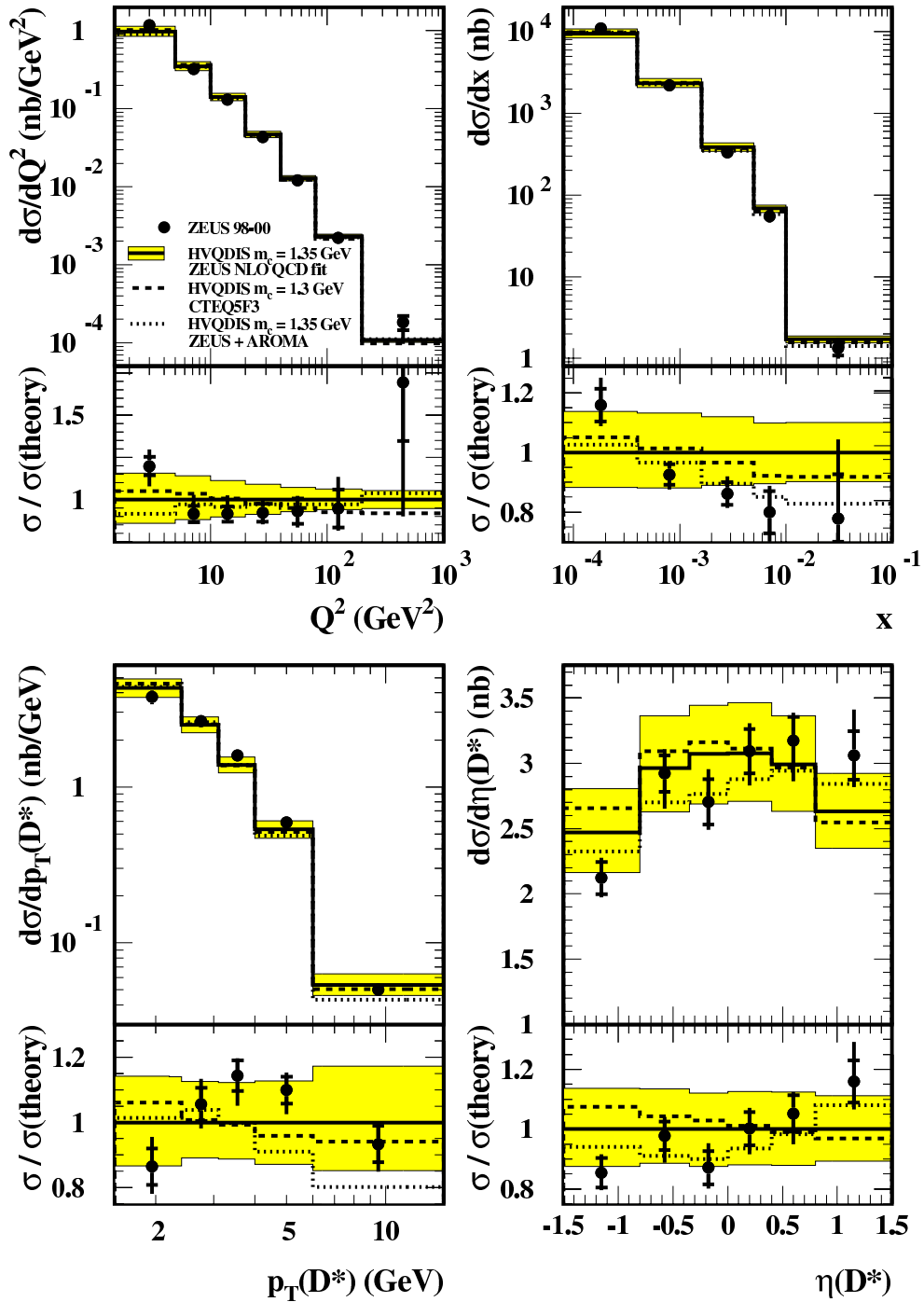


Figure 42: Differential D^{*+} cross sections as a function of photon virtuality Q^2 (upper left plot), Bjorken x (upper right plot), D^{*+} transverse momentum (lower left plot) and the D^{*+} pseudorapidity (lower right plot), from the ZEUS analysis [77]. The data are compared to NLO predictions [22], using the ZEUS NLO PDF (solid line), the CTEQ5F3 PDF (dashed-dotted line) and an alternative hadronisation scheme (dotted line), as discussed in detail in [77]. The ratios of the cross sections to the predictions are also shown beneath each plot.

For many other NLO calculations a higher value $m_c = 1.5$ GeV is used, e.g. for all the comparisons with photoproduction analyses (see table 4). Using a 0.15 GeV lower charm mass leads to a roughly 10% cross section increase in the visible data range and thereby significantly changes the agreement of data and NLO in the overall normalisation. Furthermore note that the estimated uncertainties of the NLO calculation are much smaller here than for the photoproduction case. This can be seen clearly by comparing the widths of the NLO error bands in figure 32 and figure 42 e.g. for the D^{*+} pseudorapidity distributions. The reason for this is that in DIS Q^2 provides an additional hard scale, which is typically harder than m_c^2 and $p_T(c)^2$, the only hard scales in photoproduction. In photoproduction, the renormalisation scale, which is usually set to $\mu_r = \sqrt{m_c^2 + p_T(c)^2}$ and varied within factor two, is small and thus the corresponding α_s variations are big. This uncertainty is heavily suppressed in DIS, where the renormalisation scale is usually set to $\mu_r = \sqrt{4m_c^2 + Q^2}$.

In the ZEUS analysis [77] the sensitivity is studied of the data description to the proton PDF and the charm fragmentation model used for the NLO calculation. For the proton PDF, instead of using the ZEUS NLO PDF [78], the CTEQ5F3 density is alternatively used. The results are shown separately in figure 42 as dashed lines. The differences between the predictions, which are comparable to the uncertainties in the data, demonstrate the sensitivity of this measurement to the gluon distribution in the proton. As can be seen in the ratio of data and theory, which is displayed for each variable, the prediction with using CTEQ5F3 gives a somewhat better description of $d\sigma/dx$ than that obtained with the ZEUS NLO fit. However for the other distributions, especially for $d\sigma/d\eta(D^*)$ the ZEUS NLO PDF, which was fit to recent inclusive DIS data, gives the best description of the data. The standard way to treat heavy quark fragmentation for the NLO calculations is to use the Peterson fragmentation function [23]. This function models the distribution of the momentum component of the D^{*+} parallel to the direction of the mother charm quark. However a transverse momentum component is not treated and hence usually assumed to be zero. In addition no QCD evolution is included. On contrary, the Lund string fragmentation model [31] predicts a migration of the charm quark emerging from the hard interaction towards positive pseudorapidities as it fragments into a D^{*+} due to the interaction between the color charges of the c quark and the proton remnant. This is called the 'beam drag effect'. To quantify this effect, effective Lund string fragmentation corrections are applied to the partons in the NLO calculation using the AROMA MC program [79], which has implemented this fragmentation model. With this indeed a better description of $d\sigma/d\eta(D^{*+})$ is obtained as illustrated with the dotted lines in figure 42, although in this case $d\sigma/dp_T(D^{*+})$ is not so well described.

It should be noted, that in the H1 measurement [80] the conclusions concerning the description of the D^{*+} pseudorapidity spectrum are somewhat different. Here the NLO calculation [22] is observed to undershoot the data for positive D^{*+} pseudorapidities (not shown). However, the experimental errors of the H1 analysis [80] are with $\sim 30\%$ for the differential measurements relatively large and the excesses are not very significant. In the H1 analysis the fragmentation is performed for the NLO calculation using

the Peterson fragmentation function for the longitudinal fragmentation. In addition, to account for the experimentally observed p_t smearing of hadrons with respect to the quark direction, the D^{*+} meson has been given a transverse momentum p_t with respect to the charm quark, according to the function $p_t \cdot \exp(-\alpha p_t)$. The parameter α is chosen such that an average transverse momentum $\langle p_t \rangle \approx 350$ MeV is obtained as observed in e^+e^- data. It was checked, that with this treatment very similar results are obtained for the D^{*+} pseudorapidity distributions of the NLO calculation compared to the method of applying an effective Lund string fragmentation using the AROMA Monte Carlo simulation. The excess observed at H1 for positive D^{*+} pseudorapidities resembles the one seen in photoproduction (figure 32) and in other HERA measurements with hard final states such as jets. However, as already stated above, the significance of the excess is not very large.

D^{*+} transverse momentum spectrum in hadronic centre-of-mass frame: In the γ^*p restframe the two charm quarks are produced in the leading order PGF process with a certain transverse momentum $p_T^*(c)$, which transfers in the fragmentation to the D^{*+} transverse momentum $p_T^*(D^{*+})$. In photoproduction the transverse momentum in the lab frame $p_T(D^{*+})$ is the same as $p_T^*(D^{*+})$. However, in DIS, $p_T(D^{*+})$ receives a contribution from the transverse boost of the γ^*p system reflecting the non zero Q^2 or in other words the transverse recoil of the scattered electron. This can be exploited to measure cross sections for almost zero $p_T^*(D^{*+})$, since $p_T(D^{*+})$ can be still large enough to have a good detector acceptance. The only available HERA measurement of differential cross sections as function of $p_T^*(D^{*+})$ is from the H1 analysis [81]. The results are shown in figure 43. In the figure $p_T^*(D^{*+})$ is denoted as p_\perp^* . Clearly this distribution is different from the $p_T(D^{*+})$ cross sections in figure 42. It is having its maximum approximately at $p_T^*(D^{*+}) = m_c$ and falls towards lower transverse momenta. The massive scheme NLO calculation [22] with the parameters listed in table 5 gives an adequate data description.

Transition from DIS to photoproduction: ZEUS has investigated in [82] charm production in the transition region from photoproduction to DIS. i.e. for $0.05 < Q^2 < 0.7$ GeV², using events with a fully reconstructed D^{*+} . For this measurement the scattered electron is detected in the beam pipe calorimeter (BPC). Figure 44 shows the measured cross sections as a function of Q^2 , covering the new BPC results and also the DIS results for $Q^2 > 1$ GeV², which were already presented in figure 42. The data fall by about five orders of magnitude in the covered region, mainly reflecting the $1/Q^4$ dependence of the photon propagator. The data are compared to the massive scheme NLO calculation [22]. It is a remarkable triumph, that this calculation is able to describe well all the data points from $Q^2 = 0.05$ GeV² $\ll m_c^2$ to $Q^2 = 1000$ GeV² $\gg m_c^2$. It is an interesting question, if there is not a contradiction between the BPC and the photoproduction D^{*+} results that were shown in figure 41. For photoproduction the corresponding massive scheme NLO calculation [21] was about 25% too low in the

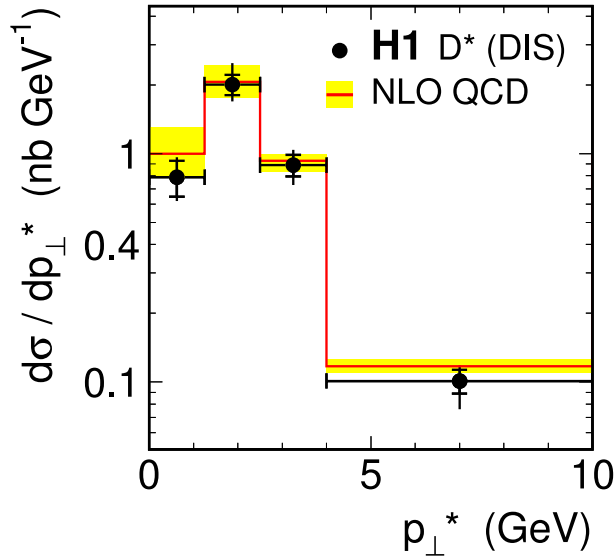


Figure 43: D^{*+} cross sections as function of the D^{*+} transverse momentum p_{\perp}^* in the hadronic centre-of-mass frame, from the H1 analysis [81]. The data are compared to the massive scheme NLO prediction [22], using the parameter settings and variations listed in table 5.

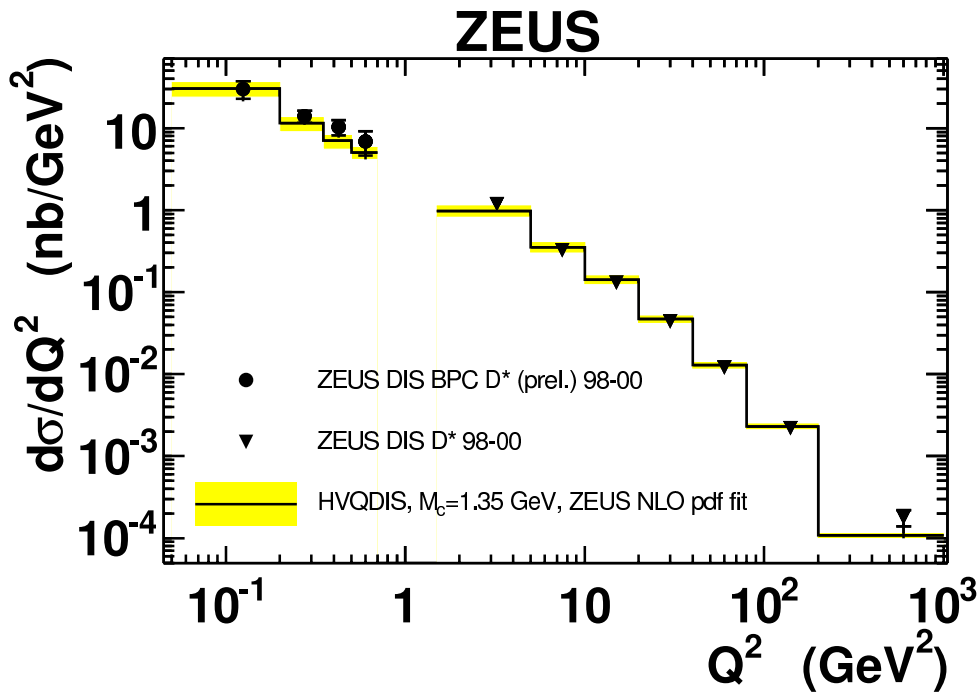


Figure 44: Differential D^{*+} cross sections as a function of Q^2 from the ZEUS analyses [77, 82]. The data are compared to massive scheme NLO predictions [22].

overall normalisation. It is somewhat astonishing that the BPC measurements are in better agreement, although the Q^2 values are so small, that the situation is more or less like in photoproduction. However, one has to take into account that for the comparison

to the BPC and DIS results (figure 44) a lower charm quark mass $m_c = 1.35$ GeV is used in the NLO calculation (see table 5) compared to $m_c = 1.5$ GeV that is used in photoproduction (see table 4). This lower charm quark mass corresponds to a $\sim 10\%$ increase of the calculated cross sections. When considering in addition, that the data in the second to fourth Q^2 bins of the BPC measurements are about 20% above the NLO calculation and the data in the first Q^2 bins has large errors, the picture is still consistent.

Resolved photon structure as function of Q^2 : It is known that resolved photon like events vanish in DIS towards higher Q^2 , since the increasing photon virtuality suppresses hadronic fluctuations of the photon. This is usually also assumed for charm (or beauty) events. For all the above measurements of charm production in DIS, the massive NLO calculations [22] which were compared to the data have only a direct and no resolved photon component. The charm mass itself provides a hard scale and also a kinematic threshold that suppresses the probability for a fluctuation of the photon into a $c\bar{c}$ pair. It is an interesting question how in charm events the two hard scales Q^2 and m_c interplay in the suppression of resolved photon events. This is studied in ZEUS analysis [83] using events with a D^{*+} and two jets. As a sensitive observable the ratio of the cross sections for $x_\gamma^{obs} < 0.75$ and $x_\gamma^{obs} > 0.75$ is studied, where x_γ^{obs} is reconstructed from the two jets using Eq.(12). The larger this ratio the bigger is the resolved photon like component. Figure 45 shows this ratio for five Q^2 bins, one for photoproduction (most left bin) and four for DIS. An almost flat ratio ~ 0.5 is observed as a function of

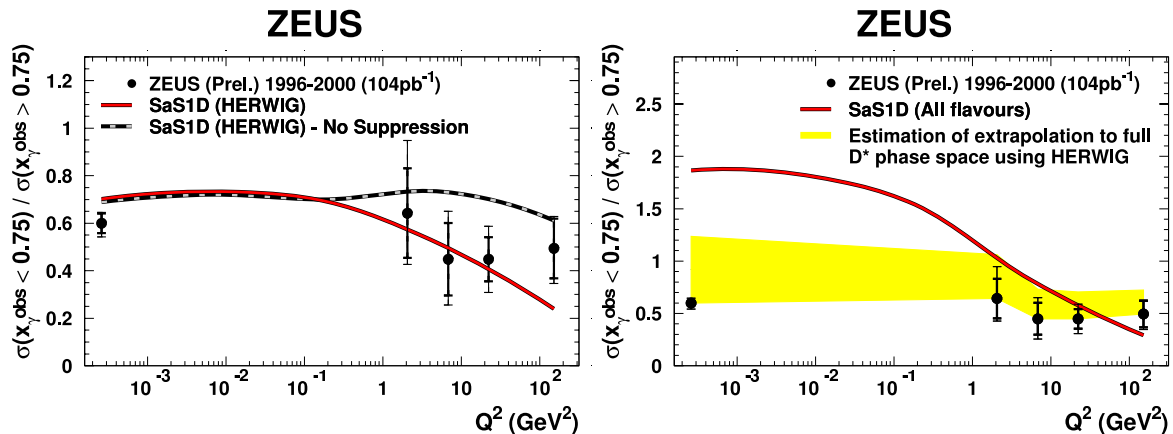


Figure 45: The left plots shows the ratio of low to high x_γ^{obs} for events with a D^{*+} and two jets, from the ZEUS analysis [83]. The data are compared to a LO prediction from HERWIG [33] which includes a resolved photon component using the SaS1D photon structure function. In one case a Q^2 dependent suppression of the resolved component is applied, in the other not. In the right the same data are compared to a curve, marked as SaS1D, which is known to describe the observed shape of a flavour inclusive dijet sample, dominated by light quarks. The data are also shown (shaded band) after extrapolation to the full D^{*+} phase space.

Q^2 . The data are compared in the left plot of figure 45 to the LO HERWIG [33] program with a resolved photon component using the SaS1D [64] virtual photon PDF. For one prediction curve a 'standard' Q^2 dependent suppression of the partonic structure of the photon is applied and for the other it is switched off. Unfortunately the data are not sufficiently accurate to distinguish between these two treatments. In the right plot of figure 45 the same data are compared to a curve, marked as SaS1D, which is known to describe the observed shape of a flavour inclusive dijet sample, dominated by light quarks. Since the D^{*+} kinematic cuts itself suppress the resolved component, an extrapolation of the D^{*+} data to the full D^{*+} phase space is performed using HERWIG. The estimation of the ratio after the extrapolation, shown as the shaded band, lifts the ratio somewhat. However, even with this correction, the ratio falls much slower with increasing Q^2 for the charm data than for the curve which represents the flavour inclusive sample. This demonstrates for the first time ever that the observed suppressions of the low x_γ^{obs} cross section due to non-zero photon virtuality and due to the charm quark mass are not independent. This is a purely experimental observation and thus stands for itself. However, for the interpretation of the low x_γ^{obs} in terms of resolved photon contributions one should note (as stated before) that this is not straightforward, since the resolved photon like events can be mimicked by higher order effects, such as hard gluon radiation that are not related to a resolved photon structure. To shed further light on this, comparisons of the observed ratios with NLO calculations would be helpful.

5.3 Beauty introduction

The total production rates of light, charm and beauty quarks at HERA roughly scale like

$$\sigma_{uds} : \sigma_c : \sigma_b \sim 2000 : 200 : 1.$$

The strong suppression of beauty events is mostly due to the limited kinematic phase space, as illustrated in figure 46. To produce two beauty quarks in the BGF process a minimal proton momentum fraction of the gluon of $\sim 10^{-3}$ is needed, while for charm the threshold is $\sim 10^{-4}$. A further suppression factor of *four* for beauty production relative to charm production is due the smaller electric charge of down type quarks compared to up type quarks. Given this small production rates, the HERA beauty

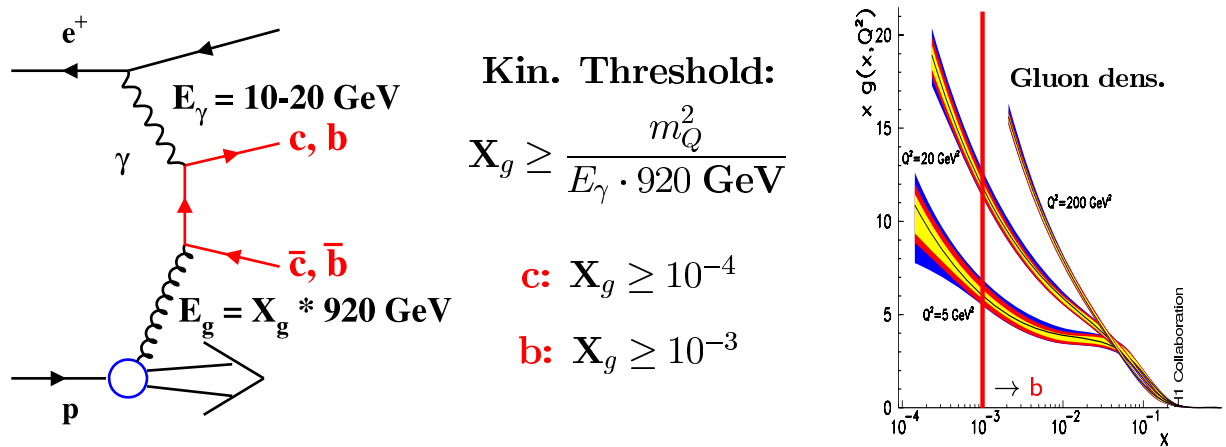


Figure 46: Comparison of kinematical thresholds for charm and beauty production at HERA in terms of the minimum proton momentum fraction x_g of the gluon that enters the hard interaction. The left plot shows the PGF process where the energies are indicated that enter the heavy quark pair production process. The threshold formula for x_g in the middle of the figure is calculated from $(x_g p + q)^2 \approx 2x_g p q = 4x_g E_\gamma E_p \geq (2m_Q)^2$, where p and q are the four vectors of the proton and photon, respectively. The right plot shows the gluon density in the proton as determined from the measured scaling violations of the F_2 structure function. The vertical line indicates the minimum fraction $X_g = 10^{-3}$ for beauty production at HERA.

measurements are restricted to much smaller samples than that available for charm. While for the differential charm measurements precision levels of $\leq 10\%$ are reached, for beauty measurements the typical accuracy is $\geq 20\%$ and for some bins only $\sim 50\%$.

5.4 Beauty in photoproduction

An overview of the presented beauty photoproduction measurements is given in table 6.

No.	Analysis	b Tag	Ref.	Exp.	Data	\mathcal{L} [pb^{-1}]	Q^2 [GeV^2]	y	Particle	p_T [GeV]	η	Events	effect. s:b	bgfree events
1	muon + dijets	muon + p_t^{rel}	[85]	ZEUS	96-00	110	< 1	[0.2, 0.8]	muon jet1(2)	> 2.5 > 7(6)	$[-1.6, 2.3]$ $[-2.5, 2.5]$	834 ± 65	1 : 4	165
2		muon + $p_t^{rel} + \delta$	[52]	H1	99-00	50	< 1	[0.2, 0.8]	muon jet1(2)	> 2.5 > 7(6)	$[-0.6, 1.1]$ $[-2.5, 2.5]$	530 ± 50	1 : 4	120
3		muon + p_t^{rel}	[84]	H1	96	6.6	< 1	[0.1, 0.8]	muon jet1(2)	> 2 > 6(6)	$[-0.9, 1.1]$	470 ± 43	1 : 3	120
4	electr. + dijets	electron + p_t^{rel}	[53]	ZEUS	96-97	38.5	< 1	[0.2, 0.8]	muon jet1(2)	> 1.6 > 7(6)	$[-1.1, 1.1]$ $[-2.4, 2.4]$	140 ± 35	1 : 8	16
5	dijets	incl. lifet.	[55]	H1	99/00	58	< 1	[0.15, 0.8]	track jet1(2)	> 0.5 > 11(8)	$[-1.3, 1.3]$ $[-0.9, 1.3]$	2000 ± 250	1 : 30	64
6	dimuon	muon + muon	[59]	ZEUS	96/00	121	all	all	muon1(2)	> 1.5(0.75)	$[-2.2, 2.5]$	1800 ± 200	1 : 20	81
7	D^{*+} + muon	$K \pi \pi_s$ + muon	[58]	ZEUS	96-00	114	< 1	[0.05, 0.85]	D^{*+} muon	> 1.9 > 1.4	$[-1.5, 1.5]$ $[-1.8, 1.3]$	40 ± 10	1 : 2	16
8	D^{*+} + muon	$K \pi \pi_s$ + muon	[57]	H1	98-00	89	< 1	[0.05, 0.75]	D^{*+} muon	> 1.5 $p > 2$	$[-1.5, 1.5]$ $[-1.7, 1.7]$	66 ± 17	1 : 3	15

No.	Program	Ref.	Default settings								Variations							
			γ PDF	μ_r	μ_f	m_b	ϵ_b	p PDF	γ PDF	μ_r	μ_f	m_b	ϵ_b	Treatment				
1	FMNR	[21]	GRV-G HO	m_T	m_T	4.75	0.0035			[0.5, 2]	[0.5, 2]	[4.5, 5.0]		simult. var.				
2	FMNR	[21]	GRV-G HO	m_T	m_T	4.75	0.0033	MRST1		[0.5, 2]	[0.5, 2]	[4.5, 5.0]	±25%	simult. var.				
3	FMNR	[21]	MRSB	m_T	m_T	4.75	0.006			[0.5, 2]	[0.5, 2]		[0.003, 0.009]	quadr. add.				
4	FMNR	[21]	MRST99	m_T	m_T	4.75	-			[0.5, 2]	[0.5, 2]	[4.5, 5.0]		simult. var.				
5	FMNR	[21]	CTEQ5D	m_T	m_T	4.75	0.0033			[0.5, 2]	[0.5, 2]	[4.5, 5.0]		simult. var.				
6	FMNR	[21]	CTEQ5M	unspecified	m_T	m_T	4.75	-		[0.5, 2]	[0.5, 2]	[4.5, 5.0]		simult. var.				
7	FMNR	[21]	CTEQ5M	GRV-G HO	m_T	m_T	4.75	0.0033	CTEQ5F4	[0.5, 2]	[0.5, 2]	[4.5, 5.0]		quadr. add.				
8	FMNR	[21]	CTEQ5M	GRV-G HO	m_T	m_T	4.75	0.0033		[0.5, 2]	[0.5, 2]	[4.5, 5.0]		simult. var.				

Table 6: Beauty photoproduction measurements discussed in this review. Information is given for each analysis on the beauty tag method, the experiment, the data period, integrated luminosity, Q^2 and y ranges and the cuts on transverse momenta and pseudorapidities of selected final state particles. The last three columns provide information on the number of tagged beauty events, the effective signal to background ratio, as calculated from $s : b = \text{events} : (\sigma(\text{events})^2 - \text{events})$ and the equivalent number of background free events, as calculated from $[\text{events}/\sigma(\text{events})]^2$. In the lower table for each measurement the perturbative NLO calculations are detailed to which the data are compared. Information is given on the used program, the proton and photon parton density functions and the default parameters for the renormalisation and factorisation scales μ_r and μ_f , the b quark mass (in units of GeV) and the ϵ parameter in the Peterson fragmentation function. Information and references for the PDFs can be found in [64]. m_T is defined as $m_T = \sqrt{m_b^2 + p_t^2}$, where p_t is the transverse momentum of the b quark. On the right the variations of the parameter settings are listed, which are used to estimate the uncertainties of the calculation, shown as error bands in the plots.

5.4.1 Analyses using events with a muon and jets

Using a muon from a semileptonic b -decay in dijet events is a well established beauty tagging method. The first publication [84] on beauty production at HERA used this technique. In the more recent H1 and ZEUS analyses [52, 85] which are presented here, the event selection requires a muon with transverse momentum $p_T^\mu > 2.5$ GeV and two jets with $p_T^{\text{jet1(2)}} > 7(6)$ GeV. As detailed in section 4, the determination of the beauty component in the final data sample relies on two observables, the muon relative transverse momentum p_t^{rel} (see figures 22 right and 23 right), which is exploited by ZEUS in [85] and the muon signed impact parameter δ (see figures 22 right and 23 left), which is used together with p_t^{rel} in the H1 analysis [52]. Figure 47 shows the observed muon pseudorapidity distribution in the ZEUS analysis [85]. This is one of

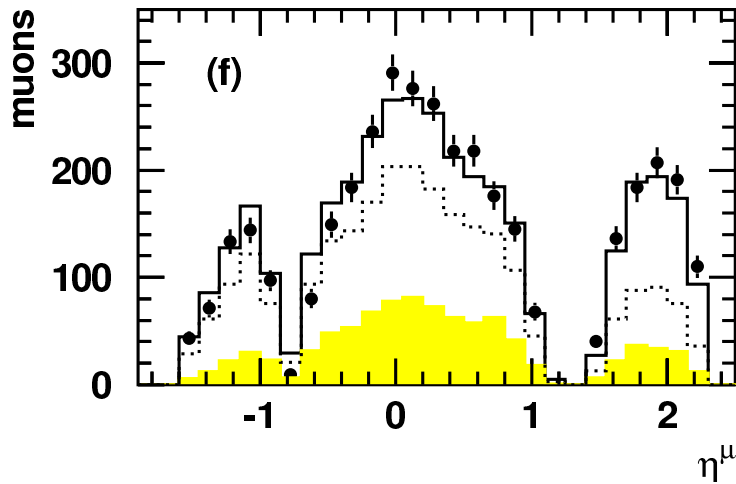


Figure 47: Pseudorapidity distribution of the muon in events with a muon and two jets, from the ZEUS analysis [85]. The data are compared to predictions from PYTHIA [25] (full line) normalised to the data. The shaded histogram shows the estimated beauty component and the dotted line is the sum of charm and beauty.

the very few heavy flavour measurements at HERA, which covers also the forward and backward rapidity regions $|\eta| > 1.5$, where the calorimeter and the muon system provide the necessary detector information. The data in figure 47 are compared to predictions from PYTHIA [25], normalised to the data. A good description is obtained. The contributions from beauty, charm and light quarks are also indicated with relative fractions as predicted from PYTHIA. The measured beauty production cross sections obtained from fits to the p_t^{rel} distributions are shown in the left plot of Figure 48. The H1 measurement [52] is also shown, which is performed in a more restricted central pseudorapidity range. The two measurements agree well in the overlapping region. The data are compared to an NLO calculation [21], which tends to be somewhat lower than the data. Especially in the forward region $1.3 < \eta < 2.3$ the cross section measured by ZEUS is almost a factor of two above NLO, but the experimental error is rather large.

Figure 48 (right) compares the measured cross sections as functions of the muon transverse momentum to the NLO predictions in the respective kinematic ranges of the

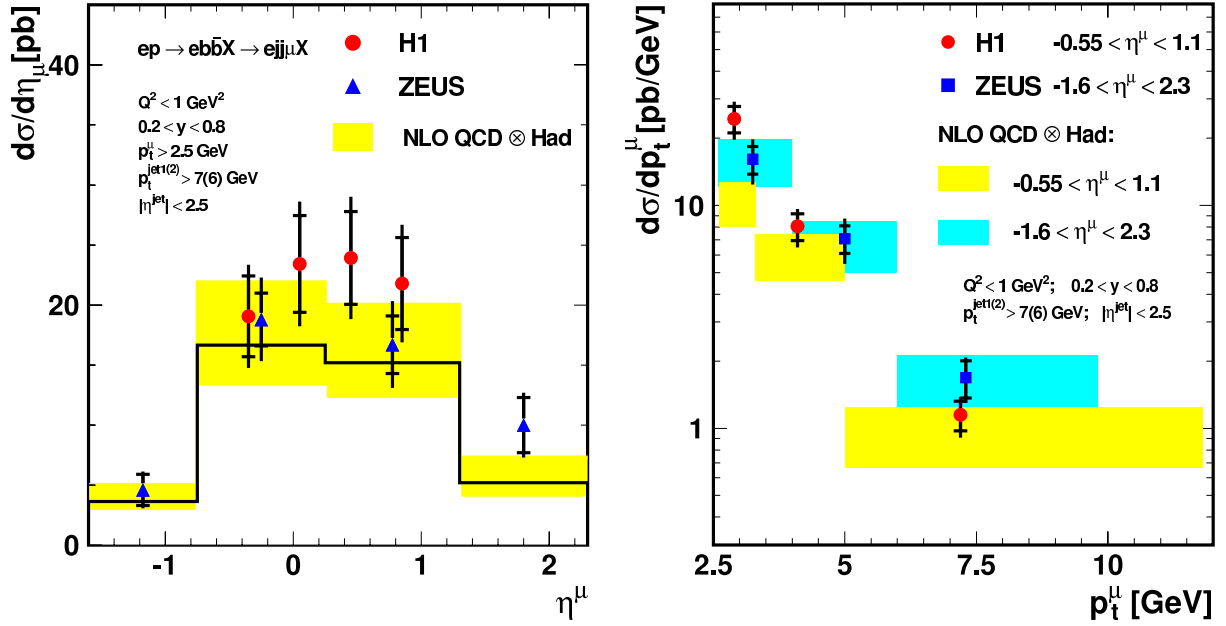


Figure 48: Differential beauty cross sections in photoproduction for events with a muon and two jets as a function of (left) muon pseudorapidity and (right) muon transverse momentum. Shown are the results from the H1 and ZEUS measurements [52, 85]. The data are compared to massive scheme NLO predictions [21].

two measurements. In the lowest bin from 2.5 to 3.3 GeV the H1 measurement exceeds the prediction (light shaded band) by a factor of ~ 2.5 , while at higher transverse momenta a better agreement is observed. Such an excess is not seen in the ZEUS case, where for all bins data and NLO (darker shaded band) agree very well. This experimental discrepancy needs to be clarified in the future.

5.4.2 Double tag analyses using $D^{*+} \mu$ and $\mu\mu$:

The $\mu + jets$ analyses discussed above require two jets with transverse momenta $p_T^{jet1(2)} > 7(6)$ GeV, which correspond to similar cuts for the beauty quarks. Much lower momenta can be probed in the double tag analyses with a muon and a D^{*+} or with two muons in the final state as illustrated in figure 49. The left plot shows the distribution of the invariant mass of the $b\bar{b}$ pair for the $\mu + jets$ analyses [52, 85] (dashed line) and for the H1 $D^{*+} \mu$ measurement [57] (full line), obtained from a PYTHIA [25] Monte Carlo simulation on generator level. For the $D^{*+} \mu$ analysis the spectrum starts right above the kinematic threshold $2m_b \sim 9.5$ GeV while for the $\mu + jets$ measurement it sets off only at around 16 GeV. The right plot in figure 49 shows the distribution of the transverse momentum of the b quark for the ZEUS $\mu\mu$ analysis [59], again from a PYTHIA Monte Carlo simulation. In this analysis, which selects muons with low momentum cuts $p_T^{\mu1(2)} > 1.5(0.75)$ GeV in a wide pseudorapidity range $-2.2 < \eta^\mu < 2.5$, beauty quarks are probed down to zero transverse momenta. This is exploited for a measurement of the total beauty production cross section at HERA. The results of the different double

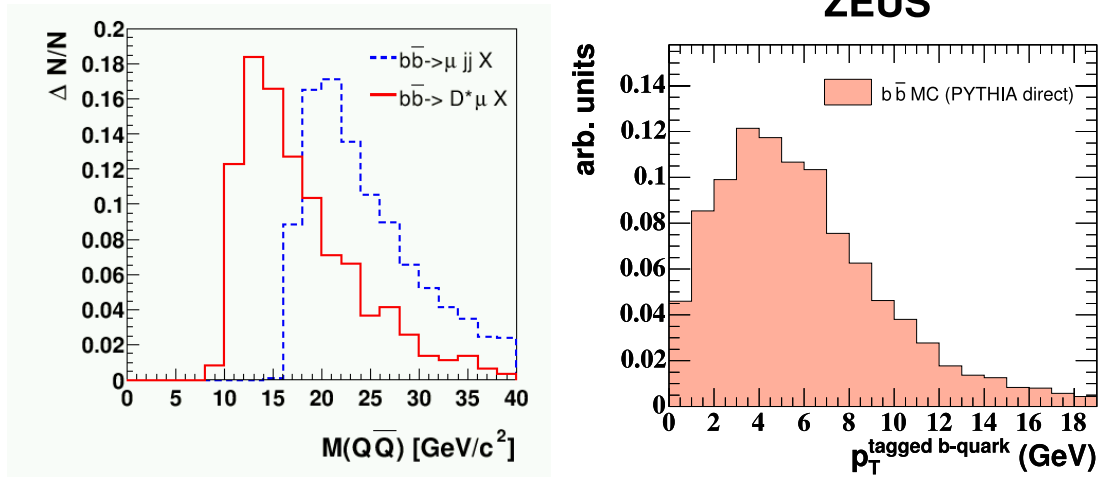


Figure 49: The left plot shows the distribution of the invariant mass of the $b\bar{b}$ quark-antiquark pair for the H1 and ZEUS $\mu + jets$ analyses [52, 85] (dashed curve) compared to the H1 $D^{*+} \mu$ analysis [57] (full curve). The right plot shows the distribution of the transverse momentum of the b quark for the ZEUS $\mu\mu$ analysis [59]. All the results are from PYTHIA [25] Monte Carlo simulations.

tag measurements are depicted in figure 50. ZEUS has performed the $D^{*+} \mu$ measurements separately in photoproduction ($Q^2 < 1 \text{ GeV}^2$) and in DIS ($Q^2 > 2 \text{ GeV}^2$), both results are presented. The data are compared to NLO calculations [21]. All the measurements are above NLO by factors $\sim 2 - 4$. The total experimental errors are all $\geq 50\%$, thus the data over NLO excesses are not very significant for each individual measurement. However, the fact that all measurements exceed NLO, indicates that at low beauty quark transverse momenta close to the kinematic threshold the massive scheme NLO predictions underestimate beauty production. This is a surprise, since in this kinematic regime the NLO predictions are expected to be very reliable.

5.4.3 Summary of beauty photoproduction as functions of transverse momentum and pseudorapidity of the b quark

Figure 51 summarises the HERA beauty results in photoproduction as a function of the b quark transverse momentum. From top to bottom the following measurements are shown, with increasing p_T :

- The H1 and ZEUS $D^{*+} \mu$ and $\mu\mu$ double tag results [57–59]. These analyses cover mainly the region $p_T^b < m_b$.
- The ZEUS $\mu + jets$ [85] and the $e + jets$ results [53]. All these measurements exploit the p_t^{rel} tagging method.
- The H1 $\mu + jets$ results [52], combining the muon p_t^{rel} and δ tagging.

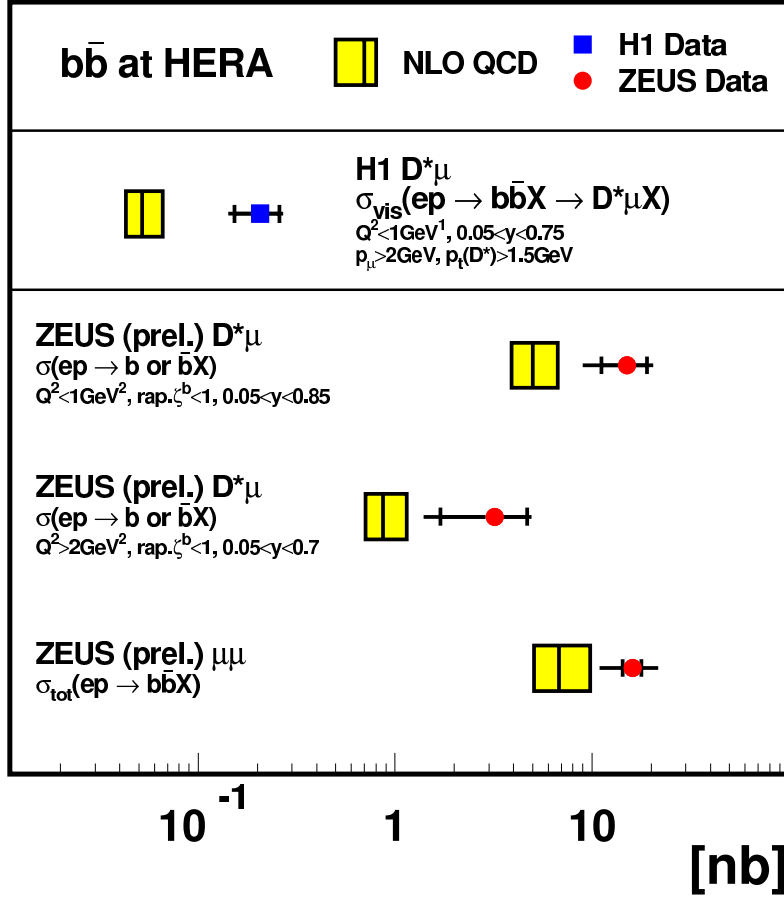


Figure 50: Measured beauty production cross sections for the double tag analyses. From top to bottom the results are shown from the analyses: H1 $D^{*+} \mu$ [57], ZEUS $D^{*+} \mu$ in photoproduction [58] and DIS [58] and ZEUS $\mu\mu$ [59]. The data are compared to NLO predictions [21].

- The H1 *inclusive lifetime tagging* results [55], using the displaced impact parameters of tracks in dijet events. These measurements extend to the highest transverse b quark momenta of ~ 35 GeV.

For the double tag measurements there is no detailed information available for the average p_T of the b quarks, hence only the expected dominant momentum region is indicated by the arrow in the figure. For the other analyses the p_T of the b quark is estimated by the transverse momentum of the leading jet. The data are compared in figure 51 to NLO calculations [21]. For the low transverse momentum region $p_T^b < m_b$ the double tag measurements indicate clearly an excess of the data compared to the NLO prediction. For higher transverse momenta the situation is not that clear. While the ZEUS $\mu + jets$ and $e + jets$ measurements are in good agreement with NLO, the H1 $\mu + jets$ analysis shows an excess in the lowest momentum bin $7 < p_T^b < 11$ GeV, indicating a continuation of the excess which is seen at lower momenta in the double tag analyses. For the H1 *inclusive lifetime tagging* analysis with harder jet cuts, there is an excess seen also for momenta $p_T^b > 11$ GeV that is seen in neither of the $\mu + jets$

analyses, which also extend into this region. These findings need to be verified in the future with measurements of higher precision.

Figure 52 summarises the HERA beauty results in photoproduction as a function of the b quark direction as represented by the pseudorapidity of the muon in the ZEUS $\mu\mu$ analysis [59] (top) and of the leading jet both for the H1 and ZEUS $\mu + jets$ measurements [52, 85] (middle) and for the H1 *inclusive lifetime tagging* analysis [55] (bottom). The average transverse momentum of the b quark increases from top to bottom from a few GeV to more than 11 GeV. The data are compared to predictions from PYTHIA [25](top) or to NLO calculations [21] (middle and bottom). For negative pseudorapidities $\eta < 0$ all the measurements agree with the calculations. However, for positive pseudorapidities $\eta > 0$ the medium and higher p_T data in the middle and bottom plots tend to exceed the calculations. While for the $\mu + jets$ measurements this effect seems rather weak, there is a clearer excess visible for the *inclusive lifetime tagging* measurement. The stronger rise in this analysis towards positive pseudorapidities, compared to the other measurements in the same figure, could be explained by the large proton momentum fraction x_g of the gluon in the PGF process (figure 9) which is needed to produce the two required high p_T jets.

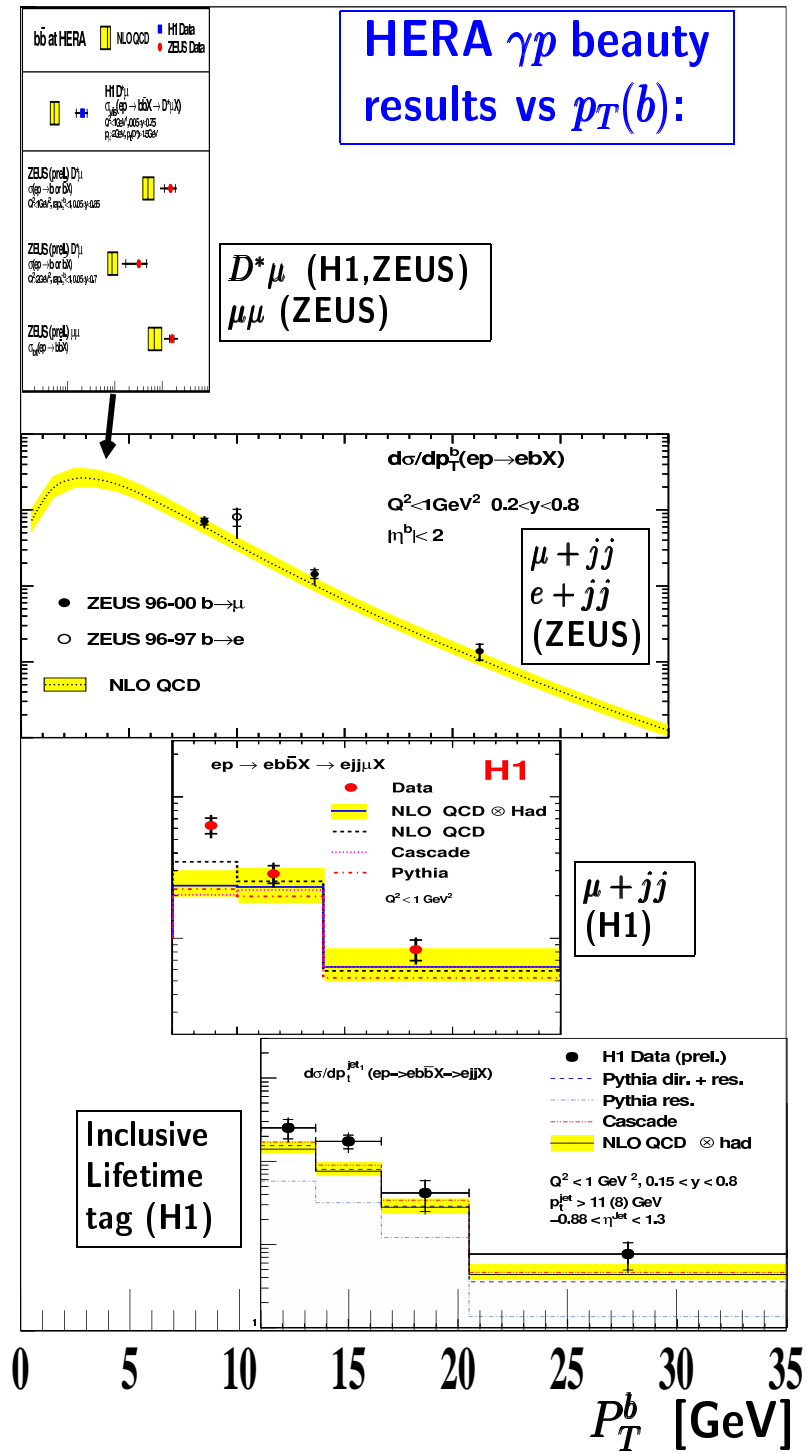


Figure 51: Summary of HERA beauty photoproduction results as a function of the b quark transverse momentum. The insert at the top shows the $D^{*+} + \mu$ and $\mu\mu$ double tag measurements [57–59]. Since for these analyses there is no detailed information available about the average p_T of the b , only the expected dominant momentum region is indicated by the arrow. The lower three plots show from top to bottom the results from the analyses: ZEUS $\mu + jets$ [85] and $e + jets$ [53], H1 $\mu + jets$ [52] and H1 dijets [55] applying inclusive lifetime tagging. For these measurements the p_T of the b quark is estimated by the transverse momentum of the leading jet. The data are compared to NLO calculations [21].

HERA γp beauty results vs η_μ, η_{jet} :

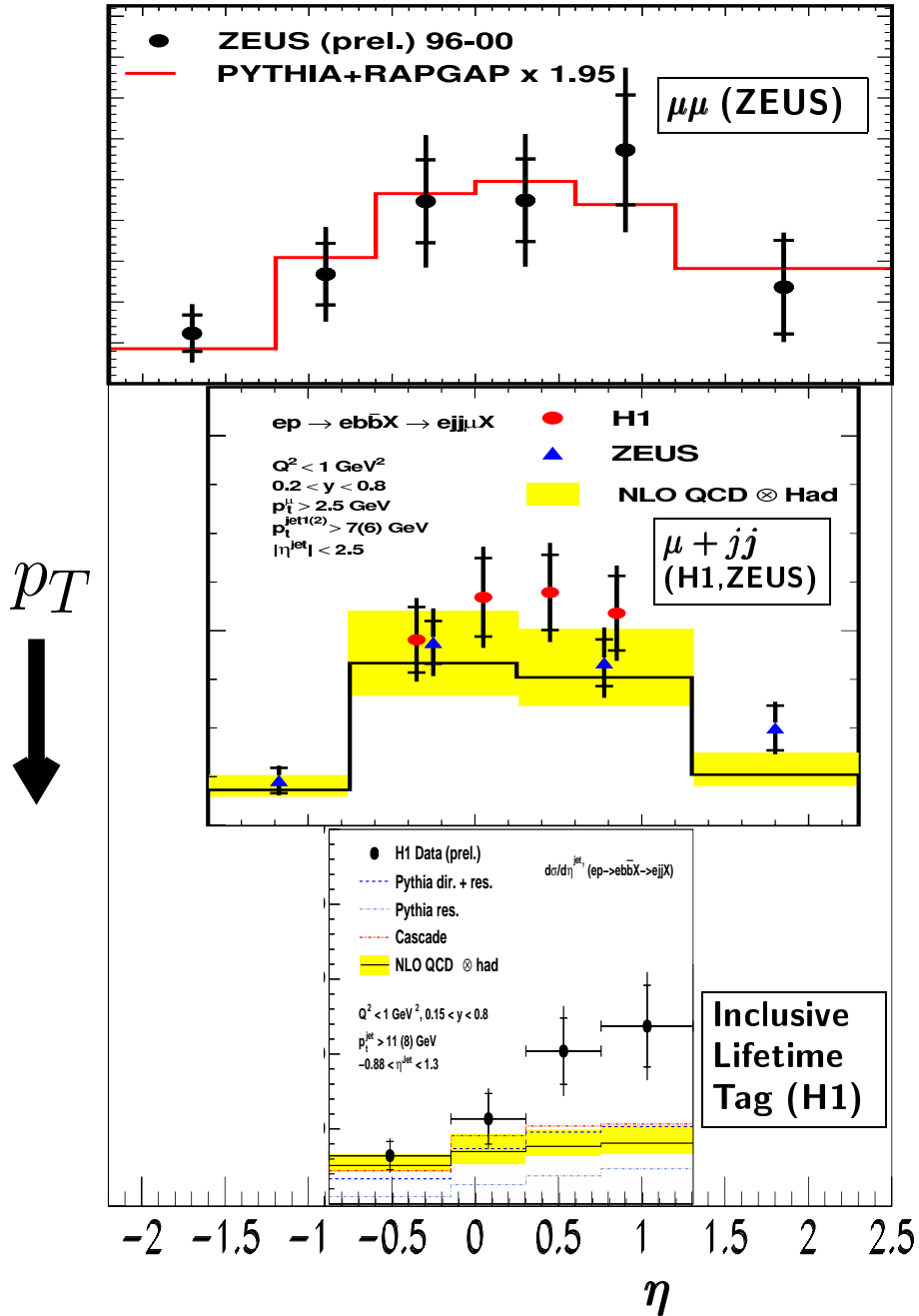


Figure 52: Summary of HERA beauty photoproduction results as a function of the b quark direction, as represented by the pseudorapidity of the muon in the ZEUS $\mu\mu$ analysis [59] (top) and of the leading jet both for the H1 and ZEUS $\mu + jets$ measurements [52, 85] (middle) and for the H1 inclusive lifetime tagging analysis [55] (bottom). The average transverse momentum of the b quark increases from top to bottom from a few GeV to more than 11 GeV. The data are compared to predictions from PYTHIA [25] (top) or to NLO calculations [21] (middle and bottom).

5.4.4 x_γ^{obs} comparisons for beauty, charm and light quark events:

For photoproduction of light quark dijets, the major fraction of events can be attributed to resolved photon interactions while direct photon processes give much smaller contributions. For charm and even more for beauty it is expected that the resolved photon contributions are suppressed. This is due to the additional hard scale provided by the heavy quark masses, which inhibit fluctuations of a photon into a heavy quark pair and furthermore introduce kinematic thresholds. In figure 53 measurements are shown as a function of x_γ^{obs} for three dijet analyses with different flavour tagging. The left plot

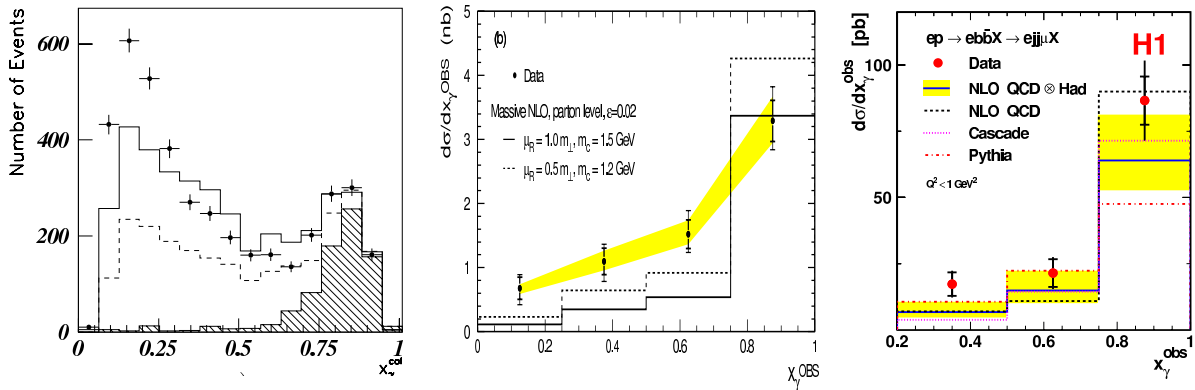


Figure 53: Distributions of the observable x_γ^{obs} for dijet events with different flavour tagging: The left plot shows the measured number of events for a flavour inclusive analysis, from the ZEUS measurement [87], the middle plot the differential cross sections for D^{*+} tagged charm events, from the ZEUS analysis [70] and the right plot the differential cross sections for muon tagged beauty events, from the H1 analysis [52]. The charm and beauty data are compared to NLO predictions [21].

shows a flavour inclusive measurement, dominated by light quarks, from the ZEUS analysis [87], the middle plot the D^{*+} charm results from the ZEUS paper [70] (already shown in figure 45) and the right plot the beauty results from the H1 $\mu + jets$ analysis [52]. For all three analyses x_γ^{obs} is reconstructed from the two leading jets, using equation 12. The jet transverse momentum and pseudorapidity cuts are similar for the three analyses and are approximately $p_t^{jet} > 6$ GeV and $|\eta^{jet}| < 2.4$. For the charm and beauty analyses one jet is restricted to the more central pseudorapidity region because of the D^{*+} and muon kinematic cuts, which leads to some suppression of small x_γ^{obs} events. It is observed that resolved photon like events $x_\gamma^{obs} < 0.75$ are much more prominent in the flavour inclusive sample than for the charm sample and for beauty a further suppression is visible. This supports the above assumptions of a suppression of resolved photon events with the heavy quark mass. On the contrary to the charm case, where the NLO calculation is much too low for $x_\gamma^{obs} < 0.75$, the beauty cross sections are reasonably well described by NLO.

5.5 Beauty production in DIS:

An overview of the presented beauty measurements in deep inelastic scattering is given in table 7.

5.5.1 Analyses using events with a muon and jets

Also for the DIS case the beauty measurements with muon and jets play a leading role. In the H1 and ZEUS analyses [52, 86] presented here, muons with high transverse momenta in the central rapidity region are selected. The jet algorithm is applied in the Breit frame. At least one jet with $p_{t,jet}^{Breit} > 6$ GeV is required, associated with the muon. The measurements cover the Q^2 regions $2 < Q^2 < 100$ GeV² for H1 and $2 < Q^2 < 1000$ GeV² for ZEUS. Figure 54 shows the differential cross sections of the H1 (top) and the ZEUS measurement (bottom) as a function of jet transverse momentum in the Breit frame (left), muon transverse momentum (middle), and muon pseudorapidity (right). The data are compared to massive scheme NLO calculations [22]. The observations

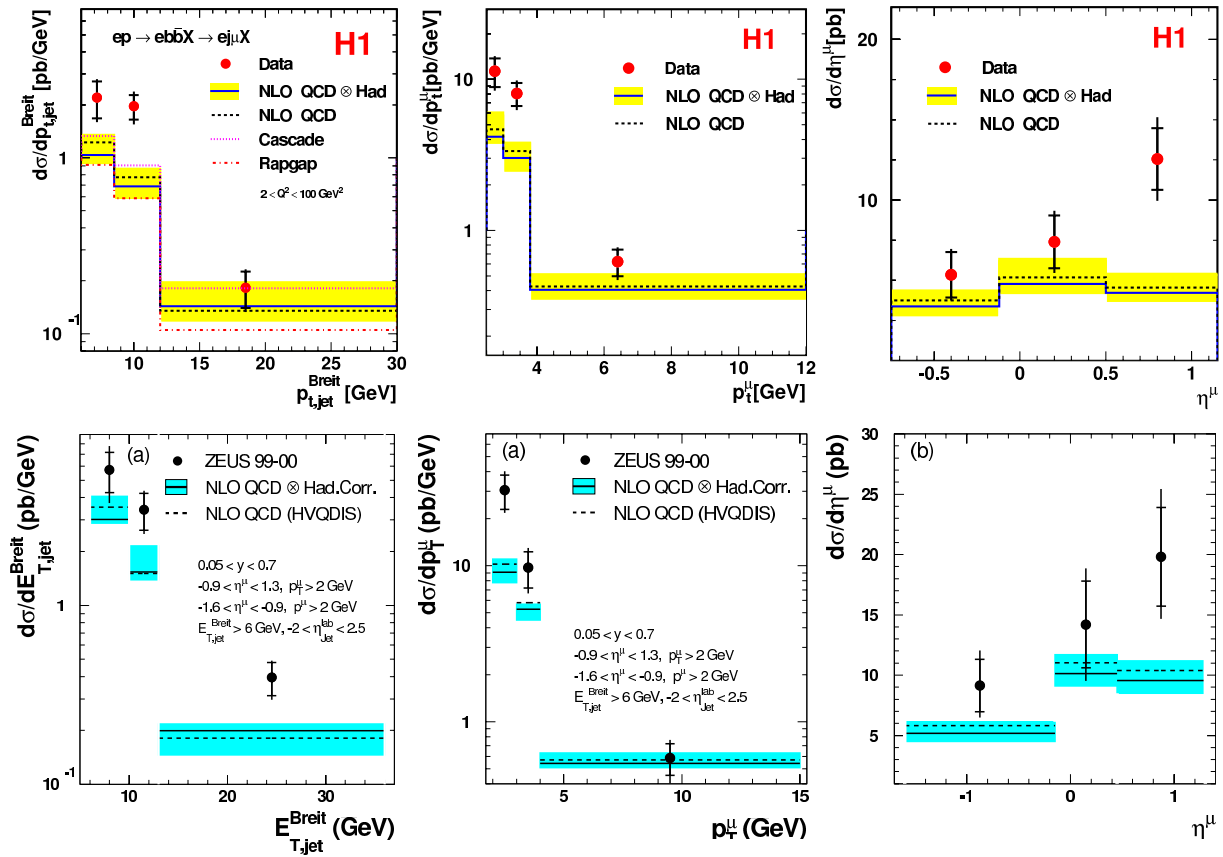


Figure 54: Differential beauty cross sections in DIS, for events with a muon and an associated jet, as a function of (left) jet transverse momentum in the Breit frame, (middle) muon transverse momentum and (right) muon pseudorapidity for the H1 analysis [52] (top) and the ZEUS measurement [86] (bottom).

No.	Analysis	b Tag	Ref.	Exp.	Data	\mathcal{L} [pb^{-1}]	Q^2 [GeV^2]	y	Particle	p_T [GeV]	η	Events	effect. s:b	bgfree events
1	muon + jet	muon + p_t^{rel}	[86]	ZEUS	99-00	72	> 2	[0.05, 0.7]	muon jet	> 2 > 6	[-1.6, 1.3] [-2.0, 2.5]	285 ± 38	1 : 4	50
2		muon + $p_t^{rel} + \delta$	[3]	H1	99-00	50	> 2	[0.1, 0.8]	muon Jet	> 2.5 > 6	[-0.6, 1.1] [-2.5, 2.5]	234 ± 30	1 : 3	64
3	F_2^{bb}	incl. lifet.	[75]	H1	99/00	57	[6, 120]	[0.07, 0.7]	track	> 0.5	[-1.3, 1.3]	2000 ± 200	1 : 20	100
4		incl. lifet.	[54]	H1	99/00	57	> 150	[0.1, 0.7]	track	> 0.5	[-1.3, 1.3]	700 ± 110	1 : 16	40
5	D^{*+} + muon	$K\pi\pi_s$ + muon	[58]	ZEUS	96-00	114	> 2	[0.05, 0.7]	D^{*+} muon	> 1.5 > 1.4	[-1.5, 1.5] [-1.8, 1.3]	11 ± 5	1 : 1.5	4

No.	Program	Ref.	Default settings						Variations					
			p PDF	μ_r	μ_f	m_b	ϵ_b	p PDF	μ_r	μ_f	m_b	ϵ_b	Treatment	
1	HVQDIS	[22]	CTEQ5F4	m_T	m_T	4.75	$\alpha = 27.5$		[0.5, 2]	[0.5, 2]	[4.5, 5.0]		quadr. var.	
2	HVQDIS	[22]	CTEQ5F4	m_T	m_T	4.75	0.0033		[0.5, 2]	[0.5, 2]	[4.5, 5.0]	$\pm 25\%$	simult. var.	
3.4	HVQDIS	[22]	CTEQ5F3	m_T	m_T	4.75								
3.4	MRST	[28]	MRSTQED04	$\sqrt{Q^2}$	μ_r	4.3								
3.4	MRST-NINLO	[29]	unspecified	$\sqrt{Q^2}$	μ_r	4.3								
3.4	CTEQ	[27]	CTEQ6HQ	$\sqrt{m_b^2 + Q^2}$	μ_r	4.5								
5	HVQDIS	[22]	unspecified	$\sqrt{m_b^2 + Q^2}$	μ_r	4.75			[0.5, 2]	[0.5, 2]	[4.5, 5.0]		simult. var.	

Table 7: Beauty DIS measurements discussed in this review. Information is given for each analysis on the beauty tag method, the experiment, the data period, integrated luminosity, Q^2 and y ranges and the cuts on transverse momenta and pseudorapidities of selected final state particles. The last three columns provide information on the number of tagged beauty events, the effective signal to background ratio, as calculated from $s : b = \text{events} : (\sigma(\text{events})^2 - \text{events})$ and the equivalent number of background free events, as calculated from $[\text{events} / \sigma(\text{events})]^2$. In the lower table for each measurement the perturbative NLO calculation is detailed to which the data are compared. Information is given on the used program, the proton density function and the default parameters for the renormalisation and factorisation scales μ_r and μ_f , the b quark mass (in units of GeV) and the ϵ parameter in the Peterson fragmentation function (or α parameter in the Kartvelishvili fragmentation function). Information and references for the PDFs can be found in [64]. m_T is defined as $m_T = \sqrt{m_b^2 + p_t^2}$, where p_t is the transverse momentum of the b quark. On the right the variations of the parameter settings are listed, which are used to estimate the uncertainties of the calculation, shown as error bands in the plots.

for the cross sections as a function of the muon kinematics are very similar for H1 and ZEUS:

1. An excess of data over NLO prediction by a factor ~ 2 is observed towards smaller muon transverse momenta below 4 GeV.
2. The differential cross sections rise towards more positive muon pseudorapidities (i.e. more close to the proton direction), while the NLO calculation predicts a more or less flat behaviour. This resembles the excesses in the more forward direction in charm and beauty photoproduction, as shown in figures 32 and 52, respectively. However, in general the experimental precision of the beauty results is yet to be improved and the pseudorapidity coverage needs to be extended to the more forward direction, before stronger conclusions can be drawn.

The excess seen both by H1 and ZEUS for lower muon transverse momenta is accompanied by an excess at lower jet transverse momenta for H1 but at higher momenta for ZEUS (compare upper and lower left plot in figure 54). More precise measurements are needed to clarify these different findings.

5.6 Summary of beauty photoproduction and DIS results as a function of photon virtuality Q^2

Figure 55 presents a summary of the recent HERA beauty cross section measurements as a function of the photon virtuality Q^2 . All the above presented beauty measurements in photoproduction and in DIS are included in this figure. The histogram shows the ratio of the measured cross sections and the massive scheme NLO predictions based on the programs [21, 22]. Uncertainties of the NLO calculations are not taken into account. The most striking observation is: *most of the data points are above the predictions*. This is seen over the whole Q^2 range $0 < Q^2 < 1000 \text{ GeV}^2$. There are also some analyses which are in good agreement with NLO: These are the ZEUS $\mu + jets$ photoproduction measurement [85] (open square point) and the H1 measurements [54, 75] of the structure function $F_2^{b\bar{b}}$ (triangle points) using inclusive lifetime tagging. The latter measurements are discussed in more detail in section 5.8. Especially for the $F_2^{b\bar{b}}$ measurements *mixed scheme* NLO calculations are provided from MRST [28] and CTEQ [27] which are shown as lines in figure 55. The MRST prediction is significantly above the massive calculation and CTEQ. According to [88] this is mainly due to the different implementation in CTEQ and MRST of the transition from the massive scheme at low Q^2 to the massless NLO scheme at high Q^2 . Furthermore in MRST there are already terms included which would be regarded in CTEQ as next-to-next-to-leading order (NNLO) contributions and which increase the cross sections. With the present experimental uncertainties the $F_2^{b\bar{b}}$ data cannot yet distinguish between these differences.

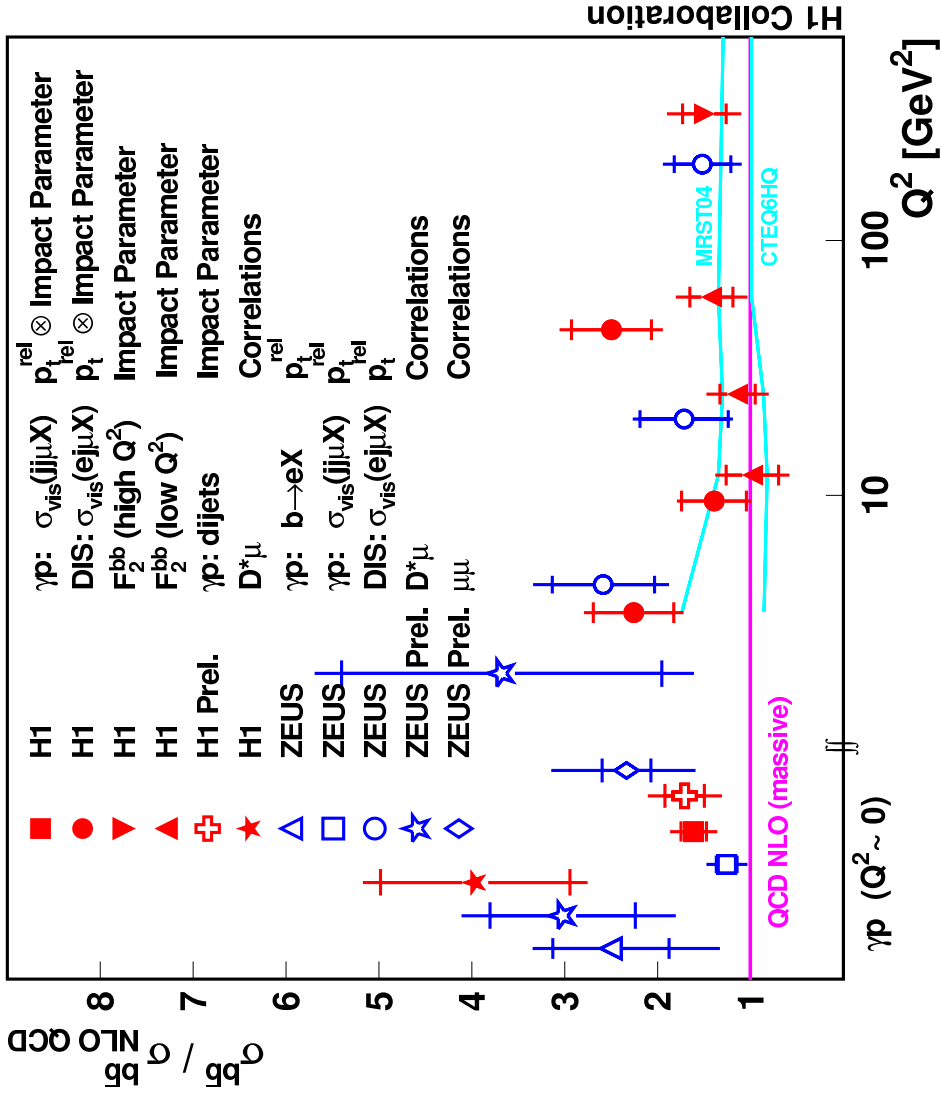


Figure 55: Ratio of recent beauty production cross section measurements at HERA and massive scheme NLO QCD predictions using the programs [21, 22] as a function of the photon virtuality Q^2 . The predictions from the VFNS NLO calculations by MRST [28] and CTEQ [27] for the DIS kinematic regime $Q^2 > 2 \text{ GeV}^2$ are also shown (lines), which are specifically provided for the F_2^{bb} measurements (full triangle points).

Key	Ref.	Signature	p_T cuts
Photoproduction			
☆	[58]	$D^* \mu$	low
★	[57]	$D^* \mu$	low
□	[85]	2 jets+ μ	medium
■	[52]	2 jets+ μ	medium
+	[55]	tracks	high
◇	[59]	$\mu\mu$	low
DIS			
☆	[58]	$D^* \mu$	low
▲	[75]	tracks	low
▼	[54]	tracks	low
●	[52]	1 jet+ μ	medium
○	[86]	1 jet+ μ	medium

5.7 Charm and Beauty cross sections at other colliders

It is interesting to compare the HERA charm and beauty production measurements with results from other colliders. At **LEP** this can be studied in $\gamma\gamma$ collisions, which involve direct and resolved photon processes as shown in figure 56 (left) for the beauty case. In general, $\gamma\gamma$ collisions at LEP are very suitable for investigations of the resolved photon structure. Cross sections results [89] from L3 are shown in figure 56 (right). The charm data using fully reconstructed D^{*+} mesons are well described by predictions based on NLO perturbative QCD in the massive scheme. However, for beauty production tagged with leptons from semileptonic b decays and using the p_t^{rel} observable (section 4), there is an excess by a factor ~ 3 . This excess comes as a surprise, i.e. its origin is not well understood.

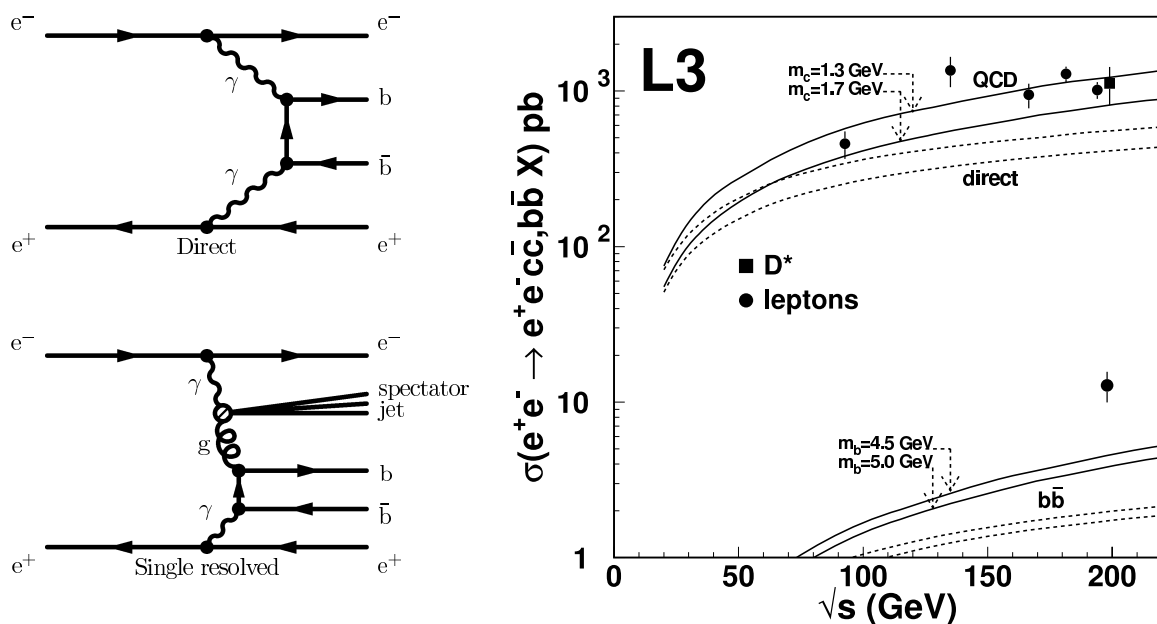


Figure 56: Left: Feynman diagrams for beauty production in direct and resolved photon interactions in $\gamma\gamma$ collisions at LEP. Right: Measured charm and beauty production cross sections in $\gamma\gamma$ collisions compared to NLO QCD predictions, from the L3 publication [89].

At the **TEVATRON** $p\bar{p}$ collider charm and beauty production is dominated by the diagrams shown in figure 57. In order to obtain reliable predictions a good knowledge of the proton gluon density is needed, which enters twice in the gg fusion diagrams. In fact due the similar proton beam energies at HERA and at TEVATRON of ~ 1 TeV also the relevant proton momentum fractions carried by the gluons which enter the PGF processes at HERA (figure 9) and the TEVATRON gg fusion processes are similar. The HERA data provide currently most of the information on the proton gluon density which is needed for predictions of heavy flavour production at TEVATRON or LHC. The gluon densities are obtained predominantly from the scaling violations of the inclusive

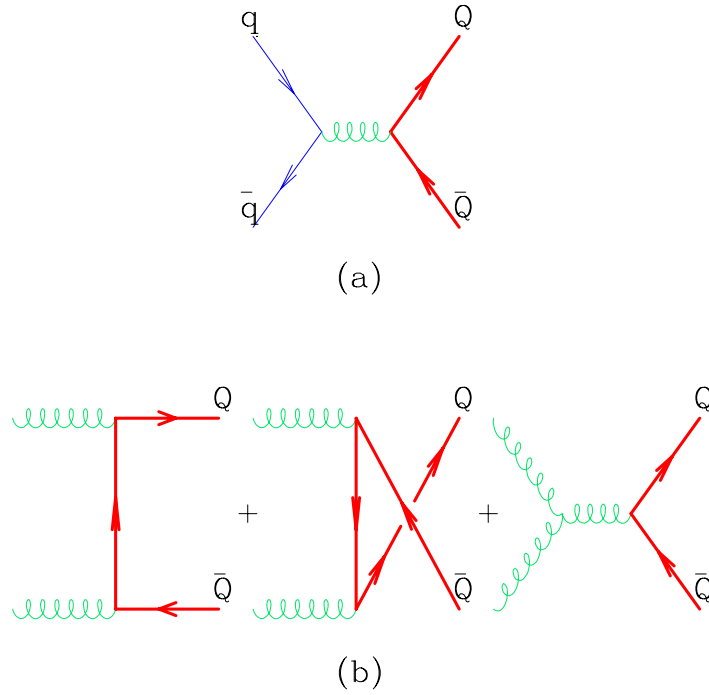


Figure 57: Leading order processes for charm and beauty production in $p\bar{p}$ collisions at the TEVATRON.

structure function F_2 at HERA and are available as parton density functions from one of the PDF fitter groups, e.g. CTEQ and MRST.

Recent charm results obtained with D -mesons from TEVATRON RUN II are shown in figure 58, for a discussion see [90]. The differential cross sections as a function

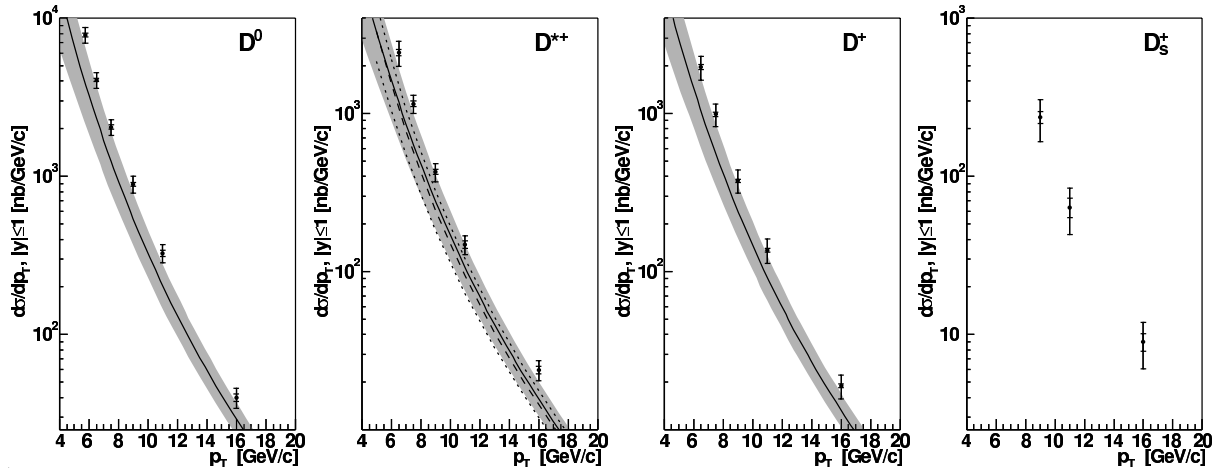


Figure 58: TEVATRON RUN II charm results with different D mesons as a function of the transverse momentum of the mesons, compared to FONLL predictions. The data are shown as the points with the error bars, the predictions as central curves with shaded error bands.

of the transverse momentum of the different studied D mesons are somewhat higher

than the central predictions from FONLL, but agree with the upper edges of the theory uncertainty bands.

For the TEVATRON RUN I beauty data there is a well known excess of data over massive scheme NLO, as illustrated in figure 59 and discussed e.g. in [91]. Results

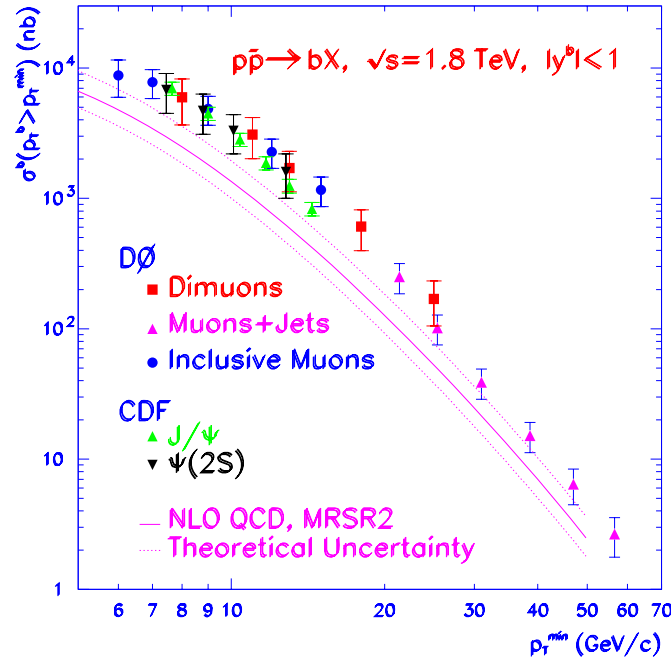


Figure 59: TEVATRON beauty results from RUN I compared to predictions from NLO calculations in the massive scheme.

from RUN II are in much better agreement with new predictions from FONLL [30] as illustrated in figure 60. In the recent article [91] by Cacciari with the title 'Rise and Fall of the Bottom Quark Production Excess' this development is discussed in detail. The main reasons for the much better agreement are:

- The measured cross sections at RUN II are surprisingly lower by $\sim 25\%$ compared to RUN I, despite an increase in the centre-of-mass energy by about 10%..
- The proton gluon density from the recent PDF set CTEQ6M, which is used in the new FONLL calculation, is significantly higher than the one used for the previous calculations.
- An improved treatment of the beauty fragmentation is applied for FONLL: The fragmentation is obtained directly by using the FONLL theory predictions in a fit to LEP beauty fragmentation data. As a result the cross section predictions are raised.

A good description is also provided by the NLO Monte Carlo program MC@NLO [39] as shown in figure 60. The possible lesson to learn for HERA is: there could be

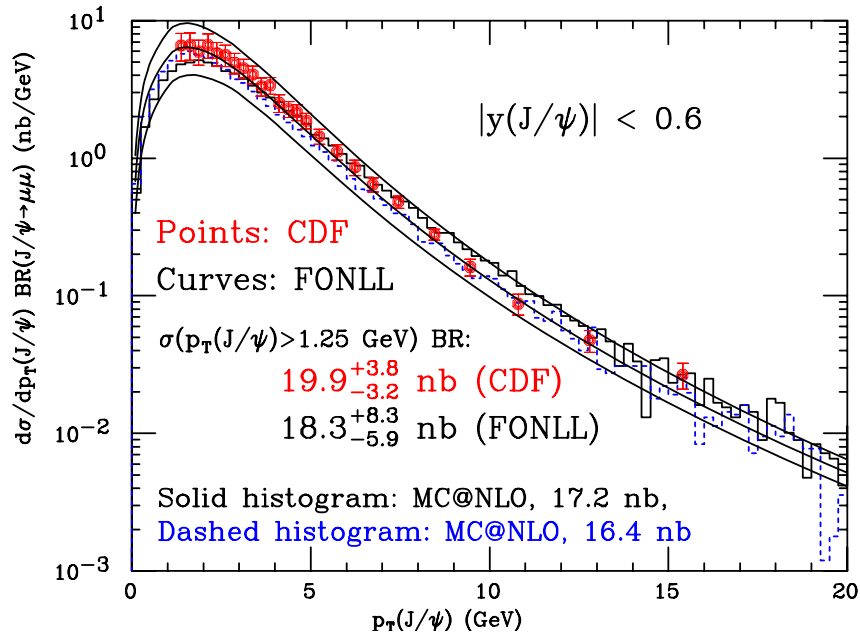


Figure 60: Recent TEVATRON RUN II beauty results compared to predictions from FONLL and MC@NLO, taken from [91].

also substantial improvements for NLO calculations of HERA beauty production, which could bring a better agreement with the data that tend to lie above available predictions (see figure 55). Unfortunately both FONLL and MC@NLO calculations are not yet available for the HERA beauty case.

5.8 Charm and beauty contributions $F_2^{c\bar{c}}$ and $F_2^{b\bar{b}}$ to the proton structure function F_2

This section discusses how much charm and beauty events contribute to inclusive deep inelastic ep scattering in the kinematic range $1 < Q^2 < 1000 \text{ GeV}^2$. The inclusive ep scattering is described by the following well known formula:

$$\frac{d^2\sigma}{dx dQ^2} = \frac{2\pi\alpha^2}{xQ^4} [(1 + (1 - y)^2)F_2 - y^2 F_L]. \quad (13)$$

The dominant contributions arise from the structure function F_2 . In the probed kinematic range electroweak corrections are small and hence are omitted. In the leading order quark parton model picture F_2 is given by

$$F_2 = \sum_i x e_i^2 (q_i(x) + \bar{q}_i(x)), \quad (14)$$

where q_i (\bar{q}_i) are the quark (antiquark) densities in the proton and e_i the quark electric charges. The sum runs over the light quark flavours u , d and s . In the following the charm production case is discussed, but the same arguments also hold for beauty. If one treats the charm quark as massless, which is expected to be a reasonable approximation for $Q^2 \gg m_c^2$, the sum in equation (14) runs also over c quarks. This is the QPM scattering domain for charm. For lower Q^2 , however, the situation is different, since it is experimentally known (figure 41) that here the dominant mechanism is photon gluon fusion. This makes a simple interpretation of the charm contribution to F_2 in terms of a charm quark density in the proton, as expressed by equation (14), impossible. Nevertheless one can still define charm proton structure functions $F_2^{c\bar{c}}$ and $F_L^{c\bar{c}}$, that simply account for the parts of F_2 and F_L attributed to events with charm quarks in the final state:

$$\frac{d^2\sigma^{c\bar{c}}}{dx dQ^2} = \frac{2\pi\alpha^2}{xQ^4} [(1 + (1 - y)^2)F_2^{c\bar{c}} - y^2 F_L^{c\bar{c}}]. \quad (15)$$

This is illustrated in figure 61 for $F_2^{c\bar{c}}$, neglecting the longitudinal structure functions.

5.8.1 Experimental aspects and extrapolation

For the determination of $F_2^{c\bar{c}}$ one has to determine the total charm production cross section $\frac{d^2\sigma^{c\bar{c}}}{dx dQ^2}$ in a given Q^2 and x range. The $F_2^{c\bar{c}}$ measurements presented in this essay are based on D^{*+} tagging, using the golden decay $D^{*+} \rightarrow K^- \pi^+ \pi_s^+$, for the analyses [77, 80], or on inclusive lifetime tagging, exploiting the displaced impact parameters of tracks from the decays of heavy flavoured hadrons, for the analyses [54, 75]. Both tagging methods were detailed in section 4. Figure 62 shows the two-dimensional distribution of D^{*+} mesons as a function of the D^{*+} transverse momentum and polar angle from a DJANGO [37] Monte Carlo simulation of charm events in DIS for

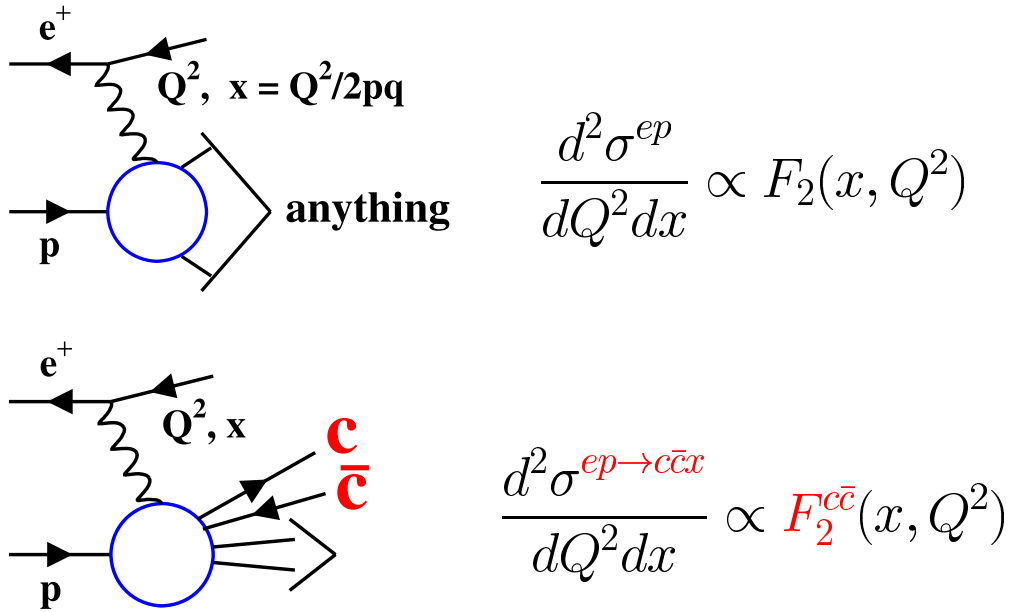


Figure 61: Illustration of flavour inclusive ep scattering (upper diagram) and charm production (lower diagram) and the relations of the corresponding cross sections to the structure functions F_2 and $F_2^{c\bar{c}}$ (on the right).

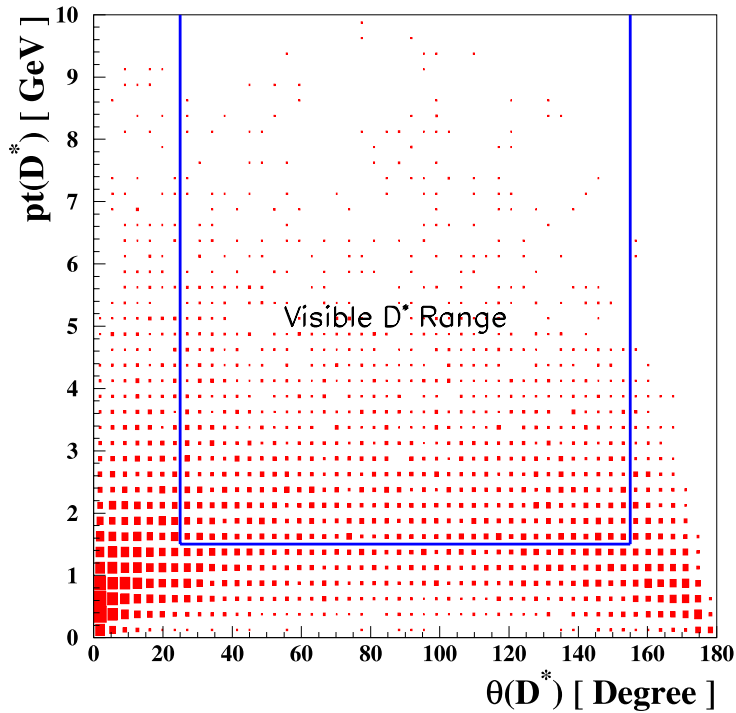


Figure 62: Two-dimensional distribution of D^{*+} mesons as a function of D^{*+} transverse momentum and polar angle, from a DJANGO [37] Monte Carlo simulation at the generator level performed in the kinematic range $Q^2 > 1 \text{ GeV}^2$. The region enclosed by the lines indicates the experimentally accessible range, also denoted as Visible D^{*+} range.

$Q^2 > 1 \text{ GeV}^2$. The simulation is performed only at the generator level without detector simulation. The D^{*+} measurements are restricted to the indicated visible kinematic range $p_T^{D^{*+}} > 1.5 \text{ GeV}$ and $|\eta^{D^{*+}}| < 1.5$ due to acceptance limitations for the D^{*+} decay tracks in the central trackers (see figure 16). Only a relatively small fraction of $\sim 10\%$ of the D^{*+} mesons is produced in this visible range. However, for determining the total charm cross section, one needs to know the D^{*+} production rates over the *whole* D^{*+} kinematic phase space. Since this information is experimentally inaccessible, the measured results in the visible D^{*+} range are extrapolated to the complete range with the help of Monte Carlo simulations. The extrapolation factors strongly depend on Q^2 and x . They vary from ~ 10 for Q^2 of a few GeV^2 to ~ 2 for $Q^2 > 100 \text{ GeV}^2$. This extrapolation introduces large model uncertainties. For instance, in the H1 analysis [80], the extrapolation factors differ up to 30% when using the CASCADE [34] program instead of RAPGAP [35].

The inclusive lifetime tagging of charm and beauty events, as pioneered for HERA by H1 in the high $Q^2 \geq 150 \text{ GeV}^2$ analysis [54] provides much larger kinematic acceptances than the D^{*+} tagging. All events are accepted with at least one charged track with minimum transverse momentum $p_T > 0.5 \text{ GeV}$ in the polar angular region $30^\circ < \theta < 150^\circ$. Figure 63 shows for the analysis [54] the fraction of charm and beauty events as a two-dimensional function of Q^2 and x for which at least one charm or beauty decay track exists, that passes these kinematic cuts. Thus these fractions give directly the kinematic acceptances. The boxes in the figure indicate the (Q^2, x) bins which are selected for the $F_2^{c\bar{c}}$ and $F_2^{b\bar{b}}$ measurements in [54]. The results are from a RAPGAP [35] Monte Carlo simulation: the achieved average acceptances are in all bins above 90%, both for charm and beauty. Thus the remaining extrapolation uncertainties are very small and concerning this point the inclusive lifetime method provides a by far better systematic control than the D^{*+} tagging.

5.8.2 $F_2^{c\bar{c}}$ Results

Figure 64 shows a compilation of the most precise HERA $F_2^{c\bar{c}}$ results as a function of x for various Q^2 values, from the H1 and ZEUS D^{*+} analyses [77, 80, 92] and from the recent H1 inclusive lifetime tagging measurements [54, 75] (shown as square points and marked as VTX in the figure legend). A huge kinematic range is probed, from $Q^2 = 2 \text{ GeV}^2 \approx m_c^2$ to $Q^2 = 500 \text{ GeV}^2 \gg m_c^2$. *Bjorken* x varies over three orders of magnitude from ~ 0.00003 to ~ 0.03 . All the H1 and ZEUS measurements agree well. The H1 inclusive lifetime tagging measurements exhibit typically a factor of two smaller statistical errors than the D^{*+} analyses, demonstrating the power of this technique. $F_2^{c\bar{c}}$ is observed to increase strongly towards smaller x and larger Q^2 . This reflects the behaviour of the gluon density in the proton which drives the photon gluon fusion process. For illustration the gluon density, as determined in the H1 analysis [5] from the scaling violations of F_2 , is shown in the bottom of figure 64. The density is presented as a function of the proton momentum fraction x_g carried by the gluon, which is always

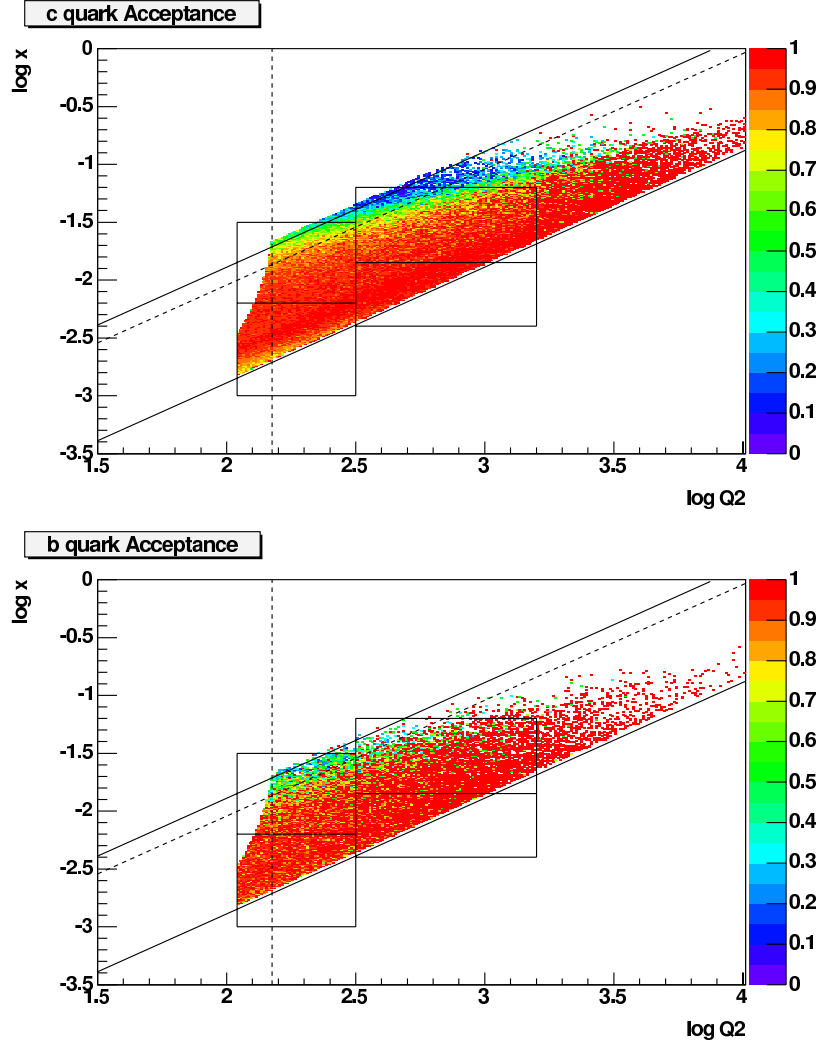


Figure 63: Charm and beauty quark kinematic acceptances for the H1 inclusive lifetime tagging analysis [54]. More details are given in the main text.

larger than Bjorken x (see figure 9). Obviously the rises of $F_2^{c\bar{c}}$ and of the gluon density are strongly correlated.

The $F_2^{c\bar{c}}$ data are compared in figure 64 to the predictions of a massive scheme NLO calculation [22], using the proton parton densities from the ZEUS NLO QCD fit [78]. The NLO curves describe the data well for all values of x and Q^2 . This is, first of all, an impressive confirmation of the QCD hard scattering factorisation theorem [4], which states that the gluon density determined from inclusive scattering is universal and can be used to predict exclusive hard processes, such as charm production. The uncertainty of the theoretical prediction shown in figure 64 is that from the ZEUS PDF fit propagated from the experimental uncertainties of the fitted inclusive data. At the lowest Q^2 , the uncertainty in the $F_2^{c\bar{c}}$ data is comparable to the PDF uncertainty shown. This implies, that the available HERA charm data could be used as an additional constraint on the proton gluon density. In fact this has been already done by the CTEQ

group for the CTEQ6HQ [27] parton density functions, using the HERA D^{*+} results available at that time.

The relative contribution of charm events to DIS is given by the ratio $F_2^{c\bar{c}}/F_2$, which is shown in figure 65 as a function of x for various Q^2 values. The F_2 values are taken from the ZEUS NLO QCD fit [78]. $F_2^{c\bar{c}}/F_2$ rises towards lower x and larger Q^2 and reaches maximum values of $\sim 30\%$ for $Q^2 \geq 30 \text{ GeV}^2$ at the lowest covered x values. This is not too far from the *flavour democratic limit* value of $4/11$, where c and b quarks can be treated as massless sea quarks like u , d and s . Neglecting the scattering with valence quarks, the contributions of the different quark flavours i to F_2 is then proportional to q_i^2 , the squared electric charge of the quark (see table 8). As can

	u	d	s	c	b
$F_2^{q\bar{q}}/F_2$	$\frac{4}{11}$	$\frac{1}{11}$	$\frac{1}{11}$	$\frac{4}{11}$	$\frac{1}{11}$

Table 8: Relative quark flavour contributions to F_2 in the 'democratic flavour' limit, where the proton consists of massless u , d , s , c and b sea quarks.

be seen in figure 65 the ratio $F_2^{c\bar{c}}/F_2$ flattens off towards small values of x , e.g. for $Q^2 = 2 \text{ GeV}^2$ and $x < 10^{-3}$. This is due to the fact that in this kinematic region photon gluon fusion is the dominant process in ep scattering, also for light quark events. On the contrary, towards larger x , the structure function F_2 is dominated more and more by QPM scattering of light sea and valence quarks (figure 1) and hence the relative charm contribution is decreasing.

Figure 66 shows a comparison of of the $F_2^{c\bar{c}}$ results with two mixed scheme NLO calculations from CTEQ [27] and MRST [28]. A subset of the the same data shown in figure 64 is presented. The results are given in the form of reduced cross sections defined as

$$\tilde{\sigma}^{c\bar{c}}(x, Q^2) = \frac{d^2\sigma^{c\bar{c}}}{dx dQ^2} \frac{xQ^4}{2\pi\alpha^2(1 + (1 - y)^2)}. \quad (16)$$

$\tilde{\sigma}^{c\bar{c}}$ and $F_2^{c\bar{c}}$ differ only by the rather small F_L contributions (see equations 15 and 16). Both CTEQ and MRST describe the charm data in figure 66 similarly well as the massive scheme calculation [22] does in figure 64. This means that the massive and the mixed scheme are rather indistinguishable in the probed kinematic regime. A similar conclusion is drawn in [93], where the different scheme calculations are directly compared with each other. Figure 67 shows the $F_2^{c\bar{c}}$ measurements as a function of Q^2 for various x values, using again a subset of the measurements that were presented in figure 64. Large positive scaling violations are observed, i.e. an increase of $F_2^{c\bar{c}}$ for fixed x with growing Q^2 . Here significant differences are found between the CTEQ and MRST NLO calculations for $Q^2 < 10 \text{ GeV}^2$. In general CTEQ and MRST differ in the way the transition from the massive to the massless regimes is handled. According to [88] these differences are larger than the effects from the different MRST and CTEQ proton gluon densities. While MRST describe the data reasonably well, CTEQ falls of

too steeply towards the lowest Q^2 values. For the first time a calculation is available in next-to-next-to-leading order (NNLO) [29] as provided very recently by MRST. This NNLO calculation predicts up to 50% lower cross sections than the NLO calculation from the same group. This is quite interesting, since it indicates that the commonly assumed NLO uncertainties could be underestimated. However, the NNLO calculation does not lead to an improved data description, in fact it tends to systematically under-shoot the data in figure 67. It should be also stated that the NNLO calculation uses two approximations [29]: First of all the exact NNLO hard matrix elements for massive quark production are presently not known and an approximation is used. Second of all the PDFs used in the NNLO calculation are not yet fully matched to the applied NNLO scheme. Hence further refinement of the theory calculations are highly desirable and can be hopefully provided in the future.

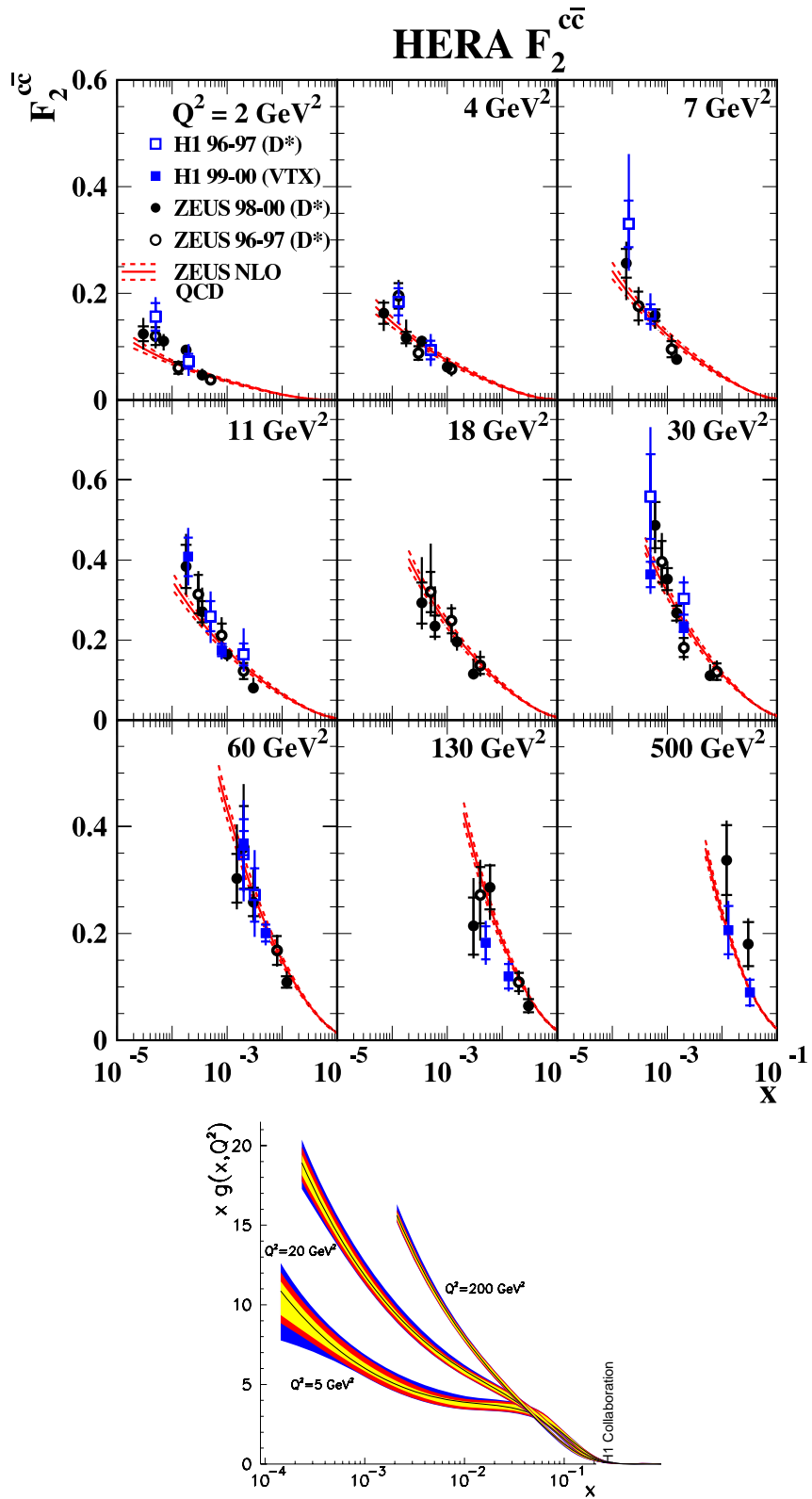


Figure 64: $F_2^{c\bar{c}}$ results as a function of x for various Q^2 values, from the H1 and ZEUS D^{*+} analyses [77, 80, 92] and from the H1 inclusive lifetime tagging measurements [54, 75] (shown as square points and marked as VTX in the figure legend). The data are compared to a massive scheme NLO prediction [22] using the ZEUS NLO fit results [78] for the proton parton densities. The lower plot shows for comparison the proton gluon density as a function of the proton momentum fraction x_g carried by the gluon, for three different Q^2 values, as determined in [5].

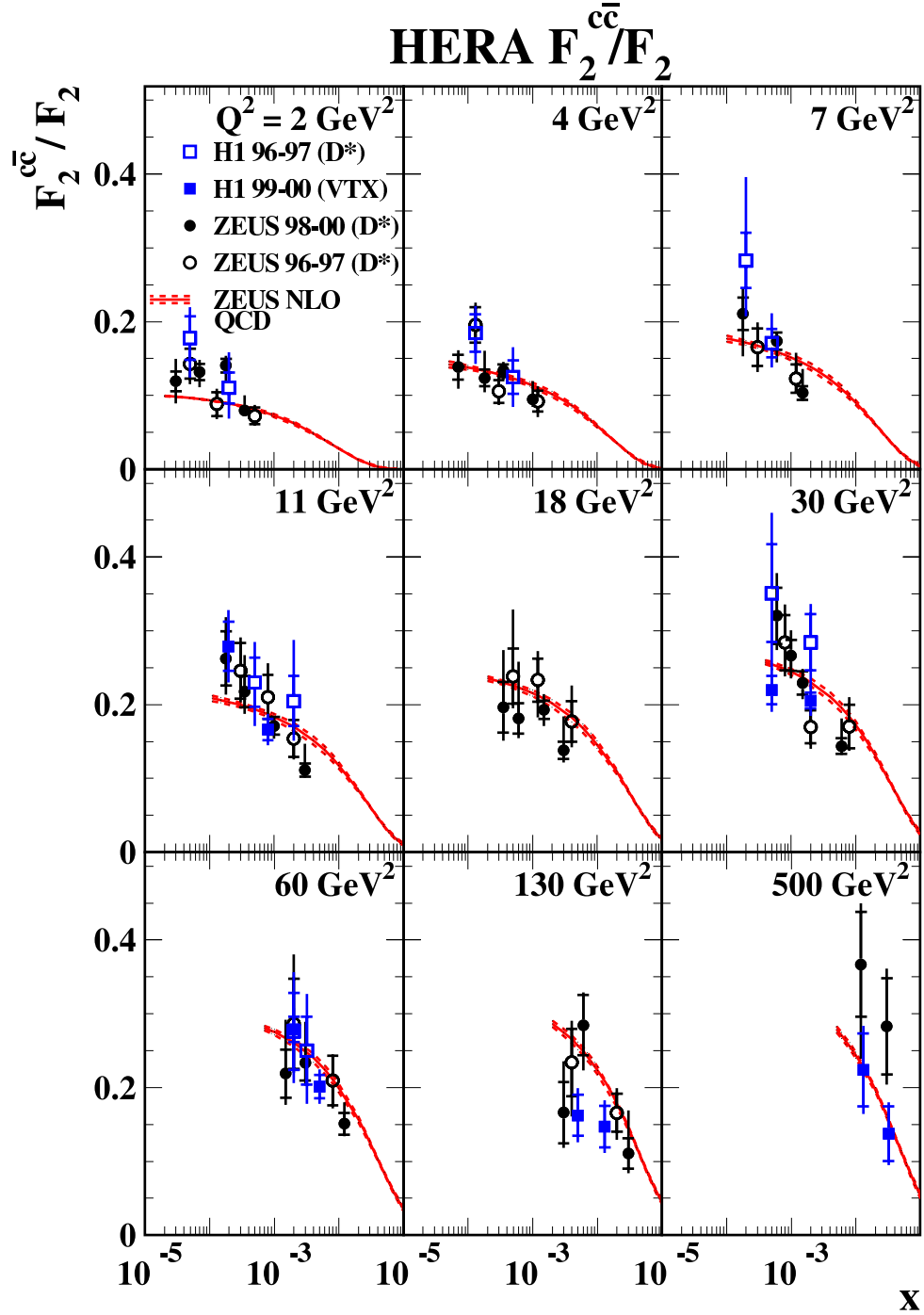


Figure 65: Fractional contribution $F_2^{c\bar{c}}/F_2$ of charm events to inclusive ep -scattering as a function of x for various values of Q^2 . The results shown are from the H1 and ZEUS D^{*+} analyses [77, 80, 92] and from the H1 inclusive lifetime tagging measurements [54, 75] (shown as square points and marked as VTX in the figure legend). The data are compared to a NLO prediction [22] in the massive scheme, using the ZEUS NLO fit results [78] for the proton parton densities.

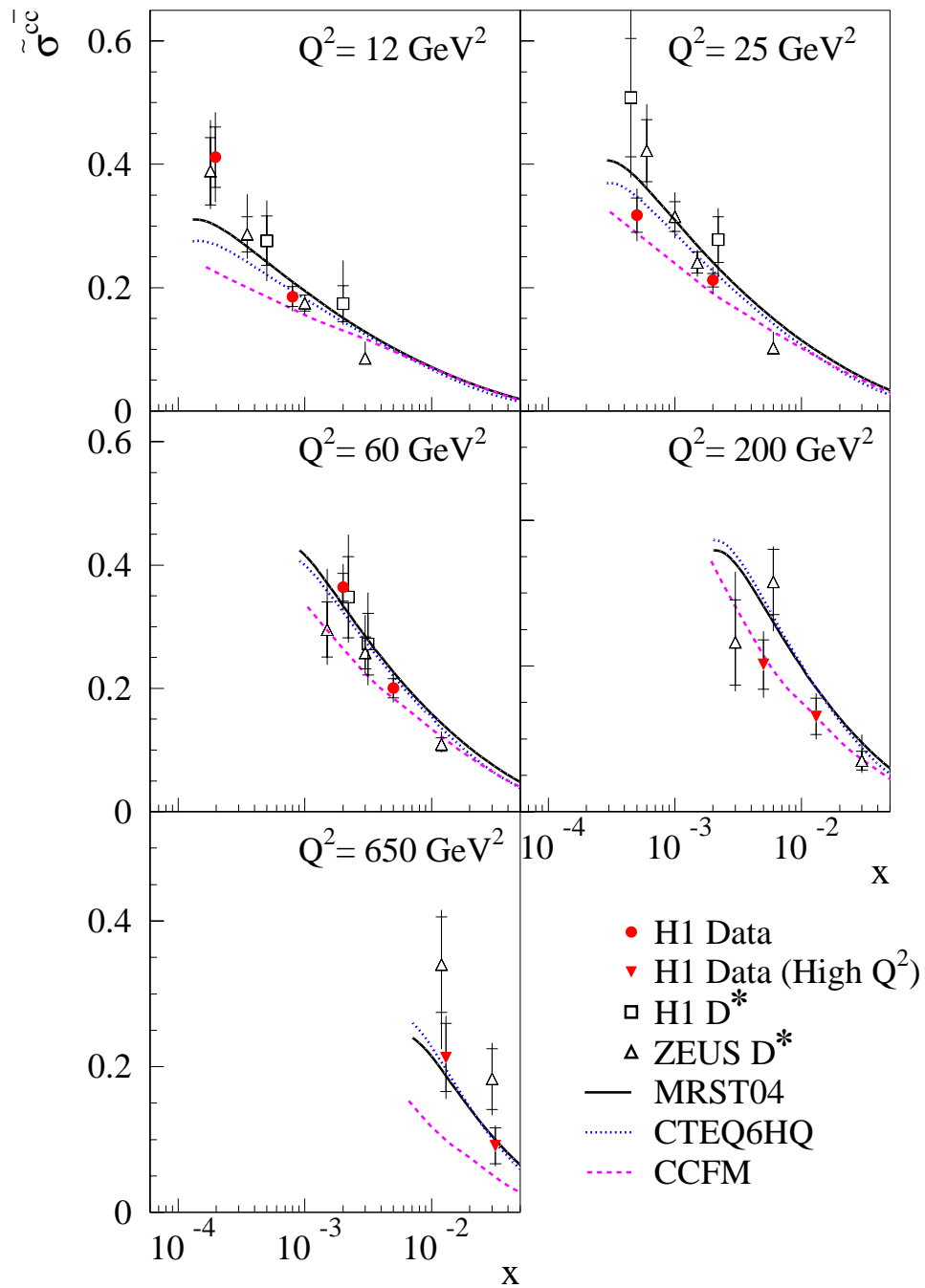


Figure 66: Measured reduced cross section $\tilde{\sigma}^{cc}$ as a function of x for five different Q^2 values, from the H1 inclusive lifetime tagging analysis [75] (shown as full circles and full triangles). The results from the H1 and ZEUS D^{*+} analyses [77, 80, 92] are also shown. The data are compared to two mixed scheme NLO calculations from CTEQ [27] and MRST [28].

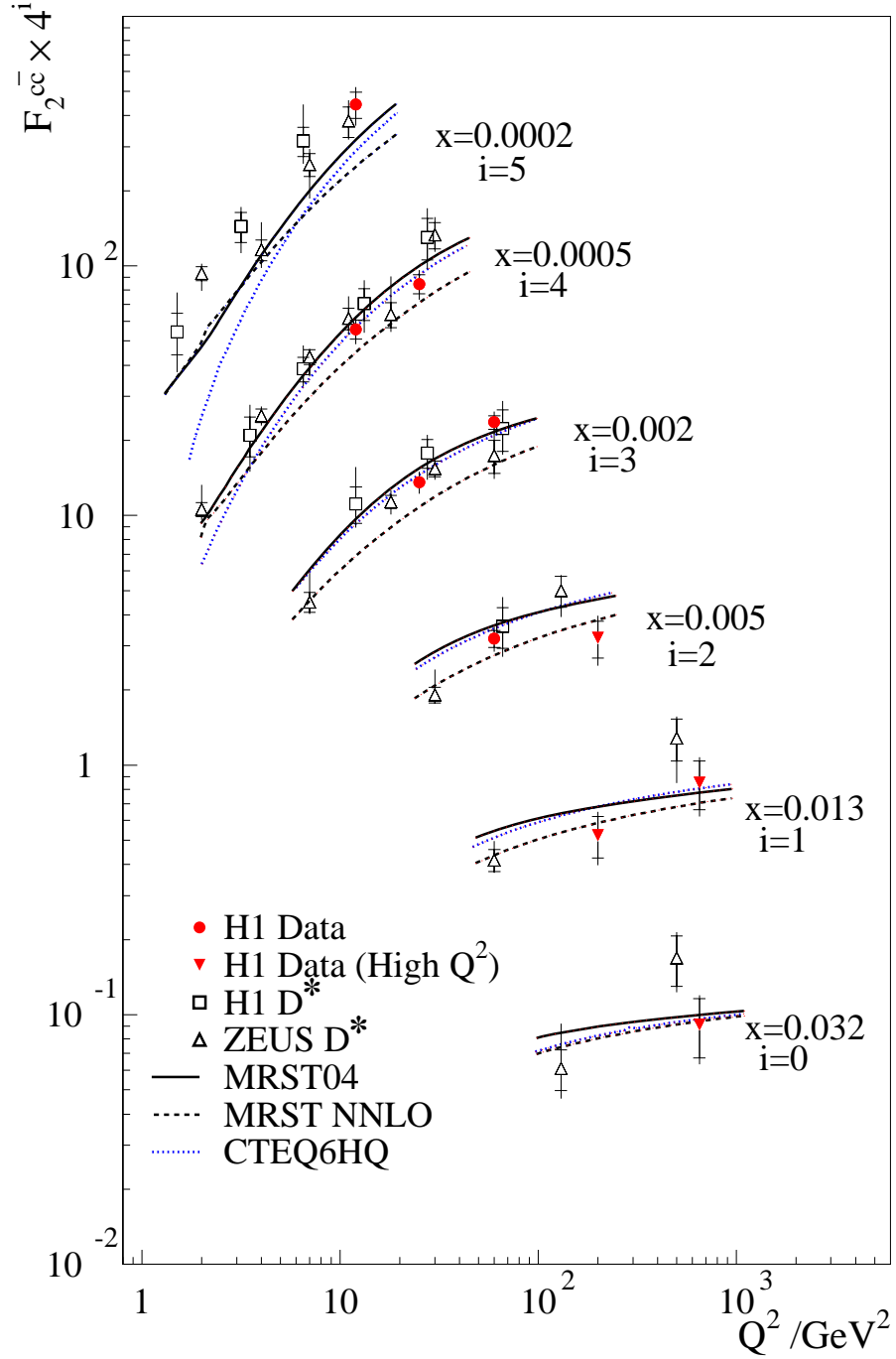


Figure 67: $F_2^{c\bar{c}}$ results as a function of Q^2 for various x values, from the H1 inclusive lifetime tagging analyses [54, 75] (shown as full circles and full triangles). The results from the H1 and ZEUS D^{*+} analyses [77, 80, 92] are also shown. The data are compared to different mixed scheme predictions, the NLO calculations from CTEQ [27] and MRST [28], and the first NNLO calculation, as provided by MRST [29].

5.8.3 $F_2^{b\bar{b}}$ results

In this subsection the contributions from beauty events to the inclusive ep scattering are discussed, as expressed by the structure function $F_2^{b\bar{b}}$. Figure 68 shows the $F_2^{b\bar{b}}$ results, from the H1 analyses [54, 75], based on inclusive lifetime tagging. These

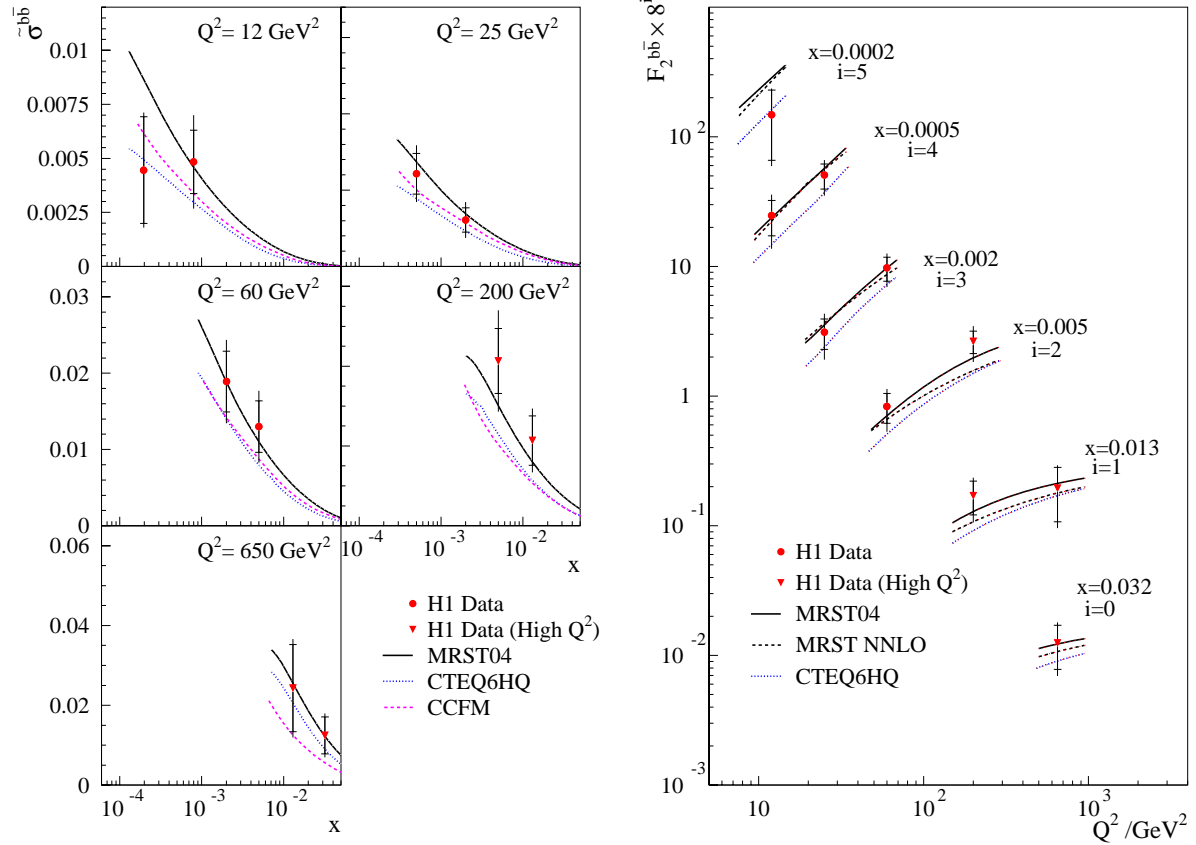


Figure 68: First measurements of the beauty contribution $F_2^{b\bar{b}}$ to the inclusive structure function F_2 , from the H1 inclusive lifetime tagging analyses [54, 75]. The plot on the left shows the reduced cross sections $\tilde{\sigma}^{b\bar{b}}$ as a function of x for different Q^2 . The plot on the right depicts $F_2^{b\bar{b}}$ as a function of Q^2 for various x . The data are compared to mixed scheme NLO calculations from CTEQ [27] and MRST [28], in the right plot also to NNLO predictions from MRST [29].

are the first measurements of $F_2^{b\bar{b}}$. On the left the reduced beauty cross sections $\tilde{\sigma}^{b\bar{b}}$ are shown (equation 16) as a function of x for different Q^2 . Similarly as for charm, the reduced cross section rises towards smaller x and larger Q^2 . On the right the $F_2^{b\bar{b}}$ measurements are shown as a function of Q^2 for various x . Large positive scaling violations are observed. The data are compared to mixed scheme NLO calculations from CTEQ [27] and MRST [28]. Large differences are observed between the two calculations which reach a factor two at the lowest Q^2 and x . These variations arise mainly from the different treatments of threshold effects by MRST and CTEQ. However, within

the current experimental errors, these differences cannot yet be resolved: both calculations describe the data well. On the right in figure 68 the data are also compared to the mixed scheme NNLO predictions from MRST [29]. As for charm, the NNLO calculation is lower than the NLO prediction from the same group. The differences are somewhat smaller than for charm, but still reach values up to 30% e.g. at $x = 0.006$. The data are also well described by NNLO.

Figure 69 shows the fractional contributions of charm and beauty events to deep inelastic ep scattering as expressed by the ratios $f^{c\bar{c}} = F_2^{c\bar{c}} / F_2$ and $f^{b\bar{b}} = F_2^{b\bar{b}} / F_2$. The results from the H1 inclusive lifetime tagging analyses [54, 75] are presented as a function of Q^2 in bins of x . In the probed kinematic region the charm fractional contribution is fairly flat with values of 20–30%. On the contrary the beauty contributions is strongly rising from a few permille at small $Q^2 = 12 \text{ GeV}^2 < m_b^2$ to about 3% at the largest $Q^2 = 500 \text{ GeV}^2 \gg m_b^2$. This reflects clearly the kinematic threshold behaviour: at small Q^2 and x the available invariant mass of the gluon-photon system can barely exceed the minimal required mass of $2m_b$. At larger Q^2 the mass effects become less important and the beauty fraction slowly approaches the 'flavour democratic limit' value of $1/11$. In figure 69 also the MRST NLO prediction [28] is shown, which gives a good description of both the charm and the beauty data.

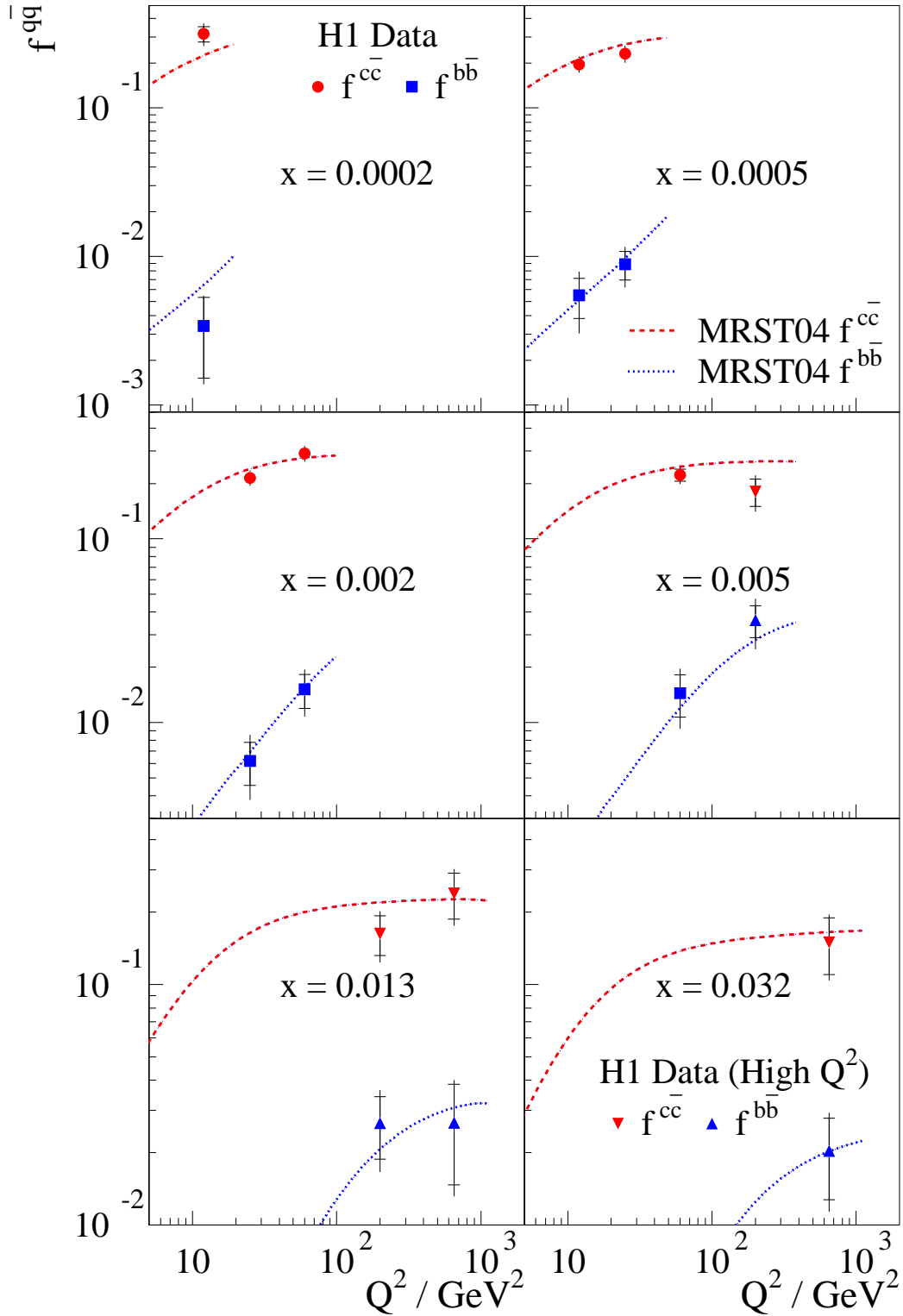


Figure 69: Relative charm and beauty contributions to the total DIS cross section $f^{cc} = F_2^{cc} / F_2$ and $f^{bb} = F_2^{bb} / F_2$, shown as a function of Q^2 for six different x values, from the H1 analyses [54, 75]. A mixed scheme NLO prediction from MRST [28] is also shown.

5.8.4 Direct determination of the proton gluon density with D^{*+} data

The inclusive D^{*+} data in DIS and in photoproduction can be used for a direct determination of the proton gluon density. This has been done in the older H1 measurement [81] with the relatively small data sample available at the time. The proton momentum fraction carried by the gluon can be approximately calculated, assuming the leading order PGF process (figure 9), from the kinematics of the D^{*+} and the photon and furthermore assuming that the gluon is collinear with the proton. The gluon density is iteratively unfolded with the help of the massive scheme NLO calculation [22]. It is assumed that NLO describes the data correctly and that the proton gluon density is the only unknown in the calculation. The results are shown in figure 70. All results are

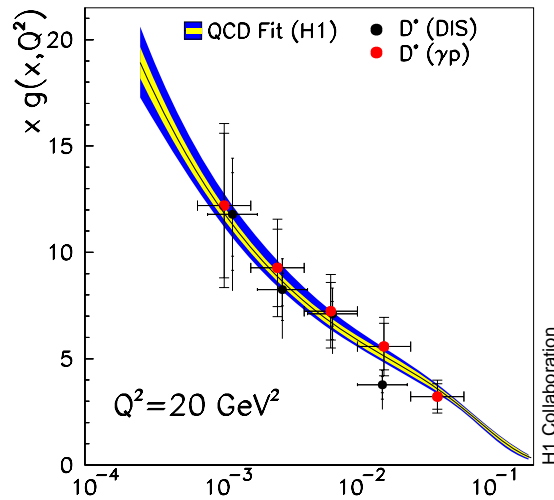


Figure 70: Proton gluon density as a function of the proton momentum fraction carried by the gluon, at a factorisation scale $Q^2 = 20 \text{ GeV}^2$. The points with the error bars show the results from the direct determination with charm events using D^{*+} measurements in DIS and photoproduction, from the H1 analysis [81]. For comparison the gluon density as determined from the scaling violations of the inclusive structure function F_2 [5] is also presented (shaded band).

evolved with the DGLAP parton evolution to an effective hard scale $Q^2 = 20 \text{ GeV}^2$. The D^{*+} data cover a range of proton momentum fractions from 10^{-3} to a few 10^{-2} . The results in photoproduction and in DIS agree with each other and also with the gluon density as determined from the scaling violations of the inclusive structure function F_2 [5]. This is another confirmation of the QCD hard scattering factorisation theorem. It would be nice to repeat this analysis with the complete HERA I sample or/and with the new HERA II data.

5.9 Charm fragmentation issues

This subsection discusses charm fragmentation at HERA. The main question is: Is charm fragmentation universal, i.e. is it the same in ep as in e^+e^- collisions? The

following fragmentation aspects are studied at HERA:

- The fragmentation function, i.e. the longitudinal charm quark momentum fraction the charm hadrons obtain in the fragmentation process.
- The fragmentation ratios into the different hadron species D^{*+} , D_s , D^0 , D^+ and λ_c .
- The production of orbital L=1 or radial excited states and the search for new charmed states.

The results are briefly discussed in the following.

Charm Fragmentation function: The charm fragmentation function is studied with D^{*+} mesons in DIS in the H1 analysis [94] and in photoproduction in the ZEUS measurement [95]. Two complementary techniques are applied:

1. **The jet method:** In addition to the D^{*+} an associated jet is selected and a fragmentation sensitive observable z_{jet} is defined as

$$z_{jet} = \frac{(E + p_L)_{D^{*+}}}{(E + p)_{jet}}, \quad (17)$$

where p_L is the momentum of the D^{*+} parallel to the jet direction. This observable is studied both in [94] and [95].

2. **The hemisphere method:** The event is divided into two hemispheres. One contains the D^{*+} and other particles from the fragmentation of the D^{*+} mother charm quark. The other hemisphere contains the anticharm quark. The fragmentation observable is constructed as

$$z_{hem} = \frac{(E + p_L)_{D^{*+}}}{\sum_{hem} (E + p)}. \quad (18)$$

In the denominator the energies and three momenta of all particles in the D^{*+} hemisphere are summed. This observable is studied in [94].

The ZEUS results with the jet method are shown in figure 71. The data are compared to PYTHIA [25] predictions using the PYTHIA default Symmetric Lund-Bowler fragmentation function (right) and the Peterson [23] function (left), with three different parameter settings. The data are highly sensitive to these settings. In figure 72 the H1 findings with the hemisphere method are presented and compared to e^+e^- results at different centre-of-mass-energies \sqrt{s} . The average \sqrt{s} probed at H1 data is roughly comparable to that at CLEO. The H1 results are shifted towards higher z compared to the e^+e^- data.

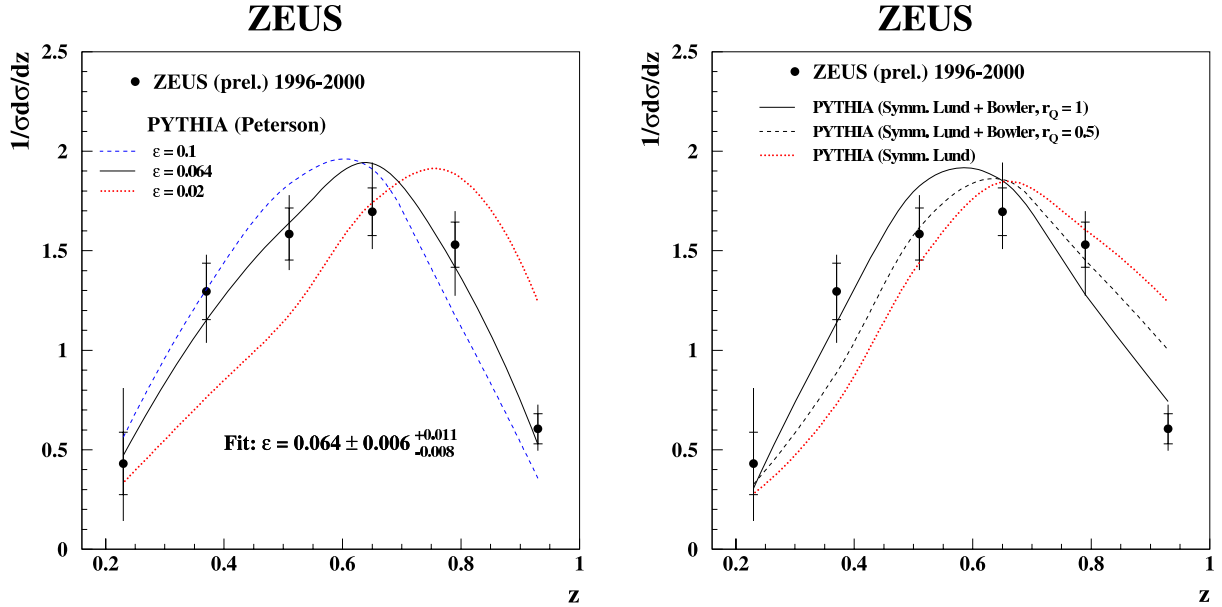


Figure 71: Fragmentation function vs z_{jet} for the ZEUS D^{*+} photoproduction analysis [95], compared to PYTHIA predictions with using the Peterson fragmentation function (left) and the Symmetric-Lund-Bowler function (right), each with three different parameter settings.

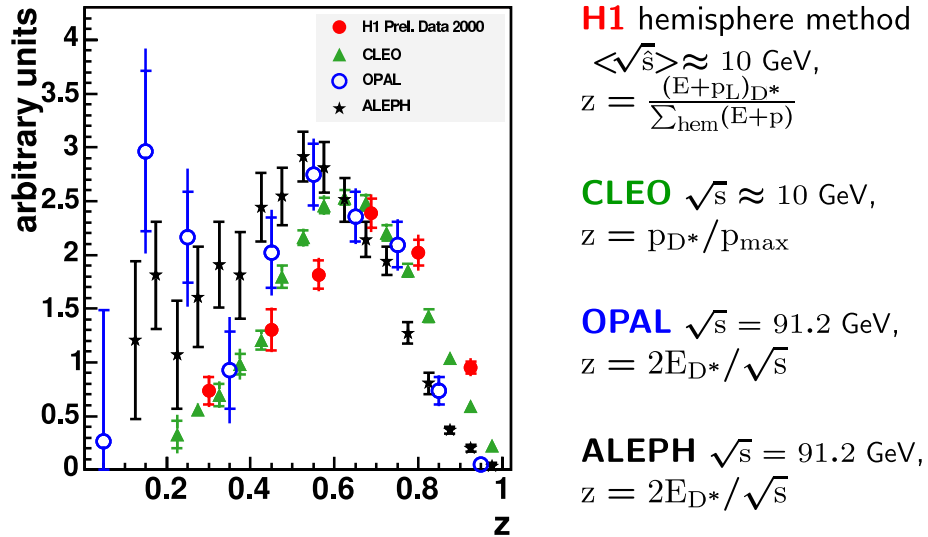


Figure 72: Comparison of D^{*+} z -distributions from CLEO, OPAL and ALEPH with the results from the H1 analysis [94] obtained with the hemisphere method in DIS events. All distributions are normalised to unit area from $z = 0.4$ to $z = 1$.

Charm fragmentation ratios: Figure 73 illustrates the charm fragmentation fractions into the different hadron species as observed in e^+e^- collisions at LEP. For HERA H1 and ZEUS have measured [48, 82, 96] the fragmentation fractions for D^{*+} , D_s , D^0 , D^+ and λ_c using fully reconstructed decays, both in photoproduction and in DIS. The results

are shown in figure 74. Good agreement is observed with the LEP results supporting the assumption of fragmentation universality.

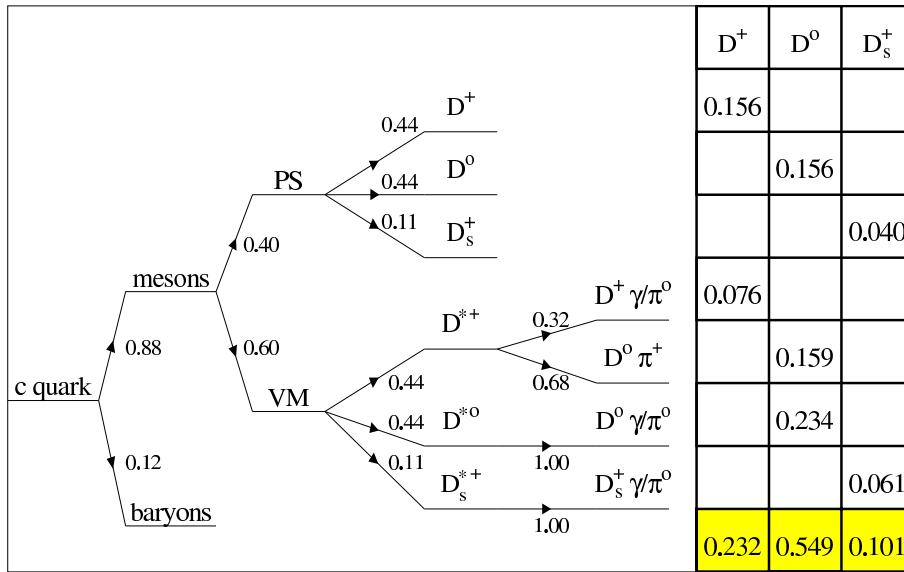


Figure 73: Illustration of the charm fragmentation ratios into different hadron species. The numbers are from e^+e^- collisions at LEP.

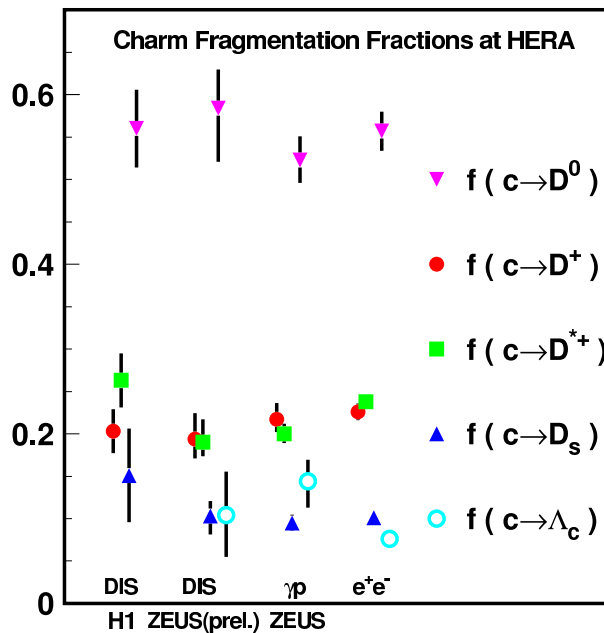


Figure 74: Charm fragmentation ratios observed at HERA compared to the results from e^+e^- collisions at LEP.

Orbital and radial excitations: ZEUS has measured in [97, 98] the fragmentation fractions of the known L=1 orbital excitations D_1^0 , D_2^{*0} and D_{s1}^+ . The results are shown

	$f(c \rightarrow D_1^0)$ [%]	$f(c \rightarrow D_2^{*0})$ [%]	$f(c \rightarrow D_{s1}^+)$ [%]
ZEUS (prel.)	$1.46 \pm 0.18^{+0.33}_{-0.27} \pm 0.06$	$2.00 \pm 0.58^{+1.40}_{-0.48} \pm 0.41$	$1.24 \pm 0.18^{+0.08}_{-0.06} \pm 0.14$
CLEO	1.8 ± 0.3	1.9 ± 0.3	
OPAL	2.1 ± 0.8	5.2 ± 2.6	$1.6 \pm 0.4 \pm 0.3$
ALEPH	1.6 ± 0.5	4.7 ± 1.0	$0.94 \pm 0.22 \pm 0.07$
DELPHI	1.9 ± 0.4	4.7 ± 1.3	

Table 9: Fragmentation fractions of $L=1$ orbital excited D meson states.

in table 9 and in general agree with the e^+e^- values. The situation for the D_2^{*0} is not so clear, since at LEP much larger fragmentation fractions are observed than seen by CLEO or ZEUS. ZEUS has searched in [97] for a radial excitation $D^{*\prime\pm}$, where evidence for an observation was claimed by DELPHI at a mass ~ 2.63 GeV. No signal is found in the ZEUS data.

New resonances: H1 has observed [99] a candidate for a charmed pentaquark resonance $|uud\bar{c}d\rangle$ with a mass of 3.1 GeV decaying into a proton and a D^{*-} meson. This signal was not confirmed by ZEUS [50]. The HERA II data with their expected much larger statistics will reveal if the H1 events were caused by a real signal or by a statistical fluctuation.

6 HERA II

With the HERA I data one has achieved many important key measurements of heavy flavour production in high energy ep collisions. The currently ongoing HERA II data taking will allow to continue investigations in this field with much higher precision. The instantaneous luminosity was increased for HERA II by a factor of ~ 3 . This was reached by installing new focusing magnets near the interaction points. The HERA II data taking started in 2003 and will finish in summer 2007, the end of HERA. The integrated luminosities taken so far by H1 and ZEUS (October 2005) are $\sim 150 \text{ pb}^{-1}$. These data are currently being analysed. Further $\sim 250 \text{ pb}^{-1}$ are expected for the remaining period. Thus at the end of HERA II the newly accumulated statistics will be roughly a factor five higher compared to HERA I. For HERA II the electron beam is polarized, which is relevant for Z^0 and W exchanges at high Q^2 but not for the largest part of heavy flavour physics with photon exchange at lower Q^2 . The H1 and ZEUS detectors have been substantially upgraded for the HERA II running period. This is discussed in the following and thereafter the heavy flavour physics goals and reach of the HERA II project.

6.1 Detector upgrades for HERA II

Dedicated detector upgrades³ have been undertaken by H1 and ZEUS for heavy flavour physics with HERA II. The upgrades are mainly in the area of charged tracking with silicon detectors, forward detectors and track based triggers, as briefly discussed in the following:

- **Silicon detectors:** ZEUS has for the first time installed a silicon tracker, the MVD, shown in figure 75. This detector consists of a 60 cm long barrel part

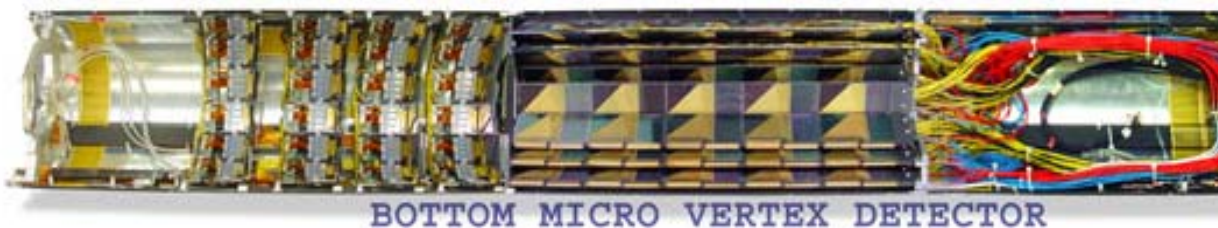


Figure 75: Sketch of the ZEUS Micro Vertex Detector (MVD) installed for the HERA II data taking period.

of two to three layers silicon sensors and four wheel detectors in the forward direction, providing angular coverage for pseudorapidities up to $\eta = 2.6$. A similar forward reach is provided by the new H1 Forward Silicon Tracker (FST), which

³Detailed information and references can be found on the H1 and ZEUS webpages.

complements the Central Silicon Tracker (CST). The H1 backward silicon tracker (BST) extends the coverage for 3d-track measurements in the backward region to $\eta = -2.8$.

- **Forward track detectors:** ZEUS has implemented two new modules of Straw Tube Trackers, interleaved with the existing three sets of planar drift chamber modules. H1 has installed five new planar drift chambers.
- **Track based triggers:** The H1 Fast Track Trigger (FTT) is a major upgrade system for triggering of heavy heavy flavour events on the basis of charged decay tracks. This trigger makes use of in total 12 wire layers of the central jet chambers. Trigger information on track multiplicities and transverse momenta is available at trigger level 1 (within $2.3 \mu\text{s}$), this information is refined at level 2 (within $23 \mu\text{s}$) e.g. adding z information. On level 3 full reconstruction of charm decays is provided, e.g. for the golden D^{*+} decay channel (within $100 \mu\text{s}$). A main goal is to facilitate the triggering of charm and beauty photoproduction events, where the scattered electron remains untagged in the beam pipe. ZEUS has implemented a new second level trigger using information from the MVD, the central drift chambers and the new forward straw tube tracker.

	Photoprod. $Q^2 \approx 0$	DIS low Q^2	DIS $Q^2 \geq 150 \text{ GeV}^2$
Charm: D^{*+} incl. lifetime tag	15000 Trigger?	15000 60000	250 1000
Beauty: Muon+jet incl. lifetime tag	600 Trigger?	300 300	unclear 200

Table 10: Expected number of background free equivalent events per experiment at the end of HERA II for selected 'flagship' charm and beauty tagging channels, for three regions of photon virtuality Q^2 . The results are obtained by a simple scaling of HERA I event numbers by a factor five. For the entries 'Trigger?' it would need to be clarified how these events are triggered.

6.2 Physics goals and reach with HERA II

In the following it is assumed that one will collect with HERA II until summer 2007 a five times larger sample than that available from HERA I. Furthermore it is assumed that the systematic uncertainties of the measurements decrease in parallel with the statistical errors. Table 10 lists the expected numbers of background free equivalent events for the 'flagship' tagging methods for charm and beauty for three regions of photon virtuality Q^2 . The same tagging efficiencies are assumed as achieved for HERA I. From these numbers it is clear that for beauty an important qualitative step can be done from the HERA I measurements, that were often barely significant in single bins, to HERA II, where precisions of $\leq 20\%$ ($\leq 10\%$) can be expected for differential (total) measurements, including systematic errors. For charm the differential measurements were already often at the $\leq 10\%$ level precision for HERA I. Here the statistics increase can be exploited for more differential measurements, e.g. double or triple differential, and measuring at higher photon virtualities Q^2 and larger transverse charm quark momenta than before. In the following the expected impact of higher statistics and upgraded detectors is discussed in detail for the different heavy flavour physics issues:

- **Structure function $F_2^{c\bar{c}}$ and the proton gluon density:**

Already the HERA I $F_2^{c\bar{c}}$ structure function measurements from H1 and ZEUS were used in recent proton PDF-fits such as CTEQ6H due to their sensitivity to the charm and gluon distributions. With the increased HERA II statistics this will become more important, because the determination of the PDFs from inclusive ep scattering or with jets is already now often systematically limited, both from the experimental and the theoretical side, while the charm results are still limited from the data statistics. Thus these measurements are a key task for

the HERA II heavy flavour program. Due to the detector upgrades the $F_2^{c\bar{c}}$ and $F_2^{b\bar{b}}$ measurements can be performed in an extended kinematic range. This is illustrated in figure 76 which shows the H1 detector acceptance for charm quarks tagged with the golden D^{*+} decay channel as a function of Bjorken x for two Q^2 ranges. The results are from a Monte Carlo simulation. With the new forward (backward) silicon detectors FST (BST) the acceptance is extended to x values as high (low) as $3 \cdot 10^{-1}$ (10^{-5}). This will allow the first measurements of charm production for high $x > 0.03$ at Q^2 values much larger compared to previous fixed targeted experiments. A direct measurement of the gluon density with using charm events will be possible over a large range of proton momentum fractions carried by the gluon.

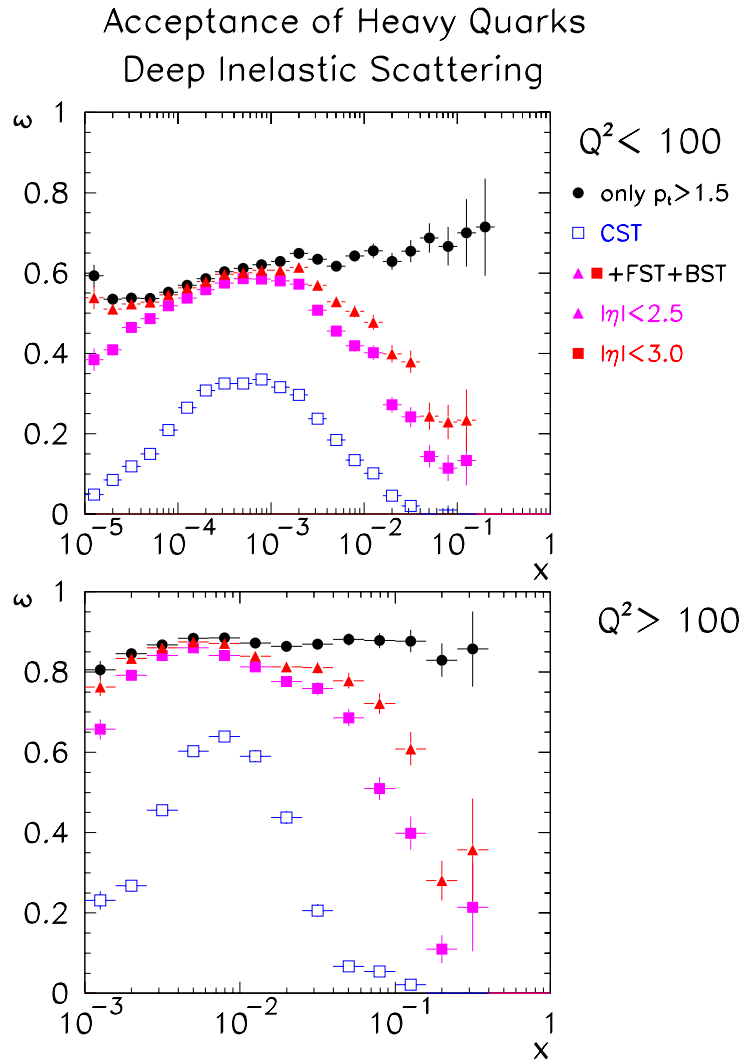


Figure 76: H1 detector acceptance for charm events ($ep \rightarrow D^{*+} X \rightarrow K\pi\pi_s + X$) using the central tracker and the central silicon tracker CST (open points) and adding the forward (backward) silicon trackers FST (BST) with different assumptions on the acceptance range η of the D^{*+} , taken from the FST upgrade proposal document, available on the H1 web pages.

- **Structure function $F_2^{b\bar{b}}$ and $b\bar{b} \rightarrow H$ at LHC:**

The HERA I measurements of the beauty contribution $F_2^{b\bar{b}}$ to the inclusive structure function F_2 have large errors due to the small available statistics. A statistical improvement by a factor ~ 10 can be expected from HERA II, adding H1 and ZEUS together, resulting in total errors $\leq 20\%$. This will be very useful for comparing with the various NLO calculations in the massive and mixed schemes that predict up to a factor two different results. A further possible application of these measurements was discussed by Maltoni at the recent HERA-LHC workshop. In the massless scheme the leading order contribution to $F_2^{b\bar{b}}$ is the QPM process (figure 6 left). In this picture $F_2^{b\bar{b}}$ is directly proportional to the beauty quark density in the proton. This density measured at HERA at the scale $Q = 30$ GeV can be directly used for predicting Higgs production in pp collisions at the LHC in the channel $b\bar{b} \rightarrow H$, where the relevant scale is $m_H/4 = 30$ GeV, assuming a Higgs mass of 120 GeV. This channel is expected to contribute up to 4% of the total Higgs production cross section at the LHC.

- **Tests of higher order effects with inclusive D^{*+} measurements:**

Single differential D^{*+} cross sections have been already measured quite accurately at HERA I both in photoproduction and in DIS. The theory uncertainties are often much larger than the data errors. Thus here is a field, where mainly the predictions need to be improved e.g. with NNLO calculations or with more precise parameter values such as for the charm quark mass. For the data the main progress could come with the following phase space extensions:

- To forward pseudorapidities $\eta > 1.5$ utilising the upgraded forward trackers.
- To the highest transverse momenta $p_T > 30$ GeV and photon virtualities $Q^2 > 1000$ GeV² exploiting the increased data statistics.
- To lower transverse momenta with other D -meson decays than the golden D^{*+} channel. This may necessitate to set up dedicated triggers, which directly select such decay channels.

Such extensions are highly interesting, because in the new phase space regions the sensitivity for distinguishing between different models and for determining theory parameters is often increased.

- **Charm production mechanism studies:**

With HERA I one has verified with D^{*+} measurements (figure 41) that in DIS for moderate photon virtualities $Q^2 > 10$ GeV² the dominant charm production mechanism is the photon gluon fusion process. It would be highly interesting to investigate for higher Q^2 the expected transition to the 'QPM scattering regime' i.e. from the massive to the massless regime. For this one would need to study with the D^{*+} sample the cross section as a function of the photon energy fraction transferred to the D^{*+} in the proton restframe in bins of Q^2 as expressed by the observable $z_{D^{*+}}$. An alternative method is to tag a charm jet with the inclusive lifetime method and to investigate other jets in the event. In photoproduction the

charm production mechanism was studied in detail with the HERA I data using events with a D^{*+} and one or two jets. Indications were found for large contributions from resolved photon processes with charm flavour excitation in the photon. For HERA II this can be investigated further in detail by more differential studies. One possibility is the double tagging of charm events with two fully reconstructed D mesons which should become feasible at HERA II. However, this will crucially depend on the triggering. Perhaps it is possible to directly trigger with the new track triggers on two fully reconstructed D mesons for transverse momenta down to ~ 2 GeV. The detector extensions to the more forward direction are a further crucial element for clarifying the charm production mechanism, since in this region the largest differences are expected between models with and without a charm component in the resolved photon.

- **Parton dynamics studies**

The HERA I inclusive flavour data have revealed important insights for the understanding of the low Bjorken $x \sim 10^{-4}$ domain in DIS. Deviations from the standard DGLAP parton evolution approach have been observed in analyses with forward particles and jets. For charm, only inclusive D^{*+} analyses are available in DIS at low x , which have not been particularly revealing for the question of the dynamics of multi gluon emission in the proton. However, the nice feature of charm events is that the charm tag automatically identifies a quark. This knowledge drastically restricts the possible feynman diagrams and can help in the understanding of the parton dynamics. For this one ideally would select in addition to the charm quark a jet which can be in the more forward direction and which can represent a gluon from the emission cascade (recall figure 8). Significant results should be obtainable with the HERA II data statistics.

- **Photon structure:**

The main question is how much charm contributes as an active parton to the resolved photon structure and vice versa how large are the contributions from resolved photon events to charm production? The main difficulty is that these questions are highly ambiguous in Next to Leading Order pQCD. Given the large general uncertainties of the charm photoproduction calculations, the question of resolved photon structure will remain a very difficult one. For HERA II a significant progress could be expected from the increased acceptance for charm measurements in the more forward directions, where the largest contributions from resolved photon contributions are expected. Investigations of the resolved photon component in DIS as a function of Q^2 can be also pursued with the increased data statistics.

- **Charm fragmentation studies:**

The charm fragmentation studies should be continued at HERA II with higher precision. The fragmentation parameters can be investigated at HERA as a function of the energy and the direction of the charm quark.

- **Determination of charm quark mass**

The perturbative uncertainties for charm production in DIS are small. This could be exploited to constrain the charm quark mass, which strongly influences the normalisation of the data, mainly at low transverse momenta.

- **Studies of beauty production:**

The at HERA II available statistics for beauty differential production measurements e.g. for analyses with muons and jets will suffice to investigate in more detail higher order effects and the production mechanisms in photoproduction and in DIS. It will remain very difficult to obtain significant results on the beauty fragmentation since only small samples of fully reconstructed B mesons will be available.

Further ideas: A few ideas are discussed here, which are not belonging to the 'main stream topics' of heavy flavour production at HERA:

- **Access to strange sea quarks in the proton with charm in charged current events:**

At high Q^2 charm quarks can be produced at HERA in charged current interactions

$$W^+ s \rightarrow c. \quad (19)$$

Such measurements of charm production could reveal important information on the s quark density in the proton, which is so far mainly known from dimuon events in neutrino scattering experiments (NUTEV, CCFR) but with rather moderate precision. The cross section for the reaction (19) was estimated in the Future Physics at HERA workshop to be ~ 5 pb for $Q^2 > 200$ GeV² with an uncertainty of about 50%. Thus with 250 pb⁻¹ integrated luminosity at HERA II about 1250 events can be expected. Assuming similar charm tagging efficiencies (10%) and signal to background ratios (1:12) as that achieved with the inclusive lifetime method in the $F_2^{c\bar{c}}$ and $F_2^{b\bar{b}}$ measurement at high Q^2 [54], the final charm event yield will be $\sim 125 \pm 40$ events. Thus in total a 3σ significant measurement can be achieved, which is not particularly promising.

- **Intrinsic charm measurement:**

There are since long speculations about an intrinsic charm component in the proton wave function, where the charm quarks carry a large momentum fraction $x > 0.2$. However, the expected effects are very small and the charm quarks are flying in the very forward direction, where the experimental acceptances are low

- **Beauty tag for BSM searches.**

There has been an excess observed in the H1 data for events with an isolated high p_T lepton and large missing momentum. These events have been analysed in the context of single top production from new physics beyond the standard model. The top decays into a b and a W . For the HERA II data with the increased

statistics and better silicon tracker coverage in the more forward region one could try to identify the b quark via its lifetime signature, which in this case is rather spectacular since the b quark would have a typical transverse momentum of ≥ 50 GeV and hence would decay after ~ 5 mm decay length. In general lifetime tags for beauty could be used for searching for new physics since in many scenarios more beauty quarks are expected than from standard model processes.

7 Summary

The study of heavy flavour production in high energy ep collisions at HERA offers a testing ground par excellence for the strongest known force in nature, quantum chromodynamics (QCD). The main production mechanism is $\gamma g \rightarrow c\bar{c}, b\bar{b}$, where the photon is emitted from the electron and the gluon from the proton. This combination of a clean electromagnetic probe as provided by the photon and a strongly interacting gluon allows to investigate the strong force in great detail. The large masses of the charm and beauty quarks provide hard scales, that make perturbative QCD (pQCD) applicable. There can be other hard scales present, the photon virtuality Q^2 or the transverse momenta p_T of the outgoing heavy quarks. This leads to the inherent multi-hard-scale problem in pQCD – terms in the perturbation series of the form $\sim [\alpha_s \log(Q^2/m_c)]^n$ to all order n that can become large and spoil the convergence of the series. There are basically two competing approximations: the massive scheme calculations, which follow a rigorous field theory approach for massive particles, and the massless scheme calculations, which neglect the heavy quark masses in the kinematics of the process. There are also mixed schemes, which interpolate between the two.

At HERA the multi-scale problem can be uniquely tested over a wide kinematical range $0 < Q^2 < 1000 \text{ GeV}^2$ and $0 < p_T < 30 \text{ GeV}$ for both charm and beauty. The two experiments H1 and ZEUS have collected during the 1992-2000 HERA I data period total charm samples of the order of ~ 10000 background free equivalent events, mainly with the D^{*+} golden decay channel. Beauty is heavily phase space suppressed at HERA due to the large b quark mass of $\sim 5 \text{ GeV}$; the tagged beauty samples, e.g. with muons, consist of the order of a few hundred background free equivalent events. In the last years HERA has seen the advent of heavy quark tagging based on the relatively long lifetime of charm and beauty quarks, utilising the high precision reconstruction of charged decay tracks as provided by a silicon detector. These measurements yield by now the statistically most accurate charm and beauty results.

The measured charm and beauty production cross sections fall from the smallest to the largest Q^2 and p_T values over several orders of magnitude. Overall, the Next to Leading Order (NLO) calculations in the massive scheme describe the charm and beauty data for all this kinematic range reasonably well, within a factor of two. However, in certain phase space regions larger discrepancies are observed. For charm photoproduction ($Q^2 \approx 0$) the D^{*+} cross sections exceed the calculations for low transverse momenta and in the more forward, or proton direction. Prominent excesses are observed in events with a D^{*+} and two jets, if the jets are very forward. These data are much better described by Leading Order Monte Carlo simulations in the massless scheme which contain a large flavour excitation component, where the charm quark originates from a hadronic fluctuation of the photon that takes place before the hard interaction with the proton. If one believes more in the rigorous approach of the massive calculation, then the excesses must be attributed to higher order NNLO corrections. In general the massless NLO calculations, where available, do not give a better description of the charm photoproduction data. Moreover, both for massive and massless

NLO calculations, the estimated perturbative uncertainties are large at small p_T , where they exceed a factor of two. The situation improves drastically for charm production in DIS ($Q^2 > 1 \text{ GeV}^2$) due to the additional hard Q^2 scale. Thus it is not a surprise that here the massive scheme NLO calculations provide a good description of differential D^{*+} cross sections as functions of Q^2 and the D^{*+} transverse momentum and pseudorapidity.

For beauty both in photoproduction and in DIS the measured cross sections are often somewhat higher than the massive scheme NLO predictions. This is a surprise, since it can be expected, that the large b mass leads to a particular good control of pQCD. The largest discrepancies are seen for small transverse momenta below the b quark mass, where the data are factors of two to four higher than the predictions. Some excesses are also seen in the more forward direction, while there is no clear trend as a function of the photon virtuality Q^2 . For measurements with events with a muon and two jets there are some experimental discrepancies between the H1 and ZEUS results that need to be clarified in the future.

Besides the comparisons with NLO predictions investigations have been performed of the role of charm and beauty events for the inclusive ep scattering, as expressed by the structure functions $F_2^{c\bar{c}}$ and $F_2^{b\bar{b}}$. As a result in the covered kinematic region charm contributes up to 30% to the flavour inclusive scattering and beauty up to 3%. The highest fractions are reached for large Q^2 and small Bjorken x . For these measurements an experimental breakthrough has been recently achieved with the inclusive lifetime tagging analyses. Due to the inclusiveness of the selection, i.e. only one track is required with $p_T > 0.5 \text{ GeV}$, the kinematic acceptance for charm and beauty quarks is very high, e.g. at large $Q^2 > 150 \text{ GeV}^2$ above 90%. This is much better than that for previous D^{*+} analyses, where the kinematic acceptances are below 50%. The $F_2^{c\bar{c}}$ results at HERA cover a large range $2 < Q^2 < 1000 \text{ GeV}^2$ and Bjorken x from ~ 0.00003 to ~ 0.03 . The results are in agreement with the massive NLO predictions, which use gluon densities determined mainly from the scaling violations of the flavour inclusive structure function F_2 . This is a nice confirmation of the QCD hard scattering theorem which states that the gluon density is universal for different hard processes. The HERA $F_2^{c\bar{c}}$ results have been already used in recent proton pdf fits from CTEQ (CTEQ6HQ) as an additional constraint on the gluon density, which indicates the high importance of these measurements. Furthermore, for the mixed schemes, they are very sensitive to the implementation of the transition from the massive to the massless regime, where predictions from MRST and CTEQ differ by large factors for small Q^2 values near m_c^2 . With the inclusive lifetime tagging the first measurements have been recently obtained on the structure function $F_2^{b\bar{b}}$. There are large differences of the order of factor two between the massive scheme and different mixed scheme predictions. However, the current statistical errors of the measurements ($\sim 50\%$) do not yet allow to separate between these predictions and the data are well described by all the calculations.

Two further topics are investigated at HERA I with charm and beauty: The first is the question of deviations from the standard DGLAP parton evolution in the proton.

Unlike DGLAP the CCFM evolution predicts a sizable non zero transverse momentum for the gluon which enters the photon gluon fusion process. However, for this question the experimental heavy flavour results from HERA I were not yet particularly revealing. This is on one hand due to experimental reasons, since these problems can be tested best with more than one tagged hard parton in the event, and the available charm and beauty samples are very small. On the other hand the only so far available theoretical implementation of CCFM, the CASCADE program, is lacking prediction power, since it is only a Leading Order calculation and fails in many cases to describe the heavy flavour and other HERA data. Hence, this topic was not investigated in detail in this essay. The second topic is the charm fragmentation. The main motivation is to test the universality of the charm fragmentation results obtained in e^+e^- collisions, which is usually assumed in calculations. The HERA results for the fragmentation fractions into different charm hadron species do clearly support this universality hypothesis, while the situation for the fragmentation hardness is not so clear.

A bright future can be foreseen for HERA heavy flavour physics. The currently ongoing HERA II data taking will collect until summer 2007 at least five times more statistics than HERA I. The detectors have been upgraded specifically for heavy flavour purposes: there are now silicon detectors all over the place, the forward tracking detectors have been improved and there are new track based triggers. This will allow to investigate all the above raised physics questions in more detail in an extended kinematic phase space as discussed in section 6. For beauty, HERA II will bring a qualitative step towards measurement with precision in the order of 10% for the total cross sections and 20% for differential cross sections. This will for sure help to clarify the situation with respect to NLO calculations and to resolve some experimental discrepancies. For charm at HERA I has already passed the precision from theory predictions in many cases. Especially for the DIS regime, the analysis of the HERA I charm data could be further exploited. Here the theory perturbative errors are reasonably small and the data could be used in global fits to constrain the non perturbative parameters as the charm quark mass.

For theory improvements there is a general problem: Rigorous NNLO calculations for the massive scheme will not be available in the next years. This is due to missing master integrals for higher order loop diagrams with heavy quark lines. This could lead to an asymmetry in the quality of theory predictions for light and heavy quarks, since the NNLO developments for light quarks are well under way. Despite this, there can be also important theory improvements foreseen, in the area of the mixed scheme NNLO calculations and in the development of the MC@NLO Monte Carlo simulation program, where massive NLO calculations at the parton level are combined with matched parton showers and fragmentation.

Finally a short excursion is made to the LHC. Recently the impact of the HERA physics on LHC has been discussed in the HERA-LHC workshop. A dedicated working group has addressed heavy flavour issues and a written workshop summary document will be soon available. The dominant production mechanism for heavy quarks

at the LHC is the gluon gluon fusion process. Thus a main ingredient from HERA is the knowledge of the proton gluon density, where the relevant range for the proton momentum fraction carried by the gluon is at LHC roughly one order of magnitude lower than at HERA, due to the seven times larger proton energy at the LHC. The physics which can be tested with beauty quarks at LHC is usually regarded as being of higher importance than that with charm quarks. As stated by e.g. Nason the uncertainty of the beauty production at the LHC is not dominated by the knowledge of the gluon density from HERA, but from perturbative aspects, i.e. higher order effects. In the context of the massless scheme approach a NNLO calculation of the beauty quark density in the proton can be used to predict Higgs production in the channel $b\bar{b} \rightarrow H$, which could account up to a few percent of the total Higgs production cross section. This calculation could be tested at HERA from a measurement of $F_2^{b\bar{b}}$ at high Q^2 , which provides access to the beauty density in the proton at comparable hard scales. Although very high precision will not be possible at HERA, such measurement will for sure be attempted at HERA II.

Acknowledgments

I would like to thank Franz Eisele for his invaluable support. I am deeply indebted to Andreas Meyer for a fantastic teamwork in the last three years. Thanks to Jochen Dingfelder, David South and Roger Wolf for their comments and suggestions to the manuscript.

References

- [1] J. J. Aubert *et al.* [E598 Collaboration], Phys. Rev. Lett. **33**, 1404 (1974).
- [2] J. E. Augustin *et al.* [SLAC-SP-017 Collaboration], Phys. Rev. Lett. **33** (1974) 1406.
- [3] S. W. Herb *et al.*, Phys. Rev. Lett. **39** (1977) 252.
- [4] J. C. Collins, D. E. Soper and G. Sterman, Adv. Ser. Direct. High Energy Phys. **5**, 1 (1988) [hep-ph/0409313].
- [5] C. Adloff *et al.* [H1 Collaboration], Eur. Phys. J. C **21** (2001) 33 [hep-ex/0012053].
- [6] S. Frixione, M. L. Mangano, P. Nason and G. Ridolfi, Adv. Ser. Direct. High Energy Phys. **15**, 609 (1998) [hep-ph/9702287].
- [7] E. Laenen, S. Riemersma, J. Smith and W. L. van Neerven, Nucl. Phys. B **392** (1993) 162;

- [8] E. Laenen, S. Riemersma, J. Smith and W. L. van Neerven, Nucl. Phys. B **392** (1993) 229;
- [9] S. Riemersma, J. Smith and W. L. van Neerven, Phys. Lett. B **347** (1995) 143 [hep-ph/9411431].
- [10] B.A. Kniehl, M. Krämer, G. Kramer and M. Spira, Phys. Lett. B **356** (1995) 539 [hep-ph/9505410];
 B.A. Kniehl, G. Kramer and M. Spira, Z. Phys. C **76** (1997) 689 [hep-ph/9610267];
 J. Binnewies, B.A. Kniehl and G. Kramer, Z. Phys. C **76** (1997) 677 [hep-ph/9702408];
 J. Binnewies, B.A. Kniehl and G. Kramer, Phys. Rev. D **58** (1998) 014014 [hep-ph/9712482];
 M. Cacciari and M. Greco, Phys. Rev. D **55** (1997) 7134 [hep-ph/9702389].
- [11] V.N. Gribov and L.N. Lipatov, Yad. Fiz. **15** (1972) 781 [Sov. J. Nucl. Phys. **15** (1972) 438];
 G. Altarelli and G. Parisi, Nucl. Phys. B **126** (1977) 298;
 Y.L. Dokshitzer, Sov. Phys. JETP **46** (1977) 641 [Zh. Eksp. Teor. Fiz. **73** (1977) 1216].
- [12] F. I. Olness and W. K. Tung, Nucl. Phys. B **308** (1988) 813;
- [13] M. A. G. Aivazis, J. C. Collins, F. I. Olness and W. K. Tung, Phys. Rev. D **50** (1994) 3102 [hep-ph/9312319];
- [14] M. A. G. Aivazis, F. I. Olness and W. K. Tung, Phys. Rev. D **50** (1994) 3085 [hep-ph/9312318];
- [15] M. Kramer, F. I. Olness and D. E. Soper, Phys. Rev. D **62** (2000) 096007 [hep-ph/0003035];
- [16] R. S. Thorne and R. G. Roberts, Phys. Rev. D **57** (1998) 6871 [hep-ph/9709442]; Phys. Lett. B **421** (1998) 303 [hep-ph/9711223]; Eur. Phys. J. C **19** (2001) 339 [hep-ph/0010344].
- [17] E. A. Kuraev, L. N. Lipatov and V. S. Fadin, Sov. Phys. JETP **44** (1976) 443 [Zh. Eksp. Teor. Fiz. **71** (1976) 840];
 Sov. Phys. JETP **45** (1977) 199 [Zh. Eksp. Teor. Fiz. **72** (1977) 377];
 Sov. J. Nucl. Phys. **28** (1978) 822 [Yad. Fiz. **28** (1978) 1597];
 Nucl. Phys. B **425** (1994) 471 [hep-ph/9403256].
- [18] M. Ciafaloni, Nucl. Phys. B **296** (1988) 49;
 S. Catani, F. Fiorani and G. Marchesini, Phys. Lett. B **234** (1990) 339;
 S. Catani, F. Fiorani and G. Marchesini, Nucl. Phys. B **336** (1990) 18;
 G. Marchesini, Nucl. Phys. B **445** (1995) 49.

- [19] M. Krämer, Prog. Part. Nucl. Phys. **47** (2001) 141 [hep-ph/0106120].
- [20] N. Brambilla *et al.*, [hep-ph/0412158].
- [21] S. Frixione, P. Nason and G. Ridolfi, Nucl. Phys. B **454** (1995) 3 [hep-ph/9506226].
- [22] B. W. Harris and J. Smith, Nucl. Phys. B **452** (1995) 109 [hep-ph/9503484].
- [23] C. Peterson, D. Schlatter, I. Schmitt and P.M. Zerwas, Phys. Rev. D **27** (1983) 105.
- [24] P. Nason and C. Oleari, Nucl. Phys. B **565** (2000) 245 [hep-ph/9903541].
- [25] T. Sjöstrand, Comput. Phys. Commun. **39** (1986) 347;
T. Sjöstrand and M. Bengtsson, Comput. Phys. Commun. **43** (1987) 367;
T. Sjöstrand *et al.*, Comput. Phys. Commun. **135** (2001) 238 [hep-ph/0010017].
- [26] G. Heinrich and B. A. Kniehl, Phys. Rev. D **70**, 094035 (2004) [hep-ph/0409303].
- [27] S. Kretzer, H. L. Lai, F. I. Olness and W. K. Tung, Phys. Rev. D **69** (2004) 114005 [hep-ph/0307022].
- [28] A. D. Martin, R. G. Roberts, W. J. Stirling and R. S. Thorne, Eur. Phys. J. C **39** (2005) 155 [hep-ph/0411040].
- [29] R. S. Thorne, [hep-ph/0506251].
- [30] M. Cacciari, M. Greco and P. Nason, JHEP **9805** (1998) 007 [hep-ph/9803400];
M. Cacciari, S. Frixione and P. Nason, JHEP **0103** (2001) 006 [hep-ph/0102134].
- [31] B. Andersson, G. Gustafson, G. Ingelman and T. Sjöstrand, Phys. Rept. **97** (1983) 31.
- [32] M. G. Bowler, Z. Phys. C **11** (1981) 169.
- [33] G. Marchesini, B.R. Webber, G. Abbiendi, I.G. Knowles, M.H. Seymour and L. Stanco, Computer Phys. Commun. 67 (1992) 465; HERWIG 6.5, G. Corcella, I.G. Knowles, G. Marchesini, S. Moretti, K. Odagiri, P. Richardson, M.H. Seymour and B.R. Webber, JHEP 0101 (2001) 010 [hep-ph/0011363]; [hep-ph/0210213].
- [34] H. Jung and G.P. Salam, Eur. Phys. J. C **19** (2001) 351 [hep-ph/0012143];
H. Jung, Comput. Phys. Commun. **143** (2002) 100 [hep-ph/0109102].
- [35] H. Jung, Comput. Phys. Commun. **86** (1995) 147.

- [36] A. Kwiatkowski, H. Spiesberger and H.J. Möhring, *Comput. Phys. Commun.* **69** (1992) 155.
- [37] G. A. Schuler and H. Spiesberger, *Proceedings, Physics at HERA*, vol. 3* 1419-1432.
- [38] G. Ingelman, A. Edin and J. Rathsman, *Comput. Phys. Commun.* **101** (1997) 108 [hep-ph/9605286].
- [39] S. Frixione, P. Nason and B. R. Webber, *JHEP* **0308** (2003) 007 [hep-ph/0305252].
- [40] I. Abt *et al.* [H1 Collaboration], *Nucl. Instrum. Meth. A* **386** (1997) 310 and 348.
- [41] ZEUS Collaboration, U.Holm (ed.), (unpublished), DESY 1993, available at www-zeus.desy.de/bluebook/bluebook.html
- [42] F. Abe *et al.* [CDF Collaboration], *Nucl. Instrum. Meth. A* **271** (1988) 387.
- [43] K. Ahmet *et al.* [OPAL Collaboration], *Nucl. Instrum. Meth. A* **305** (1991) 275.
- [44] D. Pitzl *et al.*, *Nucl. Instrum. Meth. A* **454** (2000) 334 [hep-ex/0002044].
- [45] D. Buskulic *et al.* [ALEPH Collaboration], *Nucl. Instrum. Meth. A* **360** (1995) 481.
- [46] C. J. S. Damerell *et al.*, *Nucl. Instrum. Meth. A* **288** (1990) 236.
- [47] I. J. Kroll, [hep-ex/9602005].
- [48] A. Aktas *et al.* [H1 Collaboration], *Eur. Phys. J. C* **38** (2005) 447 [hep-ex/0408149].
- [49] T. Nicholls *et al.* [H1 SpaCal Group], *Nucl. Instrum. Meth. A* **374** (1996) 149.
- [50] S. Chekanov *et al.* [ZEUS Collaboration], *Eur. Phys. J. C* **38**, 29 (2004) [hep-ex/0409033].
- [51] S. Eidelman *et al.* [Particle Data Group], *Phys. Lett. B* **592** (2004) 1.
- [52] A. Aktas *et al.* [H1 Collaboration], [hep-ex/0502010].
- [53] J. Breitweg *et al.* [ZEUS Collaboration], *Eur. Phys. J. C* **18** (2001) 625 [hep-ex/0011081].
- [54] A. Aktas *et al.* [H1 Collaboration], to appear in *Eur. Phys. J. C.*, [hep-ex/0411046].
- [55] H1 Collaboration, contributed paper 405, XXII International Symposium on Lepton-Photon Interactions at High Energy, Uppsala, Sweden, 2005.

- [56] D. Buskulic *et al.* [ALEPH Collaboration], Phys. Lett. B **313** (1993) 535.
- [57] A. Aktas *et al.* [H1 Collaboration], submitted to Phys. Lett. B, 03/05, [hep-ex/0503038].
- [58] S. Chekanov *et al.* [ZEUS Collaboration], contributed paper 575, International Europhysics Conference on High Energy Physics (EPS 2003), Aachen, Germany, 2003.
- [59] ZEUS Collaboration, contributed paper 269, XXII International Symposium on Lepton-Photon Interactions at High Energy, Uppsala, Sweden, 2005.
- [60] S.D. Ellis and D.E. Soper, Phys. Rev. D **48** (1993) 3160 [hep-ph/9305266].
- [61] S. Catani, Y.L. Dokshitzer, M.H. Seymour and B.R. Webber, Nucl. Phys. B **406** (1993) 187.
- [62] J.M. Butterworth, J.P. Couchman, B.E. Cox and B.M. Waugh, Comput. Phys. Commun. **153** (2003) 85 [hep-ph/0210022].
- [63] C. Adloff *et al.* [H1 Collaboration], Z. Phys. C **74**, (1997) 221 [hep-ex/9702003].
- [64] H. Plochow-Besch, PDFLIB:User's Manual, CERN-ETT-TT 2000.04.17 (<http://wwwinfo.cern.ch/asdoc/pdflib.ps.gz>).
- [65] S. Aid *et al.* [H1 Collaboration], Nucl. Phys. B **472** (1996) 32 [hep-ex/9604005].
- [66] M. Derrick *et al.* [ZEUS Collaboration], Phys. Lett. B **349** (1995) 225 [hep-ex/9502002].
- [67] M. Arneodo *et al.* (EMC Coll.), Z. Phys. C **35** (1987) 1.
- [68] ZEUS Collaboration, Submitted to 31nd International Conference on High Energy Physics, ICHEP02, 2002, Amsterdam, Abstract 786.
- [69] A. Aktas *et al.* [H1 Collaboration], contributed paper 5-0162, International Conference on High Energy Physics (ICHEP04), Beijing, China, 2004.
- [70] J. Breitweg *et al.* [ZEUS Collaboration], Eur. Phys. J. C **6** (1999) 67 [hep-ex/9807008].
- [71] A. Aktas *et al.* [H1 Collaboration], contributed paper 406, XXII International Symposium on Lepton-Photon Interactions at High Energy, Uppsala, Sweden, 2005.
- [72] S. Chekanov *et al.* [ZEUS Collaboration], [hep-ex/0507089].
- [73] S. Chekanov *et al.* [ZEUS Collaboration], Phys. Lett. B **565** (2003) 87 [hep-ex/0302025].

- [74] A. Aktas *et al.* [H1 Collaboration], “Study of Jet Shapes in Charm Photoproduction at HERA”. contributed paper 409, XXII International Symposium on Lepton-Photon Interactions at High Energy, Uppsala, Sweden, 2005.
- [75] A. Aktas *et al.* [H1 Collaboration], [hep-ex/0507081].
- [76] C. Adloff *et al.* [H1 Collaboration], Z. Phys. C **72** (1996) 593 [hep-ex/9607012].
- [77] S. Chekanov *et al.* [ZEUS Collaboration], Phys. Rev. D **69**, 012004 (2004) [hep-ex/0308068].
- [78] S. Chekanov *et al.* [ZEUS Collaboration], Phys. Rev. D **67** (2003) 012007 [hep-ex/0208023].
- [79] G. Ingelman, J. Rathsman and G.A. Schuler, Comput. Phys. Commun. **101** (1997) 135 [hep-ph/9605285].
- [80] C. Adloff *et al.* [H1 Collaboration], Phys. Lett. B **528** (2002) 199 [hep-ex/0108039].
- [81] C. Adloff *et al.* [H1 Collaboration], Nucl. Phys. B **545** (1999) 21 [hep-ex/9812023].
- [82] ZEUS Collaboration, Submitted to 32nd International Conference on High Energy Physics, ICHEP04, August 16, 2004, Beijing, Abstract 5-0344, 11-345.
- [83] J. Breitweg *et al.* [ZEUS Collaboration], contributed paper 495, International Europhysics Conference on High Energy Physics (EPS 2001), Budapest, Hungary, 2001.
- [84] C. Adloff *et al.* [H1 Collaboration], Phys. Lett. B **467** (1999) 156 [hep-ex/9909029]; [Erratum-ibid. B **518** (2001) 331].
- [85] S. Chekanov *et al.* [ZEUS Collaboration], Phys. Rev. D **70** (2004) 012008 [hep-ex/0312057].
- [86] S. Chekanov *et al.* [ZEUS Collaboration], Phys. Lett. B **599** (2004) 173 [hep-ex/0405069].
- [87] M. Derrick *et al.* [ZEUS Collaboration], Phys. Lett. B **348** (1995) 665 [hep-ex/9502008].
- [88] R. Thorne, private communication at Ringberg castle, october 2005.
- [89] P. Achard *et al.* [L3 Collaboration], Phys. Lett. B **619**, 71 (2005) [hep-ex/0507041].
- [90] M. Cacciari and P. Nason, JHEP **0309** (2003) 006 [hep-ph/0306212].
- [91] M. Cacciari, [hep-ph/0407187].

- [92] J. Breitweg *et al.* [ZEUS Collaboration], Eur. Phys. J. C **12** (2000) 35 [hep-ex/9908012].
- [93] A. Chuvakin, J. Smith and W. L. van Neerven, Phys. Rev. D **61** (2000) 096004 [hep-ph/9910250]; Phys. Rev. D **62** (2000) 036004 [hep-ph/0002011].
- [94] A. Aktas *et al.* [H1 Collaboration], contributed paper 407, XXII International Symposium on Lepton-Photon Interactions at High Energy, Uppsala, Sweden, 2005.
- [95] ZEUS Collaboration, Submitted to 31nd International Conference on High Energy Physics, ICHEP02, 2002, Amsterdam, Abstract 778.
- [96] S. Chekanov *et al.* [ZEUS Collaboration], arXiv:hep-ex/0508019.
- [97] ZEUS Collaboration, Submitted to 30nd International Conference on High Energy Physics, ICHEP00, July 27, 2000, Osaka, Abstract 854.
- [98] ZEUS Collaboration, contributed paper 497, International Europhysics Conference on High Energy Physics (EPS 2001), Budapest, Hungary, 2001.
- [99] A. Aktas *et al.* [H1 Collaboration], Phys. Lett. B **588** (2004) 17 [hep-ex/0403017].